# ANALYSIS OF THE LASER GROOVING PROCESS FOR CERAMIC MATERIALS

by

**WOO CHUN CHOI**

Bachelor of Science
Seoul National University, Seoul, Korea
(1982)

Master of Science
Seoul National University, Seoul, Korea
(1984)

SUBMITTED IN PARTIAL FULFILLMENT
FOR THE REQUIREMENTS FOR THE DEGREE OF

DOCTOR OF PHILOSOPHY
IN MECHANICAL ENGINEERING

at the

MASSACHUSETTS INSTITUTE OF TECHNOLOGY

September 1989

© Massachusetts Institute of Technology

The author hereby grants to M.I.T. permission to reproduce and to distribute copies of this thesis document in whole or in part.

Signature of Author ___ Signature redacted
Department of Mechanical Engineering
September 10, 1989

Certified by Signature redacted
Prof. George Chryssolouris
Thesis Supervisor

Accepted by _____ Signature redacted
Prof. Ain A. Sonin
Departmental Committee on Graduate Students

ARCHIVES

MASSACHUSETTS INSTITUTE
OF TECHNOLOGY

AUG 13 1990

LIBRARIES

# ANALYSIS OF THE LASER GROOVING PROCESS FOR CERAMIC MATERIALS

by

WOO CHUN CHOI

## ABSTRACT

In order to overcome the low energy efficiency associated with conventional laser machining, a three-dimensional laser machining process has been developed utilizing two laser beams. In this process each laser beam creates a groove on the workpiece surface. When the two grooves converge, a large volume of material is removed. In this manner, large-scale material removal processes such as turning, threading and milling processes can be implemented.

An essential element in the three-dimensional machining is single beam grooving. To describe the grooving process, analytical and numerical analyses were performed, which account for beam power, heat conduction and material ablation. The theoretical analysis was also modified to account for changing conduction area and direction.

In ceramic materials the primary phase change is melting. The molten material has to be removed in order to yield deep and clean grooves. Unlike in through-cutting, molten material removal is difficult in grooving due to the groove geometry. To eject molten material, an off-axial supersonic jet is used. Both theoretical analysis (through modification of the laser grooving analysis) and experimentation (through a statistical experimental design approach) were performed to understand gas-jet-aided grooving, find the jet condition for maximum grooving effectiveness and determine a dominant jet parameter affecting groove formation.

Comparison between the theoretical and experimental results were made, and showed a good agreement. Among various jet parameters, reservoir pressure is found to be the most important parameter, and the best jet condition is found. A significant improvement in energy efficiency was achieved in the three-dimensional machining compared with single beam laser machining processes.

# ACKNOWLEDGEMENT

I would like to thank my adviser, Prof. George Chryssolouris, for his continuous encouragement and advice. I really enjoyed working for him. I would also like to thank Prof. Mikic and Prof. Sonin for their valuable advice. I wish to thank Paul Sheng for valuable comments. I dedicate this thesis to my parents who have been giving me moral support all the time.

# TABLE OF CONTENTS

Title
Abstract
Acknowledgement
Table of Contents
List of Figures
List of Tables

1. Introduction

2. Theoretical analysis of the laser grooving process

   2.1 Problem definition

   2.2 Groove formation: heat transfer analysis
      2.2.1 Analytical solution
      2.2.2 Modified solution
      2.2.3 Numerical solution

   2.3 Gas jet interaction and molten layer behavior

   2.4 Three-dimensional machining

3. Experiments results and discussion

   3.1 Gas jet test
      3.1.1 Flat-workpiece test
      3.1.2 Grooved-workpiece test
      3.1.3 Real-size-groove test

   3.2 Grooving test
      3.2.1 Effects of an off-axial gas jet
      3.2.2 Effects of gas jet parameters on groove depth

4. Conclusions

References

Appendix

A. Gas Jet Effects on Laser Cutting
B. Fortran Program for Numerical Analysis
C. Fortran Program for Regression
D. Optimization of Three-Dimensional Machining

# LIST OF FIGURES

Fig. 1.1: Three-Dimensional Laser Machining Concept.
Fig. 1.2: Laser Machine for Three-Dimensional Laser Machining.
Fig. 1.3: Molten Layer Effect on Groove Formation.
(a) gas jet is effective; (b) gas jet is not effective.

Fig. 2.1: Schematic of Gas-Jet-Aided Laser Grooving.
Fig. 2.2: Single (a) and Multiple Pass (b) Laser Grooving.
Fig. 2.3: Analytical Model for the Laser Grooving Process.
Fig. 2.4: Control Volume inside Solid Medium.
Fig. 2.5: Isotherm Surfaces in the Conduction Direction.
Fig. 2.6: $I(\infty)$ vs. $\sigma$.
Fig. 2.7: Ratio of Conduction Heats Predicted by Analytical and Modified Solutions.
Fig. 2.8: Configuration of the Laser Beam and a Coordinate System (a) and Boundaries for Numerical Analysis (b).
Fig. 2.9: Control Surface at Cutting Front in Numerical Analysis.
Fig. 2.10: Driving Forces for Molten Material Removal.
Fig. 2.11: Under-Expanded Supersonic Jet with a Mach Shock Disc.
Fig. 2.12: Molten Layer and Control Volume.
Fig. 2.13: Numerical Domain and Boundaries for Three-Dimensional Machining.

Fig. 3.1: Experimental Apparatus and Wokpieces for Gas Jet Tests.
Fig. 3.2: Convergent Nozzles Used in Gas Jet Tests.
Fig. 3.3: Workpiece Pressure vs. Reservoir Pressure for Nozzle/Workpiece Distance Variations (nozzle exit diameter = 0.1 cm, and jet attack angle = 90°).
Fig. 3.4: Reservoir Pressure and Jet Structure.
Fig. 3.5: Under-Expanded Supersonic Cell Dimension vs. Reservoir Pressure [64].
Fig. 3.6: Shock Types Depending on Nozzle/Workpiece Distance.
Fig. 3.7: Workpiece Pressure as a Function of Radial Distance from the Jet Targeting Point (nozzle/workpiece distance = 0.4 cm, nozzle exit diameter = 0.1 cm , and jet attack angle = 90°).
Fig. 3.8: Jet Separation and Surface Flow Visualization.
Fig. 3.9: Pressure Difference vs. Reservoir Pressure for Groove Depth Variations (other conditions: 0.4cm nozzle/workpiece distance, 0.1cm nozzle exit diameter, 90° jet attack angle, 0.076cm groove width, 45° cutting front angle).

Fig. 3.10: Pressure Difference vs. Reservoir Pressure for Groove Width Variations (other conditions: 0.4cm nozzle/workpiece distance, 0.1cm nozzle exit diameter, 90° jet attack angle, 0.74cm groove depth, 45° cutting front angle).
Fig. 3.11: Pressure Difference vs. Reservoir Pressure for Groove Angle Variations (other conditions: 0.4cm nozzle/workpiece distance, 0.1cm nozzle exit diameter, 90° jet attack angle, 0.74cm groove depth, 0.076cm groove width).
Fig. 3.12: Pressure Difference vs.Reservoir Pressure for Nozzle/workpiece Distance Variations.(other conditions: 0.1cm nozzle exit diameter, 90° jet attack angle, 0.74cm groove depth, 0.076cm groove width, 45° cutting front angle).
Fig. 3.13: Pressure Difference vs. Reservoir Pressure for Jet Targeting Distance Variations.(other conditions: 0.4cm nozzle/workpiece distance, 0.1cm nozzle exit diameter, 90° jet attack angle, 0.74cm groove depth, 0.076cm groove width, 45° cutting front angle).
Fig. 3.14: Pressure Difference vs. Reservoir Pressure for Jet Attack Angle Variations.(other conditions: 0.4cm nozzle/workpiece distance, 0.1cm nozzle exit diameter, 0.74cm groove depth, 0.076cm groove width, 45° cutting front angle).
Fig. 3.15: Pressure Difference vs. Reservoir Pressure for Nozzle Exit Diameter Variation.(other conditions: 0.4cm nozzle/workpiece distance, 90° jet attack angle, 0.74cm groove depth, 0.076cm groove width, 45° cutting front angle).
Fig. 3.16: Flow Directions of Molten Material.
Fig. 3.17: Jet Flow Separation.
Fig. 3.18: Complete and Fractional Factorial Designs.
Fig. 3.19: Main Effect of Jet Targeting Distance on Pressure Difference.
Fig. 3.20: Main Effect of Nozzle/Workpiece Distance on Pressure Difference.
Fig. 3.21: Main Effect of Reservoir Pressure on Pressure Difference.
Fig. 3.22: Cross-Sectional Groove Shapes for Various Jet Conditions.
P = 500W, v = 0.508 cm/s, number of passes = 1: (a) 3 bar coaxial (b) 1.5 bar coaxial and 5 bar off-axial reservoir pressure
P = 500 W, v = 1.02 cm/s, number of passes = 2: (c) 3 bar coaxial (d) 1.5 bar coaxial and 5 bar off-axial reservoir pressure.
Fig. 3.23: Experimental Setup (Test I).
Fig. 3.24: Grooves Formed under the Process Condition: Laser Power = 500 W,

Scanning Velocity = 0.508 cm/s, and Number of Passes = 2.

| | NWD (cm) | JAA(°) | JTD (cm) |
|---|---|---|---|
| (a) | 0.4 | 60 | 1.22 |
| (b) | 0.3 | 45 | 0.85 |
| (c) | 0.1 | 60 | 0.78 |
| (d) | 0.2 | 60 | 1.22 |

Fig. 3.25: Main Effect of Nozzle/Workpiece Distance on Groove Depth.

Fig. 3.26: Main Effect of Jet Targeting Distance on Groove Depth.

Fig. 3.27: Main Effect of Jet Attack Angle on Groove Depth.

Fig. 3.28: Grooving Test Setup for Test II and III.

Fig. 3.29: Main Effect of Nozzle/Workpiece Distance on Groove Depth.

Fig. 3.30: Main Effect of Jet Targeting Distance on Groove Depth.

Fig. 3.31: Main Effect of Reservoir Pressure on Groove Depth.

Fig. 3.32: Main Effect and Sensitivity of a Parameter.

Fig. 3.33: Variations of Parameters.

Fig. 3.34: Groove Depth vs. Nozzle/Workpiece Distance.

Fig. 3.35: Groove Depth vs. Jet Targeting Distance.

Fig. 3.36: Groove Quality on Two-Dimensional Plane of Nozzle/Workpiece Distance and Jet Targeting Distance.

Fig. 3.37: Parameter Conditions for Signal-To-Noise Ratio Calculation.
Black Point: conditions where SN ratios are calculated
Gray Point: conditions due to the variations of parameters.

Fig. 3.38: Geometric and Dynamic Similarity between Two Configurations.

Fig. 3.39: Groove Depth vs. Non-Dimensional Energy in Laser Grooving ($Al_2O_3$).

Fig. 3.40: Test Setup for Two-Beam-Laser Machining.

Fig. 3.41: Groove Depths for Single and Double Beam Grooving ($Al_2O_3$).

Fig. 3.42: Material Removal Rates for Various Processes [77].

# LIST OF TABLES

Table 3.1: Parameter Ranges for Groove Tests.

Table 3.2: Conditions for High Pressure Differences in Grooved-Surface Test.

Table 3.3: Parameter Levels for Real-Size-Groove Test.

Table 3.4: Physical Properties of Aluminum Oxide ($Al_2O_3$).

Table 3.5: Jet Conditions and Corresponding Groove Depths.

Table 3.6: Main Effects and Sensitivities of Three Jet Parameters.

Table 3.7: Jet Parameters and Groove Depths (Test III).

Table 3.8: Means and Signal-to-Noise Ratios for Several Test Conditions.

# CHAP 1. INTRODUCTION

The laser stands for light amplification by stimulated emission of radiation. Since laser machining was first demostrated in 1960, it has become a significant part of industrial practice. The high power densities that laser beams create on workpiece surfaces have been a particular asset in drilling and cutting operations.

As a non-contact tool, laser beams offer a number of advantages for machining, such as no tool wear, no cutting forces, no chattering, etc. Since laser machining depends only on the thermal properties of a workpiece material instead of its mechanical properties, laser beams can easily process advanced engineering materials, such as ceramics and composites. On the other hand, laser machining has certain drawbacks, such as low energy efficiency and constraints on machining geometries (limited to one-dimensional drilling, two-dimensional scribing, and cutting operations).

A three-dimensional laser machining concept has been developed [1,2] in which two laser beams create blind kerfs in a workpiece. When the two kerfs converge, a volume of material is removed (Fig. 1.1). According to the concept, the three-dimensional machining process is flexible in terms of shapes and forms that can be worked, and is substantially more energy efficient than single-beam ablation of the entire volume of material, since energy is only consumed on the grooves to be made and not on the entire volume of material to be removed.

In order to perform three-dimensional laser machining, a dual beam $CO_2$ laser machine is used in the Laboratory for Manufacturing and Productivity, MIT. As shown in Fig. 1.2, the laser machine consists of three parts: laser cavity, beam delivery system, and workpiece positioning system. The two laser beam tools can be rotated around a central axis. A workpiece is translated in two directions and rotated by three step motors, which are controlled by a micro-computer.

The material removal rate as well as the dimensional accuracy of the three-dimensional laser machining process is directly related to the depth of the grooves [3,4]. Therefore, laser grooving is an essential element of the three-dimensional laser machining. In order to understand the three-dimensional machining better, the grooving process should be studied first. In the laser grooving process, a blind kerf is formed by a single laser

beam through single or multiple passes over a workpiece. The grooving process depends on process variables (such as beam power, scanning velocity, number of beam passes, etc) and gas jet parameters (in situations where a molten layer is formed in the groove).

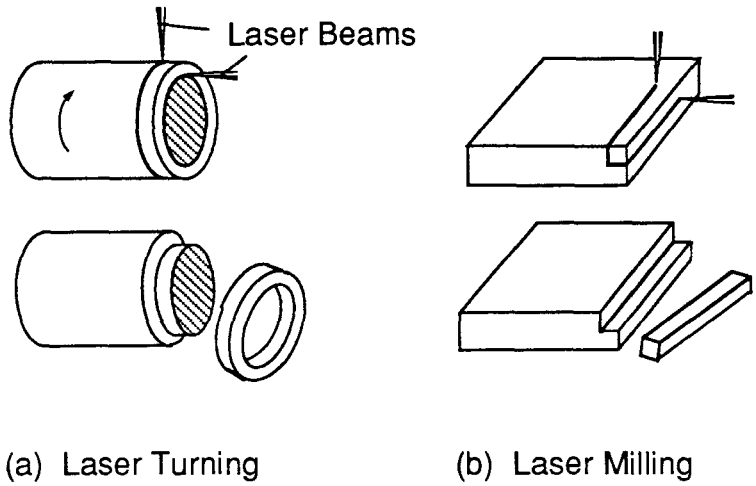



Fig. 1.1: Three-Dimensional Laser Machining Concept

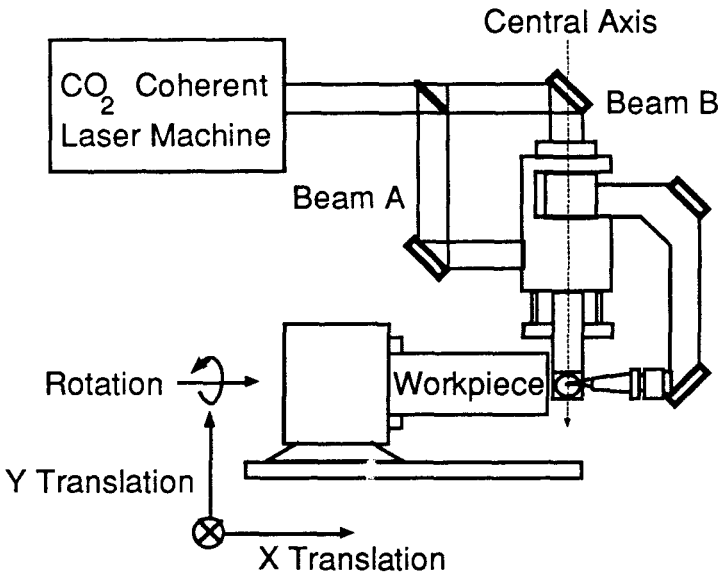



Fig. 1.2: Laser Machine for Three-Dimensional Laser Machining

A gas jet can be used to force the molten material from the groove to continuously expose new surface to the laser beam. If the gas jet is effectively utilized, the majority of the beam energy will be absorbed at the new groove bottom surface, and a very thin (order

of beam diameter) straight groove can be made on the workpiece. On the other hand, if the molten material is not effectively removed, it interacts with the laser beam and tends to grow into a thick molten layer (Fig. 1.3). The molten material resolidifies in the groove, causing a reduction in the groove depth as well as a deterioration in the surface quality. This results in a rather wide groove with walls which are not straight. The use of a gas jet reduces the molten layer thickness. A thin molten layer reduces the diversion of beam energy to heating the molten material above the melting point. Also, the use of a gas jet reduces the width of a melting front cross-section and increases the depth of the melting front cross-section because of the energy conservation. In multiple-pass grooving, a significant portion of the laser beam energy must be diverted to remelt the resolidified material that was not removed by the jet during the previous beam pass. The use of a gas jet minimizes the amount of resolidified material and, correspondingly, reduces the beam energy loss to remelt the resolidified material.

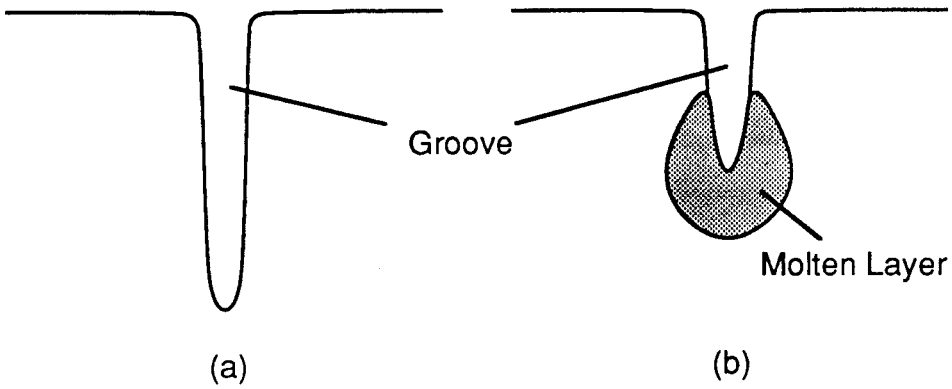



Fig. 1.3: Molten Layer Effect on Groove Formation
(a) gas jet is effective; (b) gas jet is not effective

This thesis addresses the effectiveness of using gas jets to improve groove depth and surface quality in laser grooving. The objectives of this thesis are to *understand the physical mechanism in gas jet-aided grooving*, to *develop a theoretical model of grooving and three-dimensional machining, and to find the effect of a gas jet on groove formation.* In order to achieve the objectives, the followings are considered:

- Analysis
  - grooving with the aid of an off-axial jet
  - three-dimensional machining

- Experiments
  - gas jet test
  - grooving test (aluminum oxide)
  - three-dimensional machining test

- Comparison between theoretical and experimental results

## Background on Laser Machining

When laser radiation interacts with a solid, several thermal-related effects occur. Photon absorption at the surface is the first phenomenon. Depending on the intensity of the incident laser beam, heating and vaporization with photon penetration can occur at the moment of the laser interaction [5,6]. Material heating can occur for low beam intensities. The photon energy absorbed transforms instantaneously into thermal energy heating the surface, until the surface temperature reaches the phase transition temperature. As the melting and vaporization temperatures are reached, new phases and moving boundaries appear. Vaporization with photon penetration can occur for very high intensities. An extremely high intensity causes sufficient transmittance of the laser energy past the surface, resulting in the appearance of plasma. Due to heating inside the material subsurface temperatures exceed the vaporization temperature [7]. This high temperature causes a vapor explosion.

The laser induced plasma changes dramatically the conditions of material processing. The absorptivity vary suddenly at the interface from the moment that interaction starts. The temperature increase is accompanied by phase transition. Due to the temperature difference, heat is conducted into the medium. In laser machining, phase change, conduction, and a moving heat source are involved.

Most of the theoretical work on laser machining heat transfer has centered on the solution of the heat conduction equation for a stationary or moving semi-infinite solid [8-11]. Heat conduction problems with moving heat sources have been originally treated in [12, 13]. Exact solutions were obtained for a number of problems with two phases [12]. Rosenthal [13] outlined the fundamentals of the theory of moving source of heat, and derived appropriate solutions for linear, two and three dimensional flow of heat in solids of infinite size or bounded by plane. By assuming that the heat is supplied by a point heat

source moving with a constant speed along the x-axis, the temperature distribution around the heat source was determined. If heating occurs for long enough, the temperature distribution around the heat source soon becomes constant, and the end effects become negligible. This can be applied to any process where the heat source moves at a constant velocity relative to a workpiece such as cutting and grooving. The problem of heating a homogeneous slab of material induced by time dependent laser irradiance was studied in [14]. In [15] heat conduction was investigated in a moving semi infinite medium subject to laser irradiation.

Drilling in which there is no relative movement between laser beam and workpiece has been investigated early. The initial stage of drilling is unsteady, since absorptivity changes significantly at the instant of laser interaction. Absorptivity, which depends on the interaction time, affects drilling performance. Absorptivity variation during laser drilling was investigated in many papers [16,17]. Time-dependent radiation reflectivity of the metals was found to account for most of the incident power in the initial stages of the interaction in [6]. In [18] the sequential steps of the plume evolution caused by a ruby laser pulse was investigated. They found that the laser intensity and absorptivity are the most important factors for drilling process. Drilling was performed over various materials [19-21]. Hole depth and shape were predicted as a function of absorbed intensity in [22].

Drilling is performed mostly with a pulsed laser, which by storing energy produces higher intensities evaporating a material more easily. For varying pulse lengths, the effects were investigated on laser drilling in [23]. Pulsed laser beams create a large temperature gradient inside the material because of its high intensity and short interaction time. This causes a large thermal stress which induces cracks in the material. In [24] the temperature profile and the tangential stress distribution of the laser-formed hole were calculated to indicate the magnitude of those factors that can influence the potential fracture of alumina material. In [25] residual stresses were measured from strain measurement near a hole. By calculating the transient and steady state temperature rise of laser irradiated metals, it was showed that values of the intensity that cause failure change drastically [26].

For such processes as drilling, cutting, and grooving, molten or vaporized material should be removed, in order to form a hole or kerf. Unlike cutting or grooving, where high pressure gas jets are used for the purpose of material expulsion, beam interaction time is relatively short for drilling, and thus a gas jet is not effective. Instead, the explosive vaporization at the subsurface results in very rapid and efficient material removal [7].

Material is removed in the form of liquid and/or vapor. Expulsion mechanism of liquid material during drilling was investigated in [16,18,22]. To predict an explosive vaporization, several models have been developed treating laser beam power as a heat source inside the medium rather than as a surface interaction [7,15,27]. In their models, penetration of the laser beam into the material was allowed by a distributed heat source coupled to a moving boundary. With the models the temperature distribution inside the medium was calculated, and a peak temperature inside the medium was predicted.

Usually the term laser cutting implies laser "through" cutting in which a laser beam penetrates through the entire thickness of the workpiece and advances parallel to the surface of the workpiece. Laser cutting is the most widely used machining process. In the laser cutting of metals, a laser beam heats up, and melts or evaporates a metallic workpiece, while a gas jet is used to drive out the molten or vaporized material. Depending on the phase of material removed, laser cutting is divided into sublimation and fusion cutting. In the case of sublimation cutting, the material is vaporized, and pulsed solid state lasers are mainly used. In the case of laser fusion cutting the material is melted in the region of the cutting seam and is then blown out with the aid of an inert gas jet. If a gas jet which is not inert (i.e., oxygen) is used, the process is called a reactive gas assisted cutting, where a reaction energy serves as an additional heat source in addition to the laser beam energy.

In laser cutting, maximum cutting speed is of interest. The effect of cutting parameters in laser gas cutting on the qualities of cuts has been studied in stainless steel plates using a 1 kW $CO_2$ laser in [28]. It was found that tandem nozzle cutting was significantly more effective in improving surface roughness and flatness of the cut than coaxial jet alone. In [29], based on the absorptivity calculated over the cutting kerf, a cutting model was developed. Schuocker et al. [30] suggested a model based on the assumption that the momentary end of the cut is covered by a thin molten layer which loses mass by evaporation and by ejection of liquid material. In [31] a relationship between the power density incident on a material and the resulting cutting speed was developed in terms of the thermal properties of the material. In [32], on the basis of the wave equation, the relation between the degree of absorption and the inclination of the cutting front were obtained for different laser modes, types of polarization and focal positions. Based on the absorptivity, cutting parameter effects on laser cutting were investigated. In [33] a parametric study of pulsed laser cutting of thin metal plates was reported. In [34] a relation between maximum cutting thickness and cutting speed for a given laser power was obtained.

For many materials, periodic striations are observed on the cut surfaces. The occurrence of striations is undesirable since it deteriorates the surface quality. The striations on the cut surfaces are due to an unsteady motion of the melt. When a laser beam heats up material to a temperature to ignite in the presence of the oxygen, the resulting combustion pushes molten material radially away from the laser spot. The combustion front comes to rest and the subsequent encroachment of the laser beam on the new cutting front repeats the oxidation initiation process. The resulting cut surface consists of regularly spaced striations. In [35] a dynamic solution predicted a periodic oscillation superimposed on the steady state temperature of the melt. A stability analysis associated with ripple formation was presented in [36].

In the laser welding processes, material removal is not involved. In [37] the absorption of a laser beam by a workpiece was described and the physical, chemical, and thermal changes were shown to cause welding of the workpiece. The power absorbed at the surface goes into melting, vaporization, and heat conduction into the medium. If the beam is sufficiently intense, the energy is deposited in a cavity. This cavity is known as a keyhole, which is formed relatively quickly at the start of the run, and is filled with gas or vapor, and surrounded by liquid. On the rear side of the keyhole the metal freezes as heat is conducted away from it into the solid, and this solidification forms the weld. The depth of the keyhole is much greater than the penetration depth of photons into the solid and liquid phase, and is limited by the beam power or by the absorption of the beam. In [38] a relationship was shown for the dependence of maximum single pass laser weld penetration on power, and a range of laser welding applicability was determined. In [39] a thermal analysis for laser heating and melting materials was derived for a Gaussian source moving at a constant velocity.

The penetration is opposed by the flow of molten material into the keyhole, and a balance of these effects results in a steady state hole profile. There are three other forces which should be considered in general: gravity, surface tension, and vapor pressure. Gravity is a restoring force. Temperature gradients on the melt surface between the laser beam interaction spot and the intersection line of the solid-liquid interface generate a surface tension gradient. The surface tension pulls the liquid material from the hot central region to the cold outer region. Surface tension reduces the depth of penetration typically by a factor of about three [40]. There is some vapor flow across the cavity providing the pressure

which drives the liquid. The pressure inside the cavity is governed by the hydrostatic pressure in the liquid, and by the viscous forces acting on the vapor stream [41].

Flow conditions in the horizontal plane determine the dimensions of the weld. Material is moved around the advancing vapor cavity mainly by liquid flow. In [41] the conditions of energy and material flow during beam welding were investigated theoretically to determine the factors which govern the shapes of the vapor cavity and of the molten zone. The flow of the liquid and surface tension tends to obliterate the cavity, while the vapor which continuously generated tends to maintain the cavity. Return flow is set up because of the existence of the solid liquid interface. This recirculating flow is much faster than the scanning motion [42]. As the flow develops, convection becomes the dominant energy transfer mechanism. Based on a perturbation solution due to the small scanning velocity, a weld pool shape was obtained. In [43] relationships between the weld width, the power absorbed per unit thickness of the workpiece, and the speed of welding were investigated from a mathematical model for the heat transfer and fluid flow in the molten metal surrounding a keyhole. In [44], a simple model was developed to determine keyhole shapes and the variation in the keyhole depths.

The flow of liquid due to surface tension gradients and material lost by vaporization create a depression of the liquid surface beneath the beam and ridging of the liquid surface elsewhere. As the beam passes to other areas of the surface, this distortion of the liquid surface is frozen in, creating a roughened rippled surface. In [45] it was examined how surface tension gradients cause significant rippling of a laser melted surface, and it was shown that rippling from surface tension gradients can be avoided if during surface melting the laser beam velocity exceeds a critical velocity.

In grooving a laser beam does not cut through the entire workpiece. Little work has been done on the grooving process. A numerical analysis on laser grooving was done, by assuming immediate evaporation of the solid material due to the laser irradiation in [46]. The governing equation in this study was a groove formation equation, and the temperature distribution inside the medium was assumed. A model distinguishing the process into different regions was suggested in [47]. Experimental results on laser grooving were reported in [48]; grooves on metallic and ceramic materials were produced using a single laser beam. As an element of a three-dimensional laser machining, laser grooving was investigated in [49].

# CHAP 2. THEORETICAL ANALYSIS OF THE LASER GROOVING PROCESS

## 2.1 Problem Definition

As a component of three-dimensional laser machining, the grooving process exhibits complicated characteristics, such as three-dimensional heat transfer, 2 phases, moving boundary, spatially distributed heat source, gas jet interaction, etc. (Fig. 2.1). Furthermore, there is interdependence among the behavior of a gas jet, molten layer and groove geometry. A gas jet creates a pressure field on a cutting front, which affects molten layer thickness distribution. A cutting front is defined as a surface interacted by the laser beam. A molten layer interacts with the laser beam as well as the gas jet through the cutting front, and with a solid medium through the melting front. Conduction heat from the molten layer melts solid material, and is transferred into the solid. From an analysis point of view, grooving can be decomposed into three parts: gas jet interaction, molten layer behavior, and groove formation.

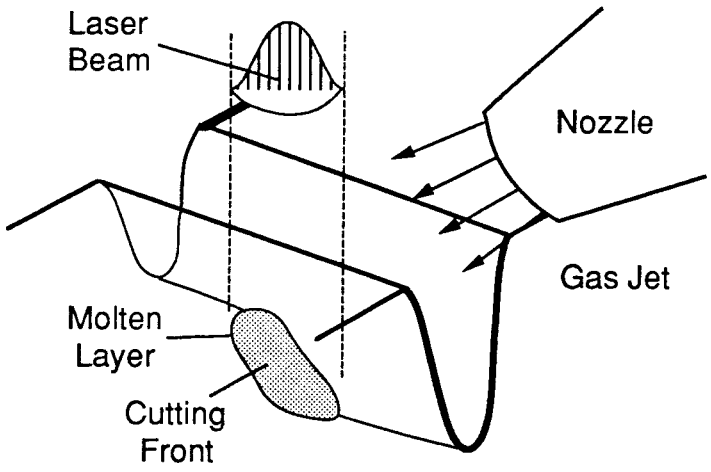



Fig. 2.1: Schematic of Gas-Jet-Aided Laser Grooving.

The following assumptions are made to simplify the analysis without substantially sacrificing its accuracy:

1. The relative speed of the laser beam travelling over the workpiece is constant.

2. The workpiece material is isotropic and has constant properties. Among the material properties, thermal conductivity varies significantly with temperature: for example, the thermal conductivity of aluminum oxide varies from 0.36 W/cm°C at room temperature to 0.064 W/cm°C at the melting point. The conduction heat into the interior of the workpiece depends on the conductivity and the temperature gradient at the melting front. If conductivity is assumed as the value at the melting front, the real temperature gradient at the melting front is not significantly different from the temperature gradient based on conductivity varying as a function of temperature. Thus groove formation is not significantly affected by the conductivity variation, while the temperature distribution inside the solid which is not close to the melting front depends greatly on the conductivity variation.

3. Melting is the only significant phase change that occurs, and possible evaporation of some of the liquid material is neglected. This assumption is based on the fact that in engineering materials such as metals the predominant phase change for laser grooving at commercially available laser powers is melting. In reality, however, it may be that some evaporation occurs, depending on the interaction time of the beam on the material. Furthermore, in materials such as composites and plastics, evaporation is the predominant phenomenon.

4. A gas jet removing the molten material from the groove does not interfere with the laser beam. The use of gas jets is a critical factor in producing thin straight kerfs.

5. The laser beam spot size remains constant. However, in numerical analysis the beam defocusing effect is considered.

6. The material is opaque; that is, that the laser beam does not penetrate appreciably into the medium, which exhibits constant absorptivity. The effect of polarization on absorptivity is not considered.

7. In the literature, a variety of phenomena related to laser beam interaction with a workpiece material has been reported such as small explosions of the workpiece material, etc. These phenomena have not been considered in this analysis.

## 2.2 Groove Formation: Heat Transfer Analysis

When a very effective gas jet is used, the molten layer thickness is negligible, and the convection effect of the molten material becomes insignificant. Without considering the convection effect of the gas jet, absorbed laser beam power is used either to melt material or to be conducted into the solid. In this situation, groove depth can be estimated without considering gas jet interaction and molten layer behavior. This method is also applicable to the cases where workpiece material does not melt but vaporizes. Later, the groove formation solution will be modified to account for a molten layer with finite thickness.

### 2.2.1 Analytical Solution

Fig. 2.2 schematically shows the process of laser grooving for (a) single pass and (b) multiple passes of the laser beam over the workpiece. The Cartesian coordinates system (x, y, z) is moving with the laser beam which has an intensity profile J(x,y) projected onto the groove surface. $s_-(y)$ (Fig. 2.2(b)) is the depth of the pre-existing groove surface formed by previous laser passes, s(x,y) is the depth of the current groove surface, and $s_+(y)$ is the depth of the already developed groove surface during this pass.

In order to gain a quantitative understanding of the effect on the process of the different process parameters, an infinitesimal control surface (Fig. 2.3) on the cutting front surface can be studied. The control surface is inclined at an angle $\theta$ with respect to the x-axis and at an angle $\phi$ with respect to the y-axis, and is subjected to a laser beam of intensity J(x,y).

A three-dimensional heat conduction equation governs the heat transfer problem with a moving heat source:

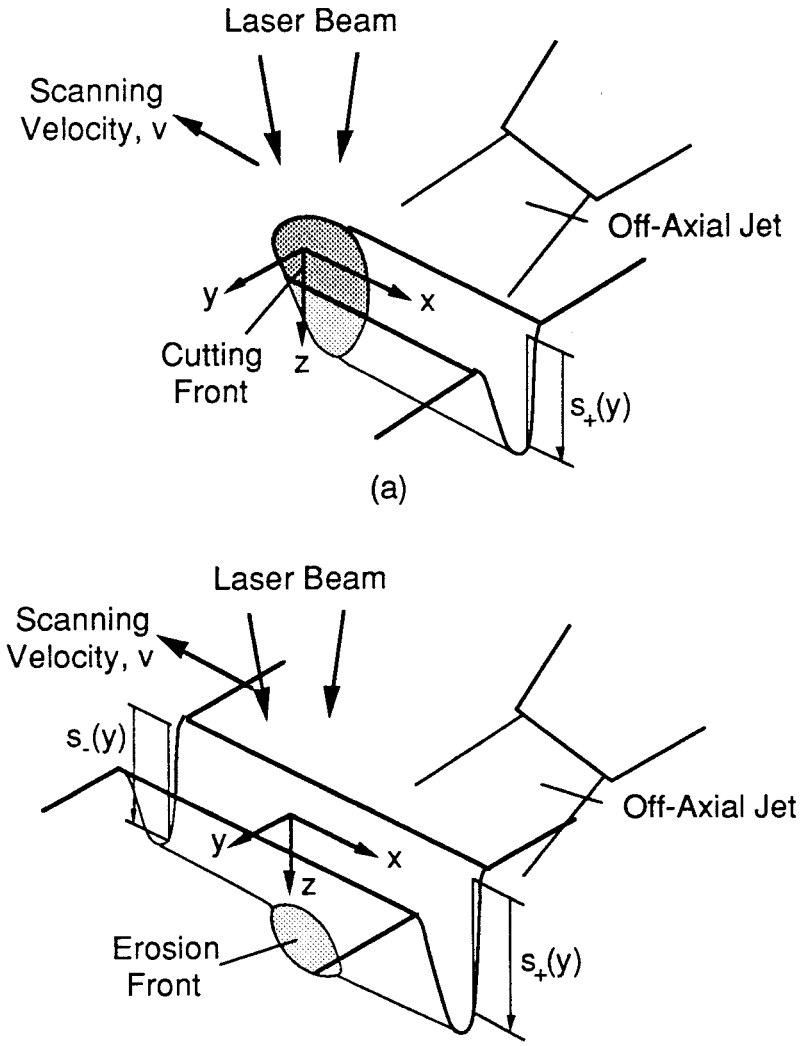



Fig. 2.2: Single (a) and Multiple Pass (b) Laser Grooving

$$k\left(\frac{\partial^2 T}{\partial x^2}+\frac{\partial^2 T}{\partial y^2}+\frac{\partial^2 T}{\partial z^2}\right)=v\rho c_p\frac{\partial T}{\partial x} \tag{2.1}$$

where k is thermal conductivity, T is temperature, v is scanning velocity, $\rho$ is the density of the material, $c_p$ is the specific heat of the material

or

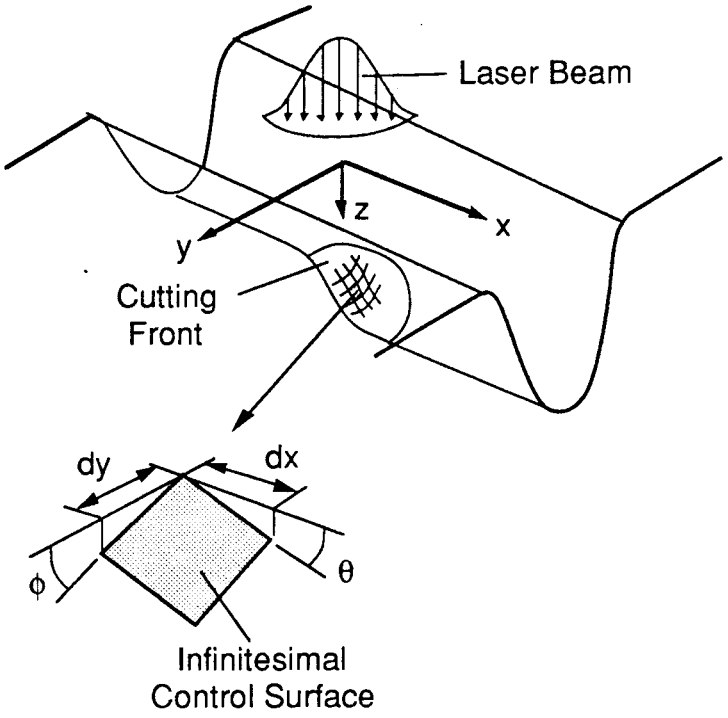



Fig. 2.3: Analytical Model for the Laser Grooving Process

$$\nabla^2 T = \frac{v}{\alpha}\frac{\partial T}{\partial x} \tag{2.2}$$

where $\alpha$ is the thermal diffusivity of the workpiece

subject to:

$$\begin{aligned} &\text{at the cutting front surface : } T=T_s \\ &x\rightarrow\pm\infty,\ y\rightarrow\pm\infty,\ z\rightarrow\infty : T=T_o \end{aligned} \tag{2.3}$$

where $T_s$ is the surface temperature, and $T_o$ is the ambient temperature.

In order to simplify Eq. (2.2), it is assumed that heat is conducted in the direction normal to the surface of the cutting front. Accordingly the following relations can be derived.

$$\frac{\partial T}{\partial x} = -\frac{\partial T}{\partial z}\tan\theta \tag{2.4}$$

$$\frac{\partial T}{\partial y} = \frac{\partial T}{\partial z}\tan\phi \tag{2.5}$$

$$\frac{\partial T}{\partial n} = \left(\left(\frac{\partial T}{\partial x}\right)^2 + \left(\frac{\partial T}{\partial y}\right)^2 + \left(\frac{\partial T}{\partial z}\right)^2\right)^{1/2} \tag{2.6}$$

where n is a coordinate normal to the cutting front surface. Additionally, the following simplification is assumed.

$$\nabla^2 T = \frac{\partial^2 T}{\partial n^2} \tag{2.7}$$

From Eqs. (2.4), (2.5), and (2.6), $\partial T/\partial x$ can be related to $\partial T/\partial n$.

$$\frac{\partial T}{\partial x} = -\frac{\partial T}{\partial n}\frac{\tan\theta}{(1 + \tan^2\theta + \tan^2\phi)^{1/2}} = -\beta\frac{\partial T}{\partial n} \tag{2.8}$$

$$\text{where} \quad \beta = \frac{\tan\theta}{(1 + \tan^2\theta + \tan^2\phi)^{1/2}} \tag{2.9}$$

Eqs. (2.4) and (2.5) are correct at the cutting front, but not generally correct inside the medium where the direction of n is not always perpendicular to the cutting front. Eq. (2.2) can be simplified as:

$$-\frac{\beta v}{\alpha}\frac{\partial T}{\partial n} = \frac{\partial^2 T}{\partial n^2} \tag{2.10}$$

subject to the following boundary conditions:

$$\begin{aligned} &\text{at } n=0,\ T=T_s \\ &\text{as } n\to\infty,\ T=T_o \end{aligned} \tag{2.11}$$

The temperature distribution inside the medium can be determined as:

$$\frac{T - T_o}{T_s - T_o} = e^{-\frac{\beta v}{\alpha} n} \tag{2.12}$$

The temperature gradient at the cutting front can be determined as:

$$\left(\frac{\partial T}{\partial n}\right)_{n=0} = -\frac{\beta v}{\alpha}(T_s - T_o) \tag{2.13}$$

The energy balance at the infinitesimal control surface is given by:

$$aJ(dxdy) = -k\,dA\left(\frac{dT}{dn}\right)_{n=0} + \rho Lv(dxdy)\tan\theta \tag{2.14}$$

where a is the absorptivity of the material, L is the latent heat of fusion, and dA is an infinitesimal control surface area (Fig. 2.3)

$$\begin{aligned} dA &= ((dxdy)^2 + (dx\tan\theta\, dy)^2 + (dxdy\tan\phi)^2)^{1/2} \\ &= dxdy\,(1 + \tan^2\theta + \tan^2\phi)^{1/2} = \frac{1}{\beta} dxdy\,\tan\theta \end{aligned} \tag{2.15}$$

Substitution of the temperature gradient (2.13) into Eq. (2.14) yields

$$\begin{aligned} aJ &= \frac{kv}{\alpha}(T_s - T_o)\tan\theta + \rho Lv\tan\theta \\ &= \rho v\tan\theta(c_p(T_s - T_o) + L) \end{aligned} \tag{2.16}$$

It is assumed that the laser beam has a Gaussian distribution intensity:

$$J = \frac{P}{\pi R^2} e^{-(x^2+y^2)/R^2} \tag{2.17}$$

where P is the laser beam power, and R is the beam spot radius. The slope of the groove surface along the x-axis, tanθ, can be determined as:

$$\tan\theta = \frac{\frac{aP}{\pi R^2} e^{-(x^2+y^2)/R^2}}{\rho v(c_p(T_s - T_o) + L)} \tag{2.18}$$

The change of the surface depth along the x-axis can be expressed as:

$$ds = dx \tan\theta \tag{2.19}$$

and the surface depth can be determined by integrating from $-\infty$ to the current x position:

$$s(x,y) = \int_{-\infty}^{x} ds + s_{-}(y) \tag{2.20}$$

or

$$s(x,y) = \int_{-\infty}^{x} \tan\theta \, dx + s_{-}(y) \tag{2.21}$$

By substituting tanθ into Eq. (2.21), the following expression for the surface depth s(x,y) can be obtained:

$$s(x,y) = \int_{-\infty}^{x} \frac{aP\, e^{-(x^2+y^2)/R^2}}{\pi R^2 \rho v (c_p(T_s - T_o) + L)}\, dx + s_{-} \tag{2.22}$$

The maximum depth of the groove $s_{max}$ can be achieved along the center line of the groove ($y = 0$):

$$s_{max} = \int_{-\infty}^{\infty} \frac{aP\, e^{-x^2/R^2}}{\pi R^2 \rho v (c_p(T_s - T_o) + L)}\, dx + s_{-}(0) \tag{2.23}$$

Thus the increment of the groove depth ($\Delta D$) for one pass of the laser beam over the workpiece, is

$$\Delta D = s_{max} - s_{-}(0) \tag{2.24}$$

The temperature at the top surface $T_s$ along the center line of the groove is assumed to be the melting temperature $T_m$. Although $T_s$ varies from $T_m$ at the cutting front to $T_o$ far away from the cutting front, the resulting error in groove depth should be negligible because the exponential term in Eq. (2.23) becomes negligible for the part of the surface where the temperature is not $T_m$. Consequently, $\Delta D$ due to one pass of the laser beam over the groove can be obtained as:

$$\Delta D = \frac{aP\pi^{1/2}R}{\pi R^2 \rho v (c_p(T_s - T_o) + L)} = \frac{2aP}{\pi^{1/2} \rho v d (c_p(T_s - T_o) + L)} \tag{2.25}$$

where d is the beam spot diameter, $d \equiv 2R$. The incremental groove depth is proportional to P/vd, which is the energy input per unit area of the workpiece. Also, $\Delta D$ is small for materials with high melting point and high latent heat of evaporation. In comparison with the groove depth in grooving, the kerf depth in through-cutting is mathematically derived in Appendix A.

### 2.2.2 Modified Solution

The previous analytical solution can predict groove depths well especially when scanning velocity is relatively high. This is because the assumptions made in the analytical solution are valid only for high scanning velocities. In order to obtain a better analytical solution, two modifications are considered, compared with the analytical solution: change in conduction direction, and area change in the direction of conduction heat.

In order to derive the governing equation, an infinitesimal volume in the n-direction is considered, as shown in Fig. 2.4. The infinitesimal surface is inclined $\theta$ and $\phi$ with respect to the x-, and y- axis, respectively. The area of heat conducted at n is A. Solid material is fed into and moved out of the control volume at a speed of v in the x-direction. The mass flow rates at 1 and 2 are

$$\dot{m}_1 = \rho v_n A \tag{2.26}$$

$$\dot{m}_2 = \rho v_n A + \frac{d}{dn}(\rho v_n A)dn \tag{2.27}$$

where $v_n$ is the velocity component of material fed into the control volume in the n-direction. The net mass flow rate out of the control volume through the side walls is

$$\dot{m}_s = \dot{m}_2 - \dot{m}_1 \tag{2.28}$$

The heat into the control volume is

$$-kA\frac{dT}{dn} + \rho c_p v_n A(T - T_o) + \frac{d}{dn}\left(\rho c_p v_n A(T - T_o)\right)dn \tag{2.29}$$

Assuming that the temperature of the material moving out of the control volume through the side walls is T + (dT/dn)dn/2, the heat out of the control volume is

$$-kA\frac{dT}{dn} - k\frac{d}{dn}\left(A\frac{dT}{dn}\right) + \rho c_p v_n A(T - T_o) + m_s c_p\left(T + \frac{1}{2}\frac{dT}{dn} - T_o\right) \tag{2.30}$$

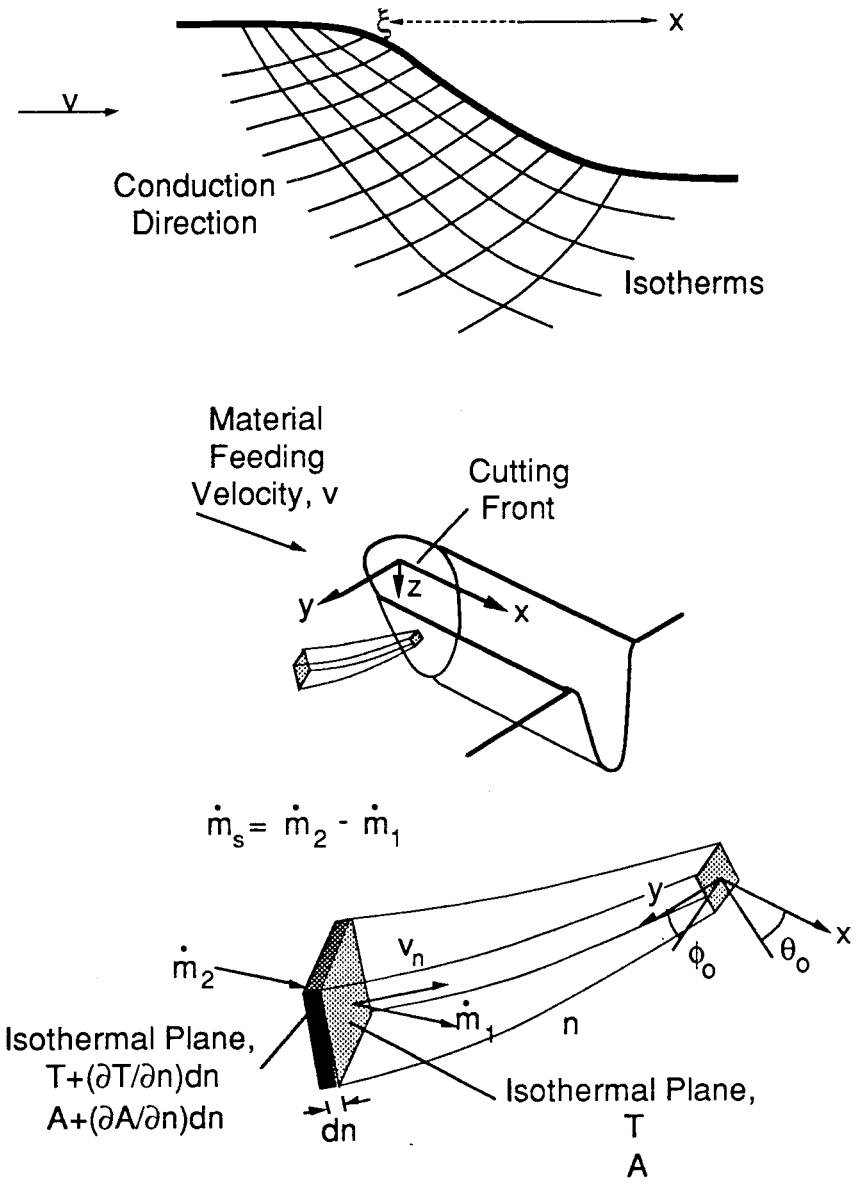



Fig. 2.4: Control Volume inside Solid Medium.

By equating heats in and out of the control volume, the following heat balance can be obtained

$$\rho c_p v_n A \frac{dT}{dn} = - k \frac{d}{dn}\left( A \frac{dT}{dn} \right) \tag{2.31}$$

The area ratio g(n) is defined as A(n) divided by A(0) (infinitesimal cutting front area).

$$g(n) = \frac{A(n)}{A(0)} \tag{2.32}$$

Divided by A(0), which is independent of the n-coordinate, Eq. (2.31) becomes

$$\frac{v_n}{\alpha} g \frac{dT}{dn} = - \frac{d}{dn}\left( g \frac{dT}{dn} \right) \tag{2.33}$$

Boundary conditions are

$$n = 0, T = T_s \tag{2.34}$$

$$n \rightarrow \infty, T = T_o \tag{2.35}$$

where $T_s$ is the surface temperature, and $T_o$ is the ambient temperature. From Eq. (2.33) the temperature distribution inside the solid can be derived.

$$T = C_1 \int_0^n \frac{e^{-\int_0^n \frac{v_n}{\alpha} dn}}{g} dn + C_2 = C_1 B(n) + C_2 \tag{2.36}$$

where:

$$B(n) = \int_0^n \frac{1}{g} e^{-\int_0^n \frac{v_n}{\alpha} dn} dn \tag{2.37}$$

Applying boundary conditions to Eq. (2.36), the temperature distribution is obtained as a function of n.

$$\frac{T - T_o}{T_s - T_o} = 1 - \frac{B(n)}{B(\infty)} \tag{2.38}$$

For an arbitrary n, the velocity component $v_n$ is

$$v_n = v \frac{\tan\theta}{(1 + \tan^2\theta + \tan^2\phi)^{1/2}} \tag{2.39}$$

Let $\xi$ be a coordinate in the opposite direction of x ($\xi = - x$) from the cutting front surface into the solid. The increments of n and $\xi$ can be related as:

$$dn = d\xi \frac{(1 + \tan^2\theta + \tan^2\phi)^{1/2}}{\tan\theta} \tag{2.40}$$

From Eqs. (2.39) and (2.40)

$$v_n \, dn = v \, d\xi \tag{2.41}$$

From Eq. (2.37), B(n) becomes

$$B(n) = \int_0^n \frac{1}{g} e^{-\int_0^n \frac{v_n}{\alpha} dn} dn = \int_0^n \frac{1}{g} e^{-\frac{v\xi}{\alpha}} dn \tag{2.42}$$

The area ratio can be determined as (Fig. 2.5):

$$g = \frac{A(n)}{A(0)} = \frac{dx'dy' \, (1 + \tan^2\theta + \tan^2\phi)^{1/2}}{dxdy \, (1 + \tan^2\theta_o + \tan^2\phi_o)^{1/2}} \tag{2.43}$$

Substitution of Eqs. (2.43) and (2.40) into equation (2.42), B can be rewritten as

$$B(\xi) = \int_0^{\xi} e^{-\frac{v\xi}{\alpha}} \frac{dxdy\,(1 + \tan^2\theta_o + \tan^2\phi_o)^{1/2}}{dx'dy'\,(1 + \tan^2\theta + \tan^2\phi)^{1/2}} \frac{(1 + \tan^2\theta + \tan^2\phi)^{1/2}}{\tan\theta}\, d\xi \tag{2.44}$$

The inclination of the cutting front surface ($\theta_o$ and $\phi_o$) is independent of n and $\xi$. Thus,

$$B(\xi) = \frac{(1 + \tan^2\theta_o + \tan^2\phi_o)^{1/2}}{\tan\theta_o} \int_0^{\xi} e^{-\frac{v\xi}{\alpha}} \frac{dxdy\,\tan\theta_o}{dx'dy'\,\tan\theta}\, d\xi \tag{2.45}$$

As shown in Fig. 2.5, the area ratio, dx'dy'/dxdy, can be approximated as:

$$\frac{dx'dy'}{dxdy} = \frac{\frac{1}{2}(R + \xi)^2\left(\frac{\pi}{2}\right)}{\frac{1}{2}R^2\left(\frac{\pi}{2}\right)} = \left(1 + \frac{\xi}{R}\right)^2 \tag{2.46}$$

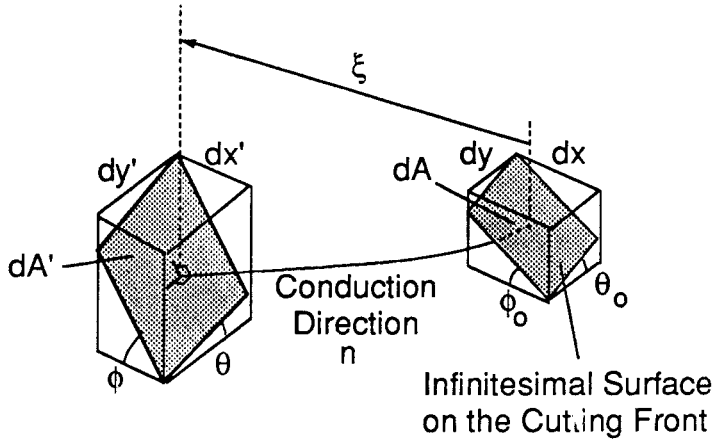



Fig. 2.5: Isotherm Surfaces in the Conduction Direction.

Therefore, $B(\xi)$ becomes

$$B(\xi) = \frac{(1 + \tan^2\theta_o + \tan^2\phi_o)^{1/2}}{\tan\theta_o} \int_0^{\xi} \frac{1}{\left(1 + \frac{\xi}{R}\right)^2} e^{-\frac{v\xi}{\alpha}} \left(\frac{\tan\theta_o}{\tan\theta}\right) d\xi \tag{2.47}$$

or

$$B(\xi) = \frac{(1 + \tan^2\theta_o + \tan^2\phi_o)^{1/2}}{\tan\theta_o} I(\xi) \tag{2.48}$$

where

$$I(\xi) = \int_0^{\xi} \frac{1}{\left(1 + \frac{\xi}{R}\right)^2} e^{-\frac{v\xi}{\alpha}} \left(\frac{\tan\theta_o}{\tan\theta}\right) d\xi \tag{2.49}$$

In order to determine $I(\xi)$, the slope ratio, $\tan\theta_o/\tan\theta$ should be expressed as a function of $\xi$. Since $\theta=\theta_o$ at $\xi=0$ and $\theta=90°$ as $\xi\rightarrow\infty$, the angle ratio can be assumed as:

$$\frac{\tan\theta_o}{\tan\theta} = e^{-\frac{\xi}{b}} \tag{2.50}$$

where b is a characteristic length which is approximated as the beam spot diameter, d. Then $I(\xi)$ becomes

$$I(\xi) = \int_0^{\xi} \frac{1}{\left(1 + \frac{\xi}{R}\right)^2} e^{-\left(\frac{v}{\alpha} + \frac{1}{b}\right)\xi} d\xi \tag{2.51}$$

Define $\eta$ such as:

$$\eta = 1 + \frac{\xi}{R} \tag{2.52}$$

$I(\xi)$ can be expressed as a function of $\eta$.

$$I(\eta) = \int_1^{\eta} \frac{R}{\eta^2} e^{-\left(\frac{v}{\alpha}+\frac{1}{b}\right)R(\eta - 1)} d\eta \tag{2.53}$$

Defining $\sigma$ as

$$\sigma = \left(\frac{v}{\alpha} + \frac{1}{b}\right) R = \left(\frac{vb}{\alpha} + 1\right) \frac{R}{b} \tag{2.54}$$

$I(\eta)$ can be expressed as:

$$I(\eta) = R\, e^{\sigma} \int_1^{\eta} \frac{1}{\eta^2} e^{-\sigma\eta} d\eta \tag{2.55}$$

$I(\infty)$ can be determined as:

$$I(\infty) = R\, e^{\sigma} \int_1^{\infty} \frac{1}{\eta^2} e^{-\sigma\eta} d\eta = R + \sigma e^{\sigma} Ei(-\sigma) \tag{2.56}$$

$I(\infty)$ represents a characteristic length of a heat affected zone in the $\xi$ direction. Fig. 2.6 shows that $I(\infty)$ decreases monotonically with increase in $\sigma$. Since $\sigma$ is a linear function of the scanning velocity, $I(\infty)$ is large for small scanning velocities and small for large scanning velocities.

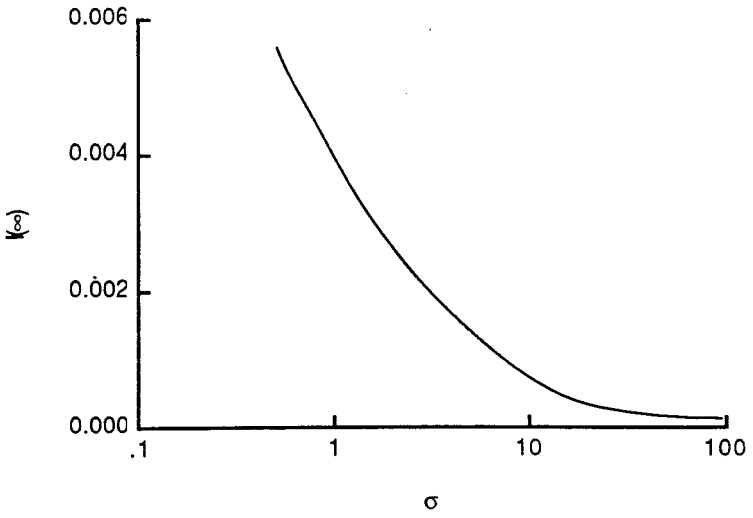



Fig. 2.6: I(∞) vs. σ.

The heat balance at the cutting front is

$$aJ = \rho L v \tan\theta_o - k\left(\frac{dT}{dn}\right)_{n=0}(1 + \tan^2\theta_o + \tan^2\phi_o)^{1/2} \tag{2.57}$$

The temperature gradient at the cutting front can be determined from the temperature distribution.

$$\left(\frac{dT}{dn}\right)_{n=0} = -\frac{(T_s - T_o)}{B(\infty)}\frac{dB(0)}{dn} \tag{2.58}$$

Since dB(0)/dn is

$$\frac{dB(0)}{dn} = \left(\frac{1}{g(n)}e^{-\int_0^n \frac{v_n}{\alpha}dh}\right)_{n=0} = 1 \tag{2.59}$$

the conduction heat at the cutting front into the material can be obtained as:

$$-k\left(\frac{dT}{dn}\right)_{n=0} = \frac{k(T_s - T_o)}{B(\infty)} \tag{2.60}$$

The heat balance at the cutting front surface can be written as:

$$aJ = \rho L v \tan\theta_o + \frac{k(T_s - T_o)}{B(\infty)}(1 + \tan^2\theta_o + \tan^2\phi_o)^{1/2} \tag{2.61}$$

$$aJ = \rho L v \tan\theta_o + \frac{k(T_s - T_o)}{I(\infty)}\tan\theta_o \tag{2.62}$$

$$aJ = \left(\rho L v + \frac{k(T_s - T_o)}{I(\infty)}\right)\tan\theta_o \tag{2.63}$$

The cutting front angle can be expressed as:

$$\tan\theta_o = \frac{\frac{aP}{\pi R^2} e^{-(x^2+y^2)/R^2}}{\rho L v + \frac{k(T_s - T_o)}{I(\infty)}} \tag{2.64}$$

The surface depth is

$$s(x,y) = \int_{-\infty}^{x} \tan\theta_o dx \tag{2.65}$$

Depth increment by one laser pass can be determined as:

$$\Delta D = \int_{-\infty}^{\infty} \tan\theta_o dx \tag{2.66}$$

$$\Delta D = \frac{2aP}{\pi^{1/2} d \left( \rho Lv + \frac{k(T_s - T_o)}{I(\infty)} \right)} \tag{2.67}$$

The second term of the denominator in Eq. (2.67) is related to the conduction heat. Compared with Eq. (2.25), Eq. (2.67) has a different denominator. This is because the changes in conduction direction and conduction area are considered in the modified solution. The ratio between the conduction heats predicted by the analytical and the modified solution can be obtained from Eqs. (2.25) and (2.67) as

$$\frac{\rho c_p v (T_s - T_o)}{\left( \frac{k (T_s - T_o)}{I(\infty)} \right)} = \frac{vI(\infty)}{\alpha} \tag{2.68}$$

As shown in Fig. 2.7, for large scanning velocities (or large $\sigma$), the ratio becomes unity, which means that the conduction heat predicted by the analytical solution is the same as that by the modified solution. For small scanning velocities, the ratio becomes less than unity. Small scanning velocities allow large beam interaction time with the material, leading to large heat affected zones. The conduction heat predicted by the analytical solution is smaller than that by the modified solution. This means that the analytical solution does not predict accurately the variation of a heat affected zone with respect to the scanning velocity.

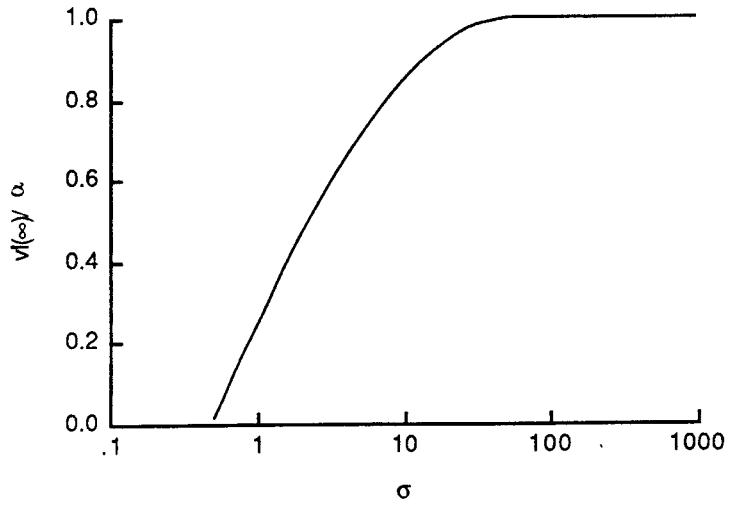



Fig. 2.7: Ratio of Conduction Heats Predicted by Analytical and Modified Solutions.

### 2.2.3 Numerical Solution

In the previous sections, two theoretical solutions were obtained. Since the two solutions were based on approximation of the temperature distribution inside a solid, they may not be accurate, if the approximation is not valid. Thus, a numerical analysis is needed to obtain a more accurate solution. For a numerical analysis, a limited region is taken into consideration, as shown in Fig. 2.8(b), due to the symmetry the plane (y = 0) can be an adiabatic boundary.

$$x = x_{max}: \qquad \partial T/\partial x = 0 \tag{2.69}$$

$$x = x_{min};\ y = y_{max};\ z = z_{min}: \qquad T = T_o \tag{2.70}$$

$$y = y_{min}: \qquad \partial T/\partial y = 0 \tag{2.71}$$

At the top surface, an energy balance is another boundary condition: the laser beam melts material and heats the surrounding material. In the control volume in Fig. 2.9, the following energy balance can be derived.

$$aJ(x,y,z)A_1 = -k\left(\frac{\partial T}{\partial n}\right)A + \rho L v A_2 \tag{2.72}$$

where n is a coordinate normal to the surface pointing into the solid. From the geometry of the control volume, the following relations among areas can be obtained:

$$\frac{A_1}{A} = \left(1 + \left(\frac{\partial s}{\partial x}\right)^2 + \left(\frac{\partial s}{\partial y}\right)^2\right)^{-1/2} \tag{2.73}$$

$$\frac{A_2}{A} = \left(\frac{\partial s}{\partial x}\right)\left(1 + \left(\frac{\partial s}{\partial x}\right)^2 + \left(\frac{\partial s}{\partial y}\right)^2\right)^{-1/2} \tag{2.74}$$

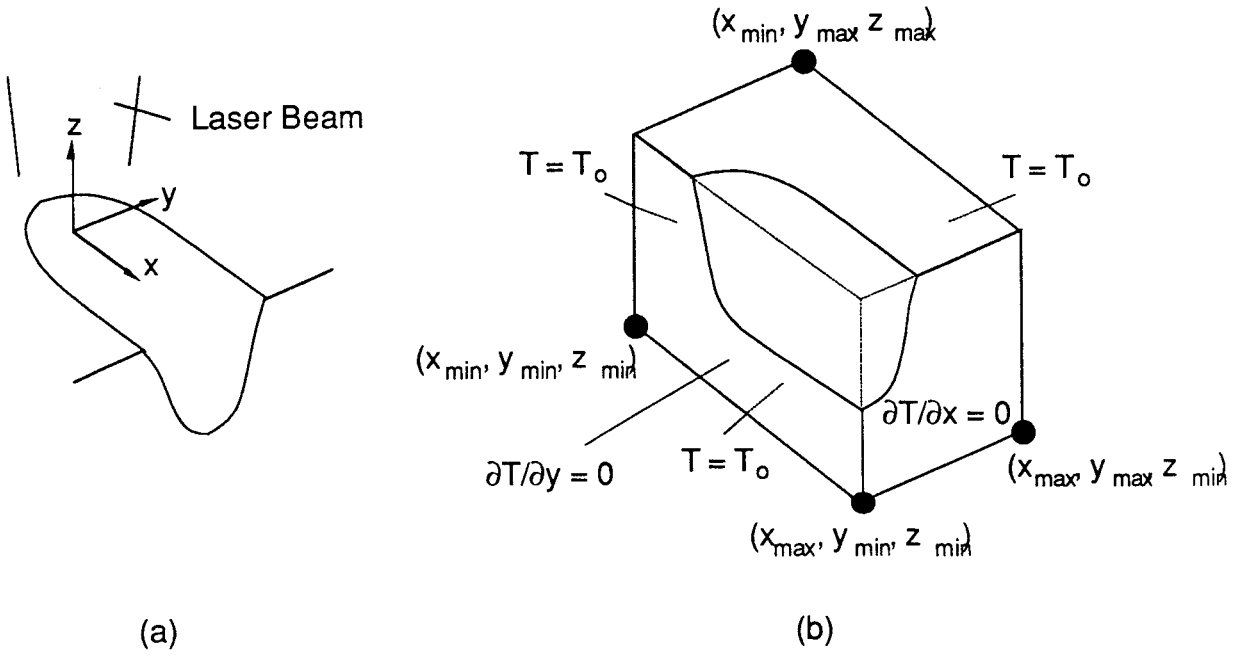



Fig. 2.8: Configuration of the Laser Beam and a Coordinate System (a) and Boundaries for Numerical Analysis (b)

Substituting of Eqs. (2.73) and (2.74) into Eq.(2.72) yields:

$$\frac{a}{\gamma} J(x,y,z) = - k\left(\frac{\partial T}{\partial n}\right) + \frac{\rho L v}{\gamma}\left(\frac{\partial s}{\partial x}\right) \tag{2.75}$$

where:

$$\gamma = \left(1 + \left(\frac{\partial s}{\partial x}\right)^2 + \left(\frac{\partial s}{\partial y}\right)^2\right)^{1/2} \tag{2.76}$$

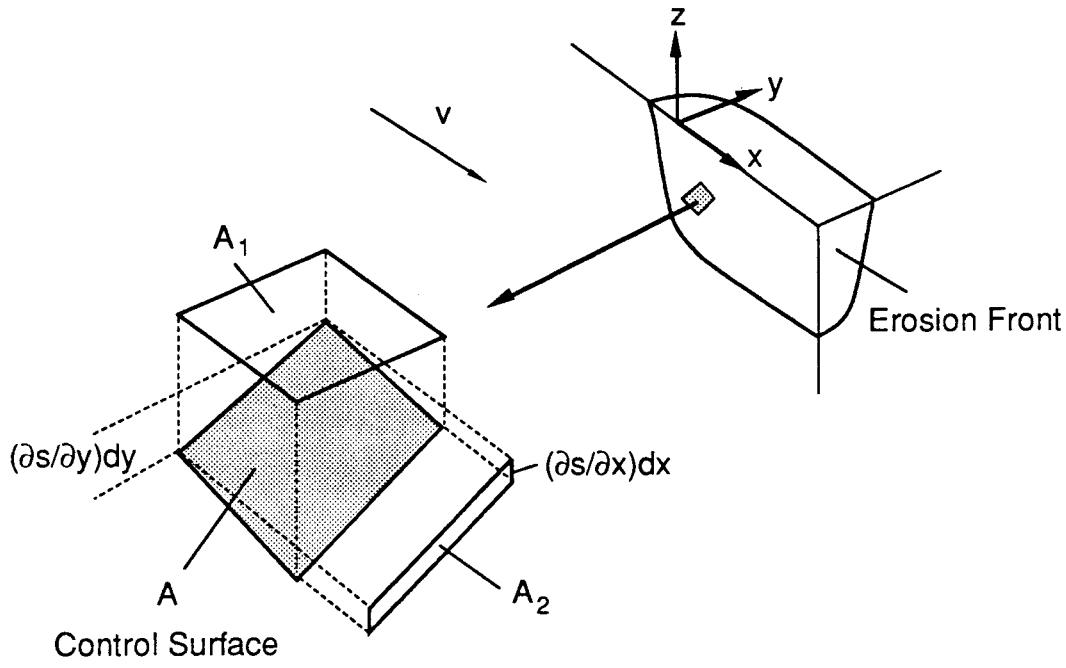



Fig. 2.9: Control Surface at Cutting Front in Numerical Analysis

The Gaussian laser beam intensity, including beam defocusing effect, can be expressed as:

$$J(x,y,z) = \frac{aP}{\pi r(z)^2} \exp\left( - \frac{x^2 + y^2}{r(z)^2} \right) \tag{2.77}$$

where:

$$r(z) = R\left( 1 + \left( \frac{\lambda_L z}{\pi R^2} \right)^2 \right)^{1/2} \tag{2.78}$$

Since the problem has a boundary whose location is to be determined as a solution, the method of lines is suitable for solving that type of problem. The method of lines has been developed for multi-dimensional heat transfer problems by Meyer [50,51]. According to the method of lines, Eq. (2.1) is transformed into a set of ordinary differential equation, by replacing all derivatives with finite difference forms except one with respect to z-direction:

$$\frac{v}{\alpha}\frac{T_{i+1} - T_{i-1}}{2\Delta x} = \frac{T_{i+1} - 2T + T_{i-1}}{\Delta x^2} + \frac{T_{j+1} - 2T + T_{j-1}}{\Delta y^2} + \frac{\partial^2 T}{\partial z^2} \tag{2.79}$$

Eq. (2.79) is a boundary-value differential equation, requiring boundary conditions at z = $z_{min}$ and the top surface. Eq. (2.79) can be converted into initial-value differential equations by the Riccati transformation. By defining a new function F,

$$\frac{\partial T}{\partial z} = \frac{1}{k} F(z) \tag{2.80}$$

Eq. (2.79) becomes:

$$\frac{\partial F}{\partial z} = -\frac{k}{\Delta x^2}(T_{i+1} + T_{i-1} - 2T) - \frac{k}{\Delta y^2}(T_{j+1} + T_{j-1} - 2T) + \frac{\rho c v}{2\Delta x}(T_{i+1} - T_{i-1}) \tag{2.81}$$

The Riccati transformation takes advantage of a relation between the functions F and T:

$$F(z) = G(z)T + H(z) \tag{2.82}$$

where G(z) and H(z) are the Riccati functions. From the Riccati transformation, three equations are resulted: two equations for a forward sweep and one for a backward sweep. In the forward sweep the top surface (cutting front) location is determined from the two equations, and in the backward sweep the temperatures along the line are calculated from one equation. The two equations for the forward sweep are:

$$\frac{dG}{dz} = \frac{4k}{\Delta x^2} - \frac{1}{k} G^2 \tag{2.83}$$

$$\frac{dH}{dz} = -\frac{k}{\Delta x^2}(T_{i+1} + T_{i-1}) - \frac{k}{\Delta y^2}(T_{j+1} - T_{j-1}) + \frac{\rho c v}{2\Delta x}(T_{i+1} - T_{i-1}) - \frac{1}{k} GH \tag{2.84}$$

The initial values for G and H can be determined from the boundary condition (2.70):

$$k\frac{\partial T}{\partial z} = k\frac{T - T_o}{\Delta z} = GT + H \tag{2.85}$$

Since Eq. (2.85) holds for arbitrary T, the initial values for G and H can be determined as:

$$G(z_{min}) = \frac{k}{\Delta z} \tag{2.86}$$

$$H(z_{min}) = -\frac{kT_o}{\Delta z} \tag{2.87}$$

Since G in Eq. (2.83) is independent of temperature, the solution for G can be obtained prior to the calculation of temperature and surface profile. From the above initial conditions, G can be determined as:

$$G = A\left(\frac{1 + \left(\frac{G(z_{min}) - A}{G(z_{min}) + A}\right)e^{-2A(z - z_{min})/k}}{1 - \left(\frac{G(z_{min}) - A}{G(z_{min}) + A}\right)e^{-2A(z - z_{min})/k}}\right) \tag{2.88}$$

where:

$$A = \left(2k^2\left(\frac{1}{\Delta x^2} + \frac{1}{\Delta y^2}\right)\right)^{1/2} \tag{2.89}$$

The function H can be solved by integrating Eq. (2.84) from $z_{min}$ to the top surface.

The energy balance equation at the top surface can be used to check if ablation takes place. A function, C, is defined by arranging Eq. (2.75).

$$C = aJ - \rho Lv\left(\frac{\partial s}{\partial x}\right) - (GT_m + H)\left(1 + \left(\frac{\partial s}{\partial x}\right)^2 + \left(\frac{\partial s}{\partial y}\right)^2\right) \tag{2.90}$$

At each node, C is calculated in the forward sweep to check if the energy balance (2.75) is satisfied. Since the energy balance (2.75) is satisfied at the cutting front, the cutting front is located where C vanishes. If C does not change its sign before the previously made surface is reached, no ablation takes place. In this case, the surface temperature instead of the surface location is determined from the energy balance as follows:

$$\frac{a}{\beta^2} J = k(GT_s + H) \tag{2.91}$$

In the backward sweep, the temperatures along the lines are determined from the top surface. The equation for the backward sweep is:

$$\frac{\partial T}{\partial z} = \frac{1}{k}(GT + H) \tag{2.92}$$

At the cutting front of the top surface, the temperature is the melting temperature, $T_m$, and at other surface is the temperature calculated from Eq. (2.91).

Iterations are repeated until the temperature and surface profile reach steady-state. During the calculation, updated temperatures, if available, are used. However, for the surface profile, the values calculated in the previous iteration are used, since a large slope can cause a numerical instability. A new temperature is obtained by an over-relaxation method:

$$T^m = T^{m-1} + \omega(T - T^{m-1}) \tag{2.93}$$

The numerical computer program is listed in Appendix B.

## 2.3 Gas Jet Interaction and Molten Layer Behavior

During beam interaction with a material, a molten layer is formed. One of the main goals in laser grooving is maximum expulsion of the molten material. In grooving, the

driving force for molten material expulsion is the pressure gradient along the cutting front, which can be created by the use of a gas jet.

In laser through-cutting, a coaxial jet is used to create a large pressure difference between the top and bottom of the kerf. This pressure difference, shown in Fig. 2.10 (a), forms a downward driving force, which expels molten material through the bottom of the kerf. In laser grooving, however, this driving force would cause molten material to be expelled towards the bottom of the groove and resolidify on the established groove wall. A favorable driving force for laser grooving (which expels material out from the top of the cutting front) can be formed by creating a pressure gradient with a high pressure at the bottom of the cutting front and low pressure at the top, as shown in Fig. 2.10 (b). Due to the geometric difficulty of removing molten material in grooving, an off-axial jet is used.

Investigations of gas jet effects in laser machining have been largely limited to the use of coaxial nozzles in through-cutting applications. In [52] high pressure (up to 20 bars) cutting with a variety of gas mixtures was investigated. In [53] the jet flow from nozzles used in laser through-cutting was investigated. A highly under-expanded jet is found to create a Mach shock disk above the workpiece that reduces the stagnation pressure at the workpiece and the cutting efficiency. In [54] the optimum values of parameters resulting in a high pressure on the workpiece were investigated. The effect of jet parameters on the pressure distribution at the cutting front in grooving was investigated in [55]. A theoretical analysis on a gas jet was done in through-cutting in [34]. In [56] the forces exerted by the gas jet on the molten layer in laser cutting were investigated theoretically by solving the equations of motion of the gas flow under the assumption that the gas flow is laminar within the cutting kerf, and the flow is subsonic. This assumption is not realistic, since the operating reservoir pressures in most applications cause the jet flow to be supersonic. In [56], it was found that momentum is transferred from the gas jet to the cutting front by a pressure gradient and friction, and both effects are of the same order. Donaldson et al. [57] found in their experiments the pressure and velocity distribution along the axis of various free jets (subsonic and supersonic) and investigated the impinging jet behavior. In [58] a breakaway zone at the interaction between a supersonic under-expanded jet and a flat plate was discussed. Related to the boost blast situation, supersonic jet impingement on a surface was studied [59-61]. Although such things as flow rate, nozzle diameter, etc. were on a larger scale in these studies than those in laser machining, the findings are helpful in understanding the flow field and pressure distribution at the surface interacted with a supersonic jet.

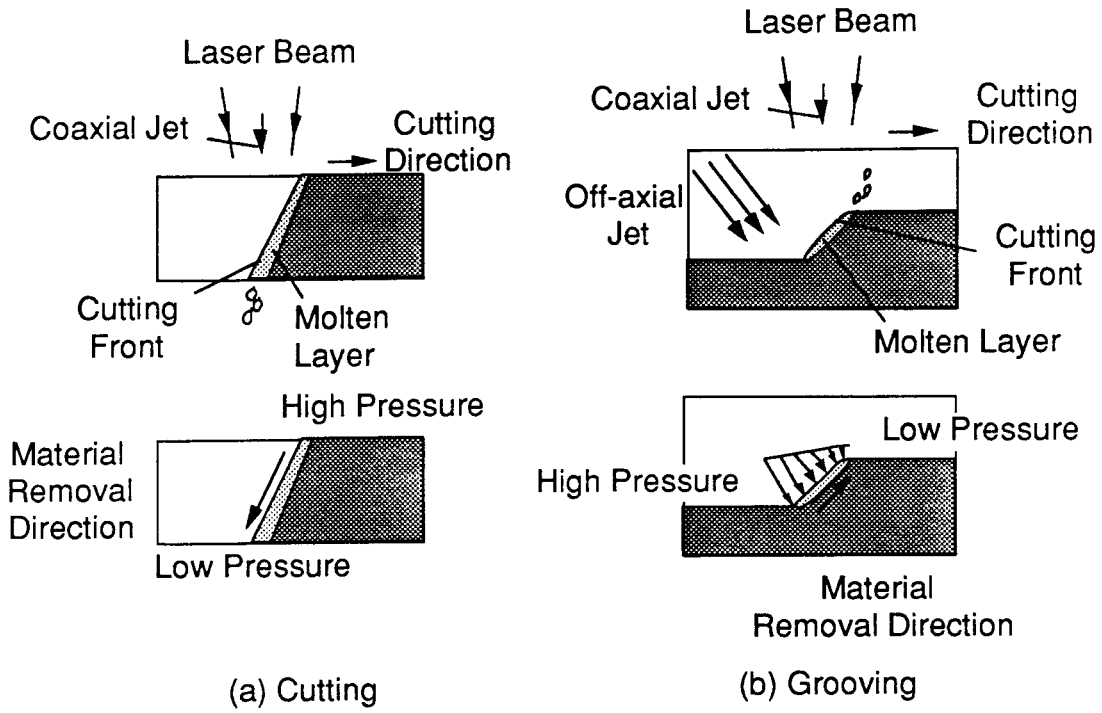



Fig. 2.10: Driving Forces for Molten Material Removal.

For a simply convergent nozzle, if a reservoir pressure is higher than 1.89 bar in an air jet, the flow after the nozzle exit becomes supersonic. A supersonic jet has a higher jet stagnation pressure than that of a subsonic one. Thus, it is important to investigate the applicability of a supersonic jet to the process of laser grooving, since high pressure is generally more effective for removing molten material out of the groove. In an under-expanded supersonic jet, a series of cells is formed, and oblique shocks develop near the jet boundary. For the reservoir pressure higher than 3.4 bar, a Mach shock occurs in the cell (Fig. 2.11), and another oblique shock is originated from the circumference of the Mach shock. Across a Mach shock, the stagnation pressure drops substantially [62-64] and the downstream (inner) jet becomes subsonic. After a Mach shock, the stagnation pressure of the inner jet is determined from the upstream Mach number. Across the oblique shock, the outer jet is still supersonic. Those jets in different states are separated by slip streams. Flowing inside the slip stream tube, the inner jet is accelerated by the outer jet, and becomes supersonic again. This is a highly irreversible process during which the stagnation pressure of the inner jet increases.

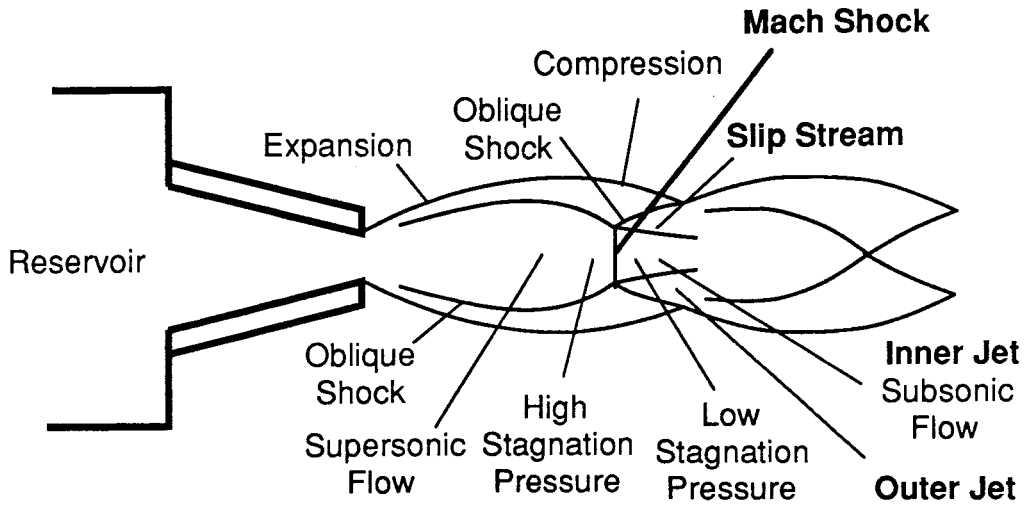



Fig. 2.11: Under-Expanded Supersonic Jet with a Mach Shock Disc.

When a body is located before the Mach shock location or after the slip stream, the jet impinging the body is supersonic, and a surface shock occurs in front of the body. When a supersonic jet impinges on a blunt body, the location of a normal shock has been theoretically obtained for a uniform jet [65-67] and for an under-expanded jet [59, 60, 68].

Supersonic jet interaction with a grooved workpiece is a complicated phenomenon. The previously mentioned literature might be helpful only to understand the jet behavior qualitatively. From a quantitative point of view, it is not well understood. In this thesis, an order of magnitude analysis is employed. It is assumed that the pressure difference between the jet stagnation pressure and the ambient pressure drives molten material out of a groove. The calculation of jet stagnation pressures will be explained in Chapter 3. As shown in Fig. 2.12, the driving force for molten material expulsion can be approximated as

$$\frac{dp}{dx} = \frac{(p_s - p_a)}{l_c} \tag{2.94}$$

where $p_s$ is the jet stagnation pressure, $p_a$ is the ambient pressure, and $l_c$ is the contact length between the jet and the cutting front. The contact length can be approximated as the groove depth, $\Delta D$.

With the known maximum driving force for the molten material removal, the molten layer thickness can be estimated. An order of magnitude analysis is also employed. In Fig. 2.12, the mass balance in the control volume is

$$\int_0^h \rho u\, dy + \frac{d}{dx}\left(\int_0^h \rho u\, dy\right) dx = \int_0^h \rho u\, dy + \rho v \sin\theta\, dx \tag{2.95}$$

or

$$\frac{d}{dx}\int_0^h \rho u\, dy = \rho v \sin\theta \tag{2.96}$$

The momentum balance in the control volume is

$$\left(p - \left(p + \frac{dp}{dx}dx\right)\right) h + \tau_g dx - \tau_w dx = \int_0^h \rho u^2 dy + \frac{d}{dx}\left(\int_0^h \rho u^2 dy\right) dx$$

$$- \int_0^h \rho u^2 dy - \rho v \sin\theta\, dx\, (-v\cos\theta) \tag{2.97}$$

where $\tau_w$ is the shear stress exerted by the wall to the molten layer, and $\tau_g$ is the shear stress by the gas jet to the molten layer. Eq. (2.97) can be rewritten as

$$-\frac{dp}{dx}h + \tau_g - \tau_w = \frac{d}{dx}\left(\int_0^h \rho u^2 dy\right) \tag{2.98}$$

Eq. (2.98) requires the velocity profile in the molten layer. The velocity profile depends on the flow type (laminar or turbulent). Although the gas jet flow is highly turbulent, the molten material flow could be laminar due to the molten material viscosity. For laminar and turbulent flows, two different estimations of molten layer thickness are obtained in the following.

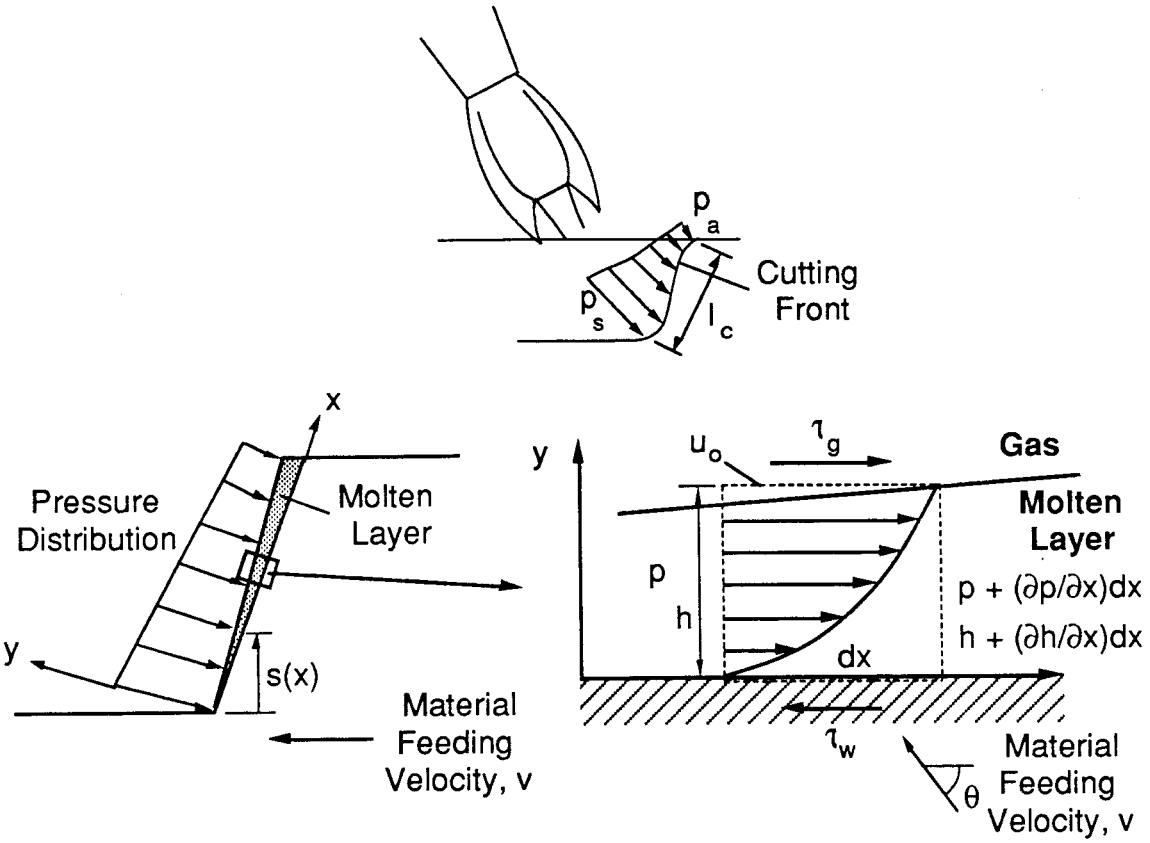



Fig. 2.12: Molten Layer and Control Volume.

**Case I) Laminar Flow**

For laminar molten material flow, the shear stresses and the integral terms in Eq. (2.98) can be expressed as

$$\tau_g = \mu\left(\frac{\partial u}{\partial y}\right)_{y=h} = \frac{\mu u_o}{h}\left(\frac{\partial u^*}{\partial y^*}\right)_{y^*=1} \tag{2.99}$$

$$\tau_w = \mu\left(\frac{\partial u}{\partial y}\right)_{y=0} = \frac{\mu u_o}{h}\left(\frac{\partial u^*}{\partial y^*}\right)_{y^*=0} \tag{2.100}$$

$$\int_0^h \rho u\, dy = \rho u_o h \int_0^1 u^* dy^* = c_d \rho u_o h \tag{2.101}$$

$$\int_0^h \rho u^2 dy = \rho u_o^2 h \int_0^1 u^{*2} dy^* = c_m \rho u_o^2 h \tag{2.102}$$

where $\mu$ is the dynamic viscosity of the molten material, $u_o$ is the maximum velocity in the molten material flow, $u^*$ is the non-dimensional velocity, $y^*$ is the non-dimensional coordinate in the y-direction, $c_d$ is the displacement thickness coefficient, and $c_m$ is the momentum thickness coefficient.

$$-\frac{dp}{dx} h + \frac{\mu u_o}{h}\left(\left(\frac{\partial u^*}{\partial y^*}\right)_{y^*=1} - \left(\frac{\partial u^*}{\partial y^*}\right)_{y^*=0}\right) = \frac{d}{dx}(c_m \rho u_o^2 h) \tag{2.103}$$

From the mass balance of the material fed into the molten layer, the maximum velocity, $u_o$, can be expressed as

$$c_d \rho \frac{d}{dx}(u_o h) = \rho v \sin\theta \tag{2.104}$$

$$u_o h = \frac{v}{c_d}\int_0^x \sin\theta \, dx = \frac{vs}{c_d} \tag{2.105}$$

where s is the surface height from the groove bottom to x (in Fig 2.12). Substitution of Eq. (2.105) into Eq. (2.103) yields

$$-\frac{dp}{dx} h + \frac{\mu v s}{c_d h^2}\left(\frac{\partial u^*}{\partial y^*}\right)_{y^*=1} = \frac{\mu v s}{c_d h^2}\left(\frac{\partial u^*}{\partial y^*}\right)_{y^*=0} + \frac{d}{dx}\left(c_m \rho \frac{v^2 s^2}{c_d^2 h}\right) \tag{2.106}$$

Eq. (2.106) consists of four force components: pressure difference driving force, frictional driving force, viscous force, and momentum increase.

According to [56], the driving force for molten material ejection consists of two components: pressure gradient and friction, and the two components are of the same order of magnitude. A pressure flow has the following velocity profile:

$$u^* = 2y^* - y^{*2} \tag{2.107}$$

A steady shear flow has a linear velocity profile

$$u^* = y^* \tag{2.108}$$

The velocity profile is assumed to be the average of the two profiles (2.107) and (2.108).

$$u^* = \frac{3}{2} y^* - \frac{1}{2} y^{*2} \tag{2.109}$$

The non-dimensional velocity gradients and the thickness coefficients in Eq. (2.106) can be determined as

$$\left(\frac{\partial u^*}{\partial y^*}\right)_{y^*=0} = \frac{3}{2} \tag{2.110}$$

$$\left(\frac{\partial u^*}{\partial y^*}\right)_{y^*=1} = \frac{1}{2} \tag{2.111}$$

$$c_d = \int_0^1 \left(\frac{3}{2} y^* - \frac{1}{2} y^{*2}\right) dy^* = \frac{1}{2} \tag{2.112}$$

$$c_m = \int_0^1 \left(\frac{3}{2} y^* - \frac{1}{2} y^{*2}\right) dy^* = \frac{17}{40} \tag{2.113}$$

Substituting Eqs. (2.110-113) to Eq.(2.106), the following equation can be derived.

$$-\frac{dp}{dx}h = \frac{\mu\ vs}{h\ c_d h} + \frac{d}{dx} c_m \rho \frac{v^2 s^2}{c_d^2 h} \tag{2.114}$$

The ratio between the first and the second term is

$$\frac{\dfrac{\mu\ vs}{h\ c_d h}}{\dfrac{d}{dx}\left(c_m \rho \dfrac{v^2 s^2}{c_d^2 h}\right)} \sim \frac{\dfrac{\mu v(\Delta D)}{h^2}}{\left(\dfrac{\rho v^2 (\Delta D)^2}{h}\right)} \sim \frac{\mu}{\rho v h} \tag{2.115}$$

The ratio depends on the inverse of Reynolds number based on the scanning velocity and the molten layer thickness. For the range of scanning velocity and the molten material viscosity, the ratio is of order of 1. Since s and x are of the order of the groove depth ($\Delta D$) and dp/dx can be approximated as $\Delta p/\Delta D$, the molten layer thickness can be estimated by solving the following equation:

$$\frac{\Delta p}{\Delta D} h = \frac{\mu v \Delta D}{c_d h^2} + \frac{c_m \rho v^2 \Delta D}{c_d^2 h} \tag{2.116}$$

Since in Eq. (2.116) the molten layer thickness at the top of the cutting front is obtained, the average molten layer thickness is approximately half of the thickness at the top. The average molten layer thickness is used in calculating the groove depth.

### Case II) Turbulent Flow

In a turbulent flow, shear stress and velocity distribution are different from those in a laminar flow. Thus, a momentum balance for a turbulent flow is different from Eq. (2.116). It is assumed that $\tau_g$ is negligible compared with $\tau_w$. For turbulent flow, the wall shear stress can be expressed as [69]

$$\tau_w = 0.0228\ \rho u_o^2 \left(\frac{\nu}{u_o h}\right)^{1/4} \tag{2.117}$$

The typical velocity profile for a turbulent flow is

$$\frac{u}{u_o} = \left(\frac{y}{h}\right)^{1/7} \tag{2.118}$$

or

$$u^* = y^{*1/7} \tag{2.119}$$

The displacement and momentum thickness coefficients can be calculated as

$$c_d = \int_0^1 u^*\, dy^* = \int_0^1 y^{*1/7}\, dy^* = \frac{7}{8} \tag{2.120}$$

$$c_m = \int_0^1 u^{*2}\, dy^* = \int_0^1 y^{*2/7}\, dy^* = \frac{7}{9} \tag{2.121}$$

Eq. (2.98) can be rewritten as

$$-\frac{dp}{dx} h - 0.0228\ \rho u_o^2 \left(\frac{\nu}{u_o h}\right)^{1/4} = \frac{d}{dx}\left(c_m \rho u_o^2 h\right) \tag{2.122}$$

Substitution of Eq. (2.105) to Eq. (2.122) yields

$$-\frac{dp}{dx} h = 0.0228\ \rho \left(\frac{vs}{c_d h}\right)^2 \left(\frac{vc_d}{vs}\right)^{1/4} + \frac{d}{dx}\left(c_m \rho \frac{v^2 s^2}{c_d^2 h}\right) \tag{2.123}$$

The ratio between the first and the second terms in the right side of Eq. (2.123) is

$$\frac{0.0228\,\rho\left(\frac{vs}{c_d h}\right)^2\left(\frac{vc_d}{vs}\right)^{1/4}}{\frac{d}{dx}\left(c_m\rho\frac{v^2s^2}{c_d^2 h}\right)} \sim \left(\frac{\nu}{v\Delta D}\right)^{1/4}\frac{\Delta D}{h} \sim \left(\frac{\mu}{\rho v h}\right)^{1/4}\left(\frac{\Delta D}{h}\right)^{3/4} \tag{2.124}$$

Since $\mu/\rho vh$ is of order of 1 and $\Delta D$ is of much larger order of magnitude than h, the second term is negligible compared with the first term. Thus, the molten layer thickness for turbulent flow can be estimated as

$$h \sim \left(\frac{0.0228\,\rho\Delta D}{\Delta p}\right)^{1/3}\left(\frac{v\Delta D}{c_d}\right)^{7/12} v^{1/12} \tag{2.125}$$

To determine the molten layer flow type, the Reynolds number should be calculated. The Reynolds number based on the groove depth is expressed as

$$Re_{\Delta D} = \frac{u_o \Delta D}{\nu} = \frac{\rho v(\Delta D)^2}{c_d \mu h} \tag{2.126}$$

Since aluminum oxide is used as a workpiece material, the viscosity of aluminum oxide molten material should be known. Although the exact viscosity value is not available, it can be estimated from the following formular derived from quantum physics [70]:

$$\mu = \left(\frac{N}{V}\right)^{2/3}(2\pi mkT)^{1/2}\frac{bRT}{\Delta E_{vap}} e^{\Delta E_{vap}/RT} = 0.009773 \text{ g cm/s} \tag{2.127}$$

where N: Avogadro number = $6.023 \times 10^{23}$ mole$^{-1}$

V: molar volume = $M/\rho = 26.97$ cm$^3$/mole

m: molecular weight = 101.94 g/mole

k: Boltzman's constant = $1.38 \times 10^{-23}$ J/K

T: temperature = 2072 + 273 = 2345 K

b: constant = 2

$\Delta$Evap: enthalpy of vaporization ~ 9.4 $RT_b$

$T_b$: boliling temperature = 2980 + 273 = 3253 K

n: number of atoms per molecule = 5

h: Planck's constant = 6.62 x $10^{-34}$

For the typical grooving condition (material = aluminum oxide, scanning velocity = 0.508 cm/s, and the groove depth = 0.5 cm), the Reynolds number is

$$Re_{\Delta D} = \frac{2.8(0.508)(0.5)^2}{(7/9)(0.009773)h} = \frac{46.78}{h} \tag{2.128}$$

Since the groove depth decreases with the increase in the scanning velocity and $v(\Delta D)^2$ is almost constant in a broad range of the scanning velocity near the grooving condition (Fig. 3.35), the Reynolds number does not vary significantly. To make the flow turbulent, the molten layer thickness should satisfy the following

$$\frac{46.78}{h} > 5 \times 10^4 \tag{2.129}$$

or

$$h < 9.36 \times 10^{-4} \text{ cm} = 0.053 \text{ d} \tag{2.130}$$

Eq. (2.130) means that if the molten layer thickness at the top of the cutting front is less than 5 per cent of the beam spot diameter, the molten material flow at the top becomes turbulent. For the most flow to be turbulent, the maximum molten layer thickness should be less than about 0.5 percent of the beam spot diameter. In this case, the molten layer effect on the groove depth becomes negligible, and the assumption that molten material is completely removed is reasonable. Thus, the molten layer analysis is meaningful only when the flow is laminar. If the molten layer thickness calculated under the assumption of laminar molten material flow satisfies Eq. (2.130), the molten layer can be ignored.

When an effective gas jet is used, the resulting molten layer thickness is very small. Since the molten layer volume is much less than the heat affected zone volume, the amount of heat to superheat the molten layer beyond the melting point is negligible compared with

the conduction or the melting heat However, as long as the molten layer thickness is comparable to the beam diameter and the groove width, the molten layer increases the melting front width, and the increase in the melting front width requires large amount of heat to melt material per unit depth. Since the melting heat is proportional to the cross-sectional area of the melting front, a thick molten layer reduces the aspect ratio of the melting front cross-section, and thus reduces the groove depth.

According to Eqs. (2.115), the molten layer thickness can be calculated with known groove depth. Since the groove depth is initially unknown, a repetition method is needed to determine the groove depth and the molten layer thickness. The groove depth can be determined as the follows:

1. Calculate the groove depth based on the assumption that molten material is totally ejected.
2. Calculate the maximum pressure difference at the cutting front, and the thickness of a molten layer from the pressure distribution.
3. Calculate the groove depth with the effective laser spot diameter, which is adjusted according to the molten layer thickness such as

$$d_{effective} = d + 2h_{avg} \tag{2.131}$$

where $d_{effective}$ is the effective beam spot diameter, and $h_{avg}$ is the average molten layer thickness. In this step, a grooving with a finite molten layer thickness is substituted by a grooving with a larger beam diameter and no molten layer. Since the superheat is much less than the major heat components such as conduction heat, melting heat, etc., the resulting error is expected to be negligible.

The three steps are repeated until the calculated groove depth converges. The groove depths predicted by the three theoretical solutions will be compared with experimental results in Chap 3.

## 2.4 Three-Dimensional Machining

The three-dimensional laser machining consists of two single beam grooving. The material removal rate in the three-dimensional machining can be determined simply from the

groove depth predicted by the single beam grooving solutions. However, since there are two beams (heat sources) and the heat affected zone induced by one beam is affected by the other heat source, the groove depth of the two beam machining might be different from that of single beam solutions. A finite difference method is employed to determine the groove depth and the material removal rate.

Numerical formulation for the three-dimensional machining is basically the same as that of the single beam grooving except the boundary conditions. Since the two beams are of the same intensity distribution, there is a symmetric plane, which can be a boundary. Heat affected zones (and thus grooves) are not symmetric with respect to the z-axis. Therefore, the numerical analysis domain should cover a groove (Fig. 2.13) instead of a half groove in the single beam grooving. The boundary conditions for the three-dimensional machining analysis are

$$x = x_{max}: \qquad \partial T/\partial x = 0 \tag{2.132}$$

$$x = x_{min}\ ;\ y = y_{min}\ ;\ y = y_{max}: \qquad T = T_o \tag{2.133}$$

$$z = z_{min}: \qquad \partial T/\partial y = \partial T/\partial z \tag{2.134}$$

At the top surface ($z = z_{max}$), the energy balance (Eq. (2.74)) is the boundary condition. The initial values for G and H at the bottom plane can be determined from the boundary condition (2.134):

$$\frac{\partial T}{\partial z} = \frac{1}{k}(GT + H) \tag{2.135}$$

$$\frac{\partial T}{\partial y} = \frac{T - T_{-1}}{\Delta y} \tag{2.136}$$

$$GT + H = \frac{k}{\Delta y}(T - T_{-1}) \tag{2.137}$$

where $T_{-1}$ is the temperature at the node next to the node on the symmetric boundary in the y direction. Since Eq. (2.137) holds for arbitrary T, the initial values for G and H can be determined as:

$$G(z_{min}) = \frac{k}{\Delta y} \tag{2.138}$$

$$H(z_{min}) = -\frac{kT_{-1}}{\Delta y} \tag{2.139}$$

The temperature, $T_{-1}$, is replaced by the temperature at the node which has the same y coordinate on the symmetric boundary as the node for the temperature $T_{-1}$. In order to determine the groove depth for the given laser power and scanning velocity, the laser center is started from a small y value, and moved in the positive y direction until the groove bottom surface meets the symmetry boundary plane.

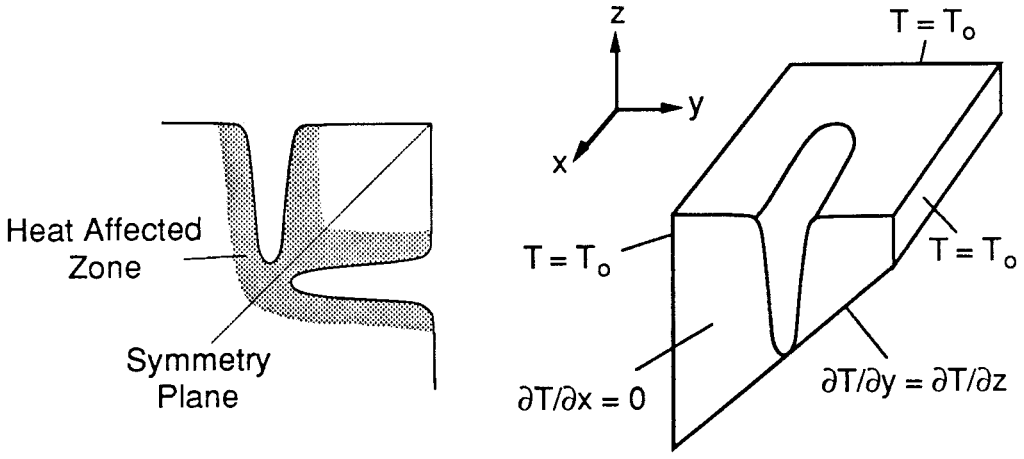



Fig. 2.13: Numerical Domain and Boundaries for Three-Dimensional Machining.

# CHAP 3. EXPERIMENTAL RESULTS AND DISCUSSION

A gas jet plays an important role in laser grooving. In this chapter, the gas jet effects are investigated experimentally for pressure distribution on a cutting front and the groove depth. Two types of experiments are performed: gas jet test, and grooving test. The gas jet test is performed with an off-axial jet alone, and the grooving test is performed with a coaxial jet, an off-axial jet, and a laser beam. Grooving tests are more expensive and time-consuming than gas jet tests. Also, grooving involves gas jet flow as well as heat transfer, which makes it difficult to interpret grooving test resluts. Thus, it is useful to perform gas jet tests before grooving tests to understand gas jet flow aspects without heat transfer aspects.

## 3.1 Gas Jet Test

The objectives of gas jet tests are to understand the effects of jet parameters on the pressure distribution at the cutting front. Three gas jet tests were performed: *flat-workpiece test, grooved-workpiece test, and real-size-groove test.* The flat-workpiece test was performed to understand the characteristics of normal impingement of a supersonic gas jet; the grooved-workpiece test was to find the general trends of various parametric effects; the real-size-groove test was to understand the gas jet interaction with a groove similar to one made in grooving.

An experimental apparatus was constructed, as shown in Fig. 3.1. Reservoir pressure (chamber pressure) was regulated by a valve connecting a compressed air line and the gas chamber. A micrometer adjustment stage was used to provide accurate longitudinal translation. The support structure provided three degrees of freedom for nozzle/workpiece distance, jet attack angle, and jet targeting distance. In the real-size-groove test, jet targeting distance was defined as the distance from the top surface to the intersection point between an assumed laser beam center line (coaxial jet center line) and the off-axial jet center line, as shown in Fig. 3.1. However, in the rest of the gas jet tests, jet targeting distance was defined as the distance from the axis of the assumed laser beam to the point on the groove surface where a jet center is aimed, since most experiments in those tests were performed with 90° of jet attack angle, and the off-axial jet is parallel to the assumed laser beam. Pressure transducers were used to measure the static pressures in the reservoir and at the workpiece.

Nozzles of various exit diameters were machined to have a convergent shape (averaging 15° taper angle), as shown in Fig. 3.2. A supersonic jet from a simply convergent nozzle is called under-expanded jet. In the flat-workpiece and the grooved-workpiece test, nozzles with circular exit shape were used. In the real-size-groove test, a nozzle with oval exit shape was used. The oval shape nozzle delivers more air flow rate and momentum to the cutting front.

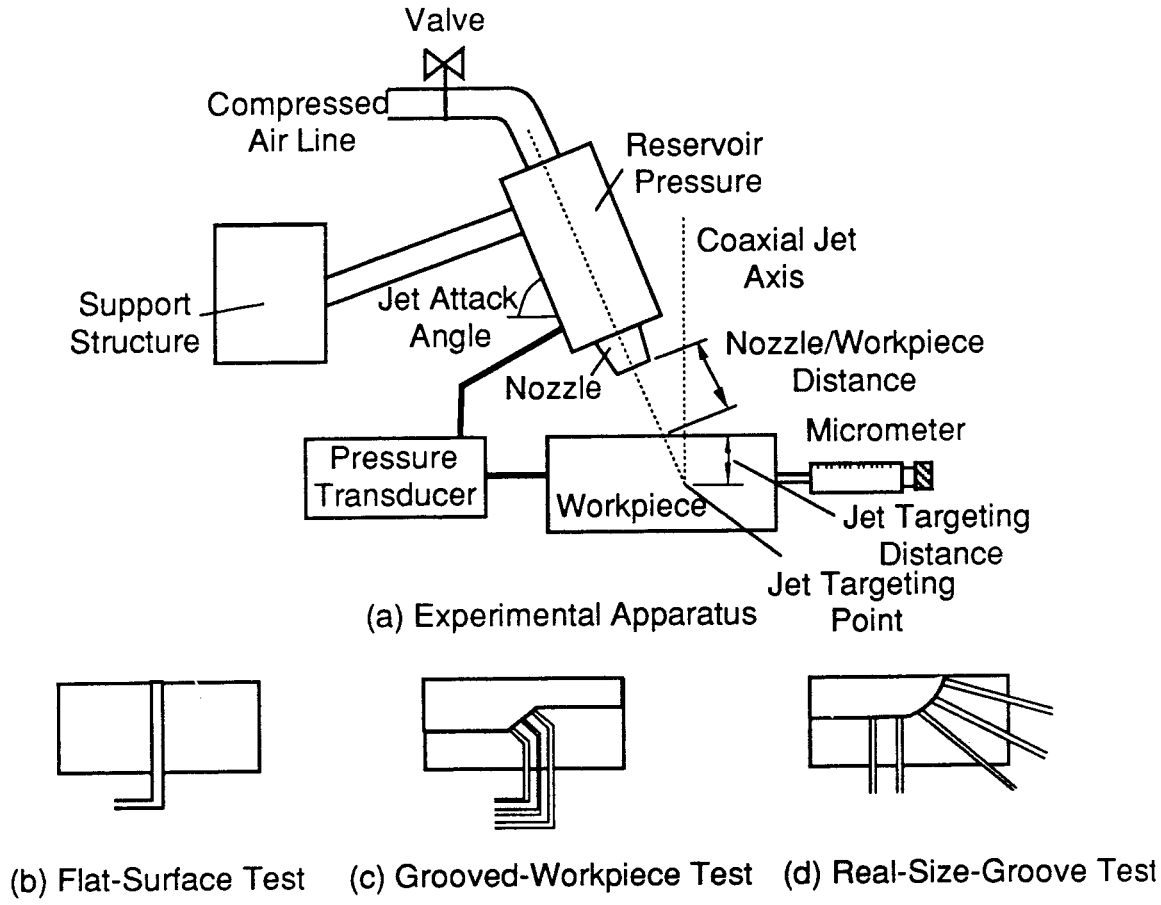



Fig. 3.1: Experimental Apparatus and Wokpieces for Gas Jet Tests.

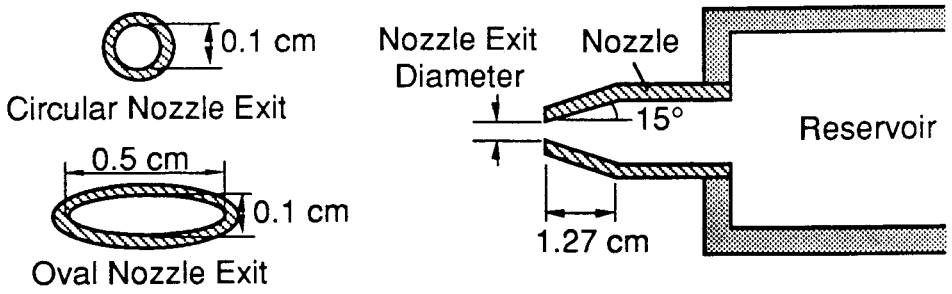



Fig. 3.2: Convergent Nozzles Used in Gas Jet Tests.

### 3.1.1 Flat-workpiece test

Supersonic jets have higher stagnation pressures than subsonic jets, and are more effective for molten material ejection in grooving. They have complicated shocks, which are difficult to understand. In order to find the role of a supersonic jet in grooving, its characteristics should be understood. As a first step, experiments were performed on normal impingement of a supersonic jet to a flat surface. Reservoir pressure and nozzle/workpiece distance were varied. A circular nozzle of exit diameter of 0.10 cm was used. During each trial, reservoir pressure was increased, and the pressures at the flat-workpiece were measured. The experiment was repeated for different values of nozzle/workpiece distance in a range from 0.13 cm to 1.87 cm.

Fig. 3.3 shows a plot of workpiece pressure vs. reservoir pressure for nozzle/workpiece distance variations. Workpiece pressure is defined as the pressure measured at the point on the workpiece surface where the jet center aims. Fig. 3.3 shows that the workpiece pressure is proportional to the reservoir pressure for reservoir pressures less than 1.8 bar. This is because the jet is subsonic in that pressure range. Since a jet diverges after the nozzle exit, the workpiece pressure for large nozzle/workpiece distances (e.g. 0.95 cm in Fig. 3.3) is very small compared with the reservoir pressure. For reservoir pressures higher than 2 bar, the workpiece pressure is not simply proportional to the reservoir pressure, unless nozzle/workpiece distance is large. The explanation for this behavior is that for high reservoir pressure the resulting jet becomes supersonic, and shocks occur in front of the workpiece, which make the jet flow complicated. The workpiece pressure is related to the jet stagnation pressure after a shock. Since the characteristics of supersonic jet interaction with a flat surface is important in understanding

of the gas jet flow in grooving, it is useful to review the related work before discussing further the phenomena shown in Fig. 3.3.

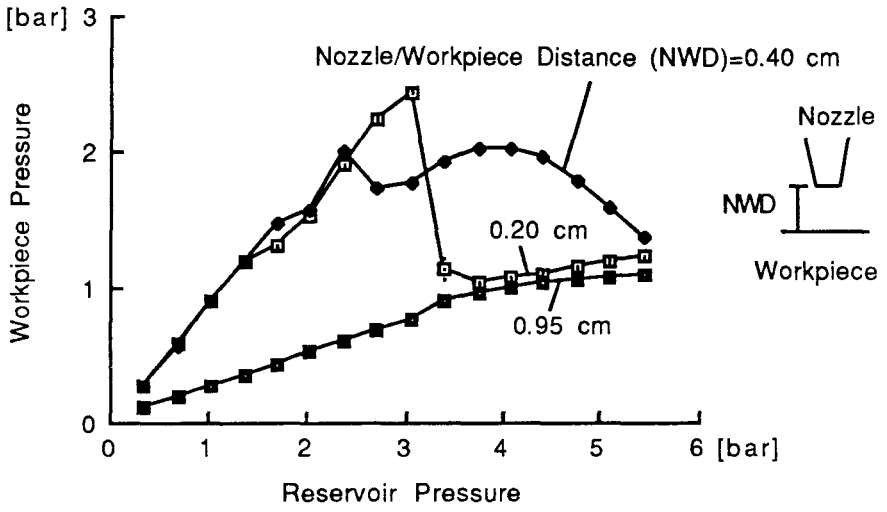



Fig. 3.3: Workpiece Pressure vs. Reservoir Pressure for Nozzle/Workpiece Distance Variations (nozzle exit diameter = 0.1 cm, and jet attack angle = 90°).

Two types of shocks can occur during the interaction of an under-expanded supersonic jet with a body: a surface shock and a Mach shock. A surface shock occurs in front of a body when a supersonic jet impinges a body. A Mach shock occurs in a free supersonic jet whose reservoir pressure is high enough (> 3.4 bar for an air jet), as shown in Fig. 3.4. When a Mach shock occurs, the jet has an oblique shock originating from the circumference of the Mach shock. Across a Mach shock the inner jet becomes subsonic, and across the oblique shock the outer jet remains supersonic. The stagnation pressure of the inner jet drops substantially. A slip stream separates the inner jet with the outer jet. The inner subsonic jet is accelerated by the outer jet, until it becomes supersonic again. The location of a Mach shock depends on the reservoir pressure of the jet and the nozzle configuration (nozzle diameter, nozzle type, etc.), while the location of a suface shock depends on the workpiece position and the upstream jet Mach number.

The supersonic cell dimension increases monotonically with the increase in the reservoir pressure. Fig. 3.5 shows cell length, distance to a Mach shock, and Mach shock diameter with respect to reservoir pressure [64]. As shown in Fig. 3.6, if a workpiece is located too close not to allow a Mach shock to occur (approximately within the jet cell

length), only a surface shock occurs in front of the workpiece. Since in a supersonic flow the upstream condition does not change, the upstream supersonic cell structure remains the same as that of a free jet until a shock. If a workpiece is located farther than the location of a Mach shock and shorter than a distance where the inner jet becomes supersonic again (approximately between 1 and 5/3 of the jet cell length), only a Mach shock occurs. In that case, the location of the Mach shock does not change with respect to the workpiece position. The workpiece pressure drops due to a Mach shock, and is recovered as the nozzle/workpiece distance increases. If a workpiece is located farther than a distance where the inner jet becomes supersonic (greater than 5/3 of the jet cell length), a surface shock as well as a Mach shock occurs between the nozzle and the workpiece. As nozzle/workpiece distance increases further, the workpiece pressure behavior explained above is repeated with a slight decay.

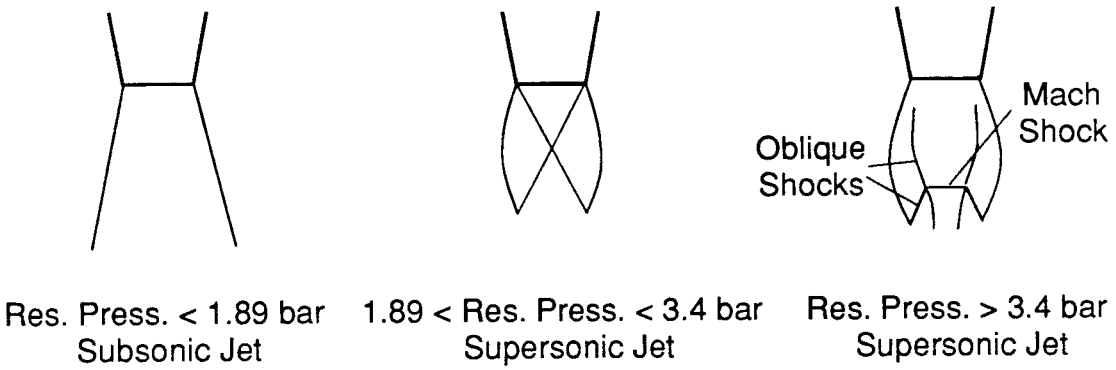



Fig. 3.4: Reservoir Pressure and Jet Structure.

For small nozzle/workpiece distances (0.2 cm), when the reservoir pressure is greater than 1.89 bar, a surface shock occurs between nozzle exit and the workpiece. Since the shock occurs at relatively low Mach number, the downstream stagnation pressure does not decrease significantly. When the reservoir pressure becomes greater than 3.4 bar, a Mach shock occurs. Since a Mach shock occurs at about the maximum Mach number, the stagnation pressure drops substantially across the Mach shock, and the resulting downstream jet stagnation pressure and the workpiece pressure become small. In the plot of workpiece pressure for nozzle/workpiece distance of 0.2 cm, the Mach shock effect on the workpiece pressure is clearly shown. For 3.4 bar of reservoir pressure, the ratio between the ambient pressure and the reservoir pressure is

$$p_a/p_r = 1/(3.4+1) \tag{3.1}$$

where $p_a$ is the ambient pressure, $p_r$ is the reservoir pressure. The minimum pressure, p*, in the jet satisfies the following equation:

$$p^* p_r = p_a^2 \tag{3.2}$$

Thus, the ratio between p* and $p_r$ can be determined as

$$p^*/p_r = (p_a/p_r)^2 = (4.4)^{-2} = 0.0517 \tag{3.3}$$

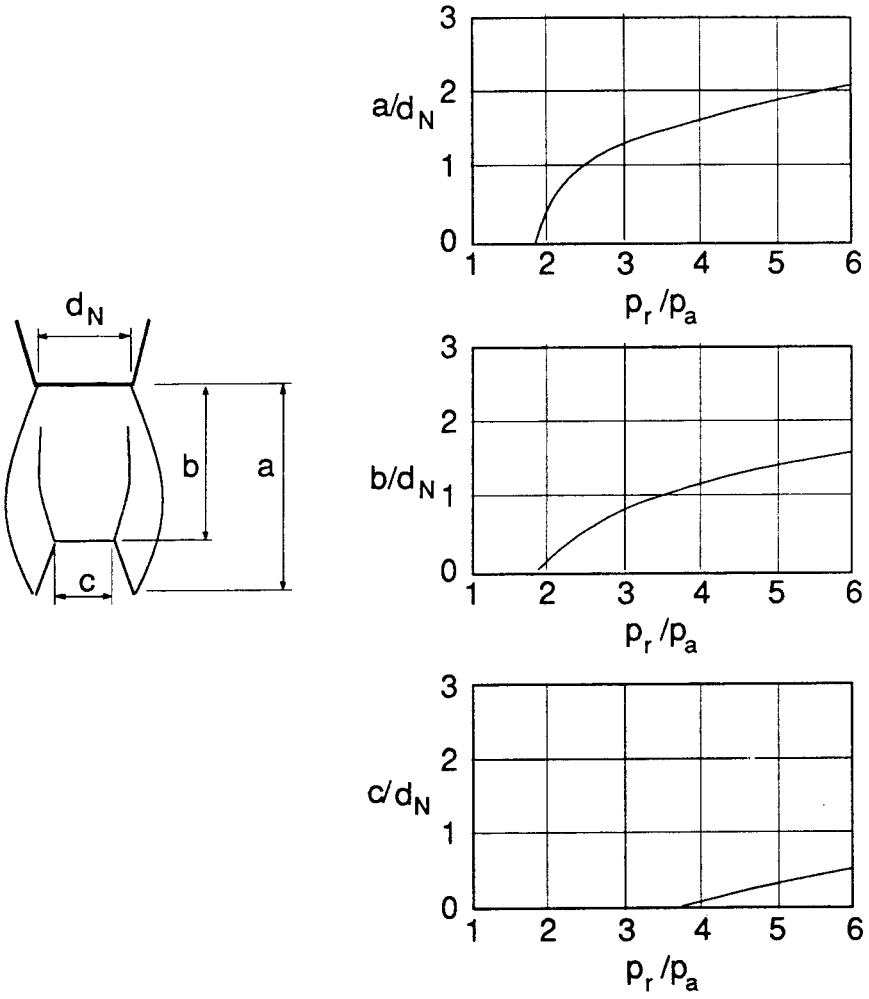



Fig. 3.5: Under-Expanded Supersonic Cell Dimension vs. Reservoir Pressure [64].

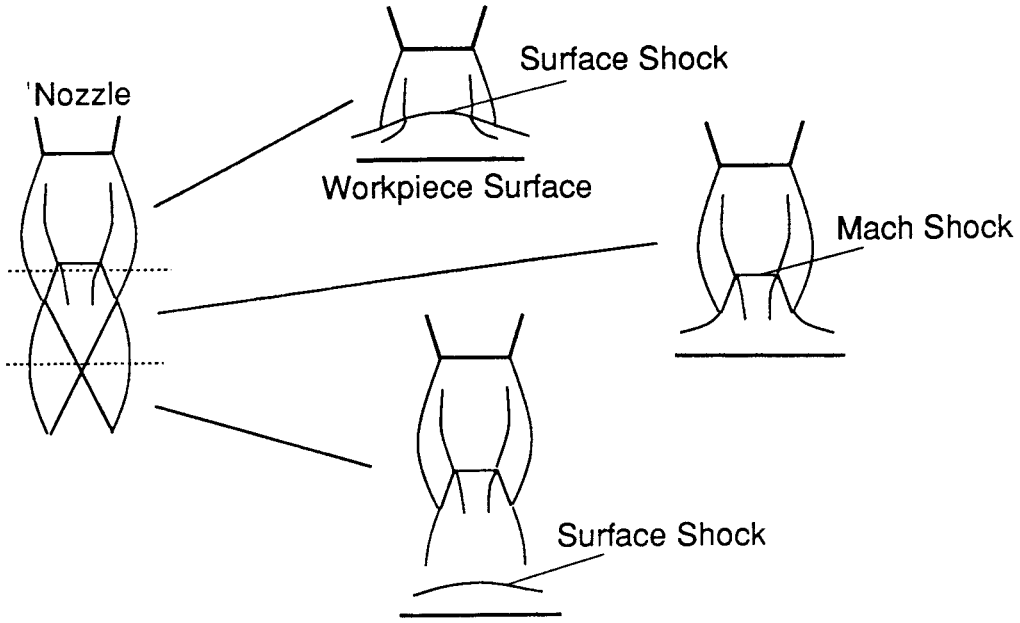



Fig. 3.6: Shock Types Depending on Nozzle/Workpiece Distance.

The maximum Mach number for the given reservoir pressure, which occurs at the minimum pressure p*, is 2.58. The ratio between the jet stagnation pressures at the downstream and the upstream is 0.468, and the downstream jet stagnation pressure is 1.09 bar. Fig. 3.3 shows that the workpiece pressure is close to 1.09 bar for 0.2 cm of nozzle/workpiece distance and 3.4 bar of reservoir pressure. As the reservoir pressure increases, the maximum Mach number increases. Higher reservoir pressure tends to increase the workpiece pressure, while higher Mach number reduces the workpiece pressure due to a Mach shock. Thus, for reservoir pressures higher than 3.4 bar the workpiece pressure remains almost the same. For 5.5 bar of reservoir pressure and 0.2 cm of nozzle/workpiece pressure, the downstream jet stagnation pressure is 0.95 bar based on the above calculation. Fig. 3.3 shows that the workpiece pressure is slightly greater than the downstream stagnation pressure of a free supersonic jet. This is because for high reservoir pressures the cell length increases and a surface shock occurs instead of a Mach shock. Since the surface shock occurs at a small Mach number and the stagnation pressure drop becomes small, the downstream stagnation pressure is larger than that of a free jet.

Fig. 3.3 shows a complicated variation of the workpiece pressure for 0.4 cm of nozzle/workpiece distance. Since the supersonic structure is very complicated, only a qualitative expalnation is possible. Since the jet cell length is less than twice the nozzle exit

diameter (0.1 cm) within the test reservoir pressure range, for 0.4 cm of nozzle/workpiece distance more than two cells exists between the nozzle exit and the workpiece. Near the workpiece the jet is supersonic whether or not a Mach shock occurs. Thus, a Mach shock which might occur at a high reservoir pressure does not influence the workpiece pressure, but a surface shock determines the workpiece pressure. If a surface shock occurs at a high (low) Mach number, the resulting workpiece pressure becomes small (large).

For large nozzle/workpiece distances (0.95 cm), the jet is dissipated and becomes subsonic near the workpiece surface. Due to jet dissipation and divergence, the jet has a small jet stagnation pressure. Since the flow near the workpiece is subsonic, the workpiece pressure increases monotonically with the increase in the reservoir pressure.

Fig. 3.7 shows the pressure distribution at the surface in the radial direction from the center. For high reservoir pressure, the maximum workpiece pressure occurs at a certain distance from the center. This is because a Mach shock occurs in front of the workpiece. Across a Mach shock the jet stagnation pressure drops substantially in the inner jet, while across the oblique shock the stagnation pressure does not decrease significantly. Thus, the pressure is higher at the periphery than at the center. A small pressure at the center implies that a separated region is formed around the center, and the jet flows toward the center from the periphery (Fig. 3.8). In actual laser grooving applications, this can lead to accumulation of molten material at the cutting front.

The flat-workpiece test results can apply to through-cutting, where a high stagnation pressure is desirable for molten material ejection. The best condition for the through-cutting process, yielding high workpiece pressure, can be determined from the flat-workpiece test results.

### 3.1.2 Grooved-workpiece test

In the previous jet test, the characteristics of supersonic interaction with a flat surface was investigated. With understanding of a supersonic jet impingement on a flat surface, a test of a supersonic jet interaction with grooves was conducted to find the general trends of parametric effects on the pressure distribution at the cutting front.

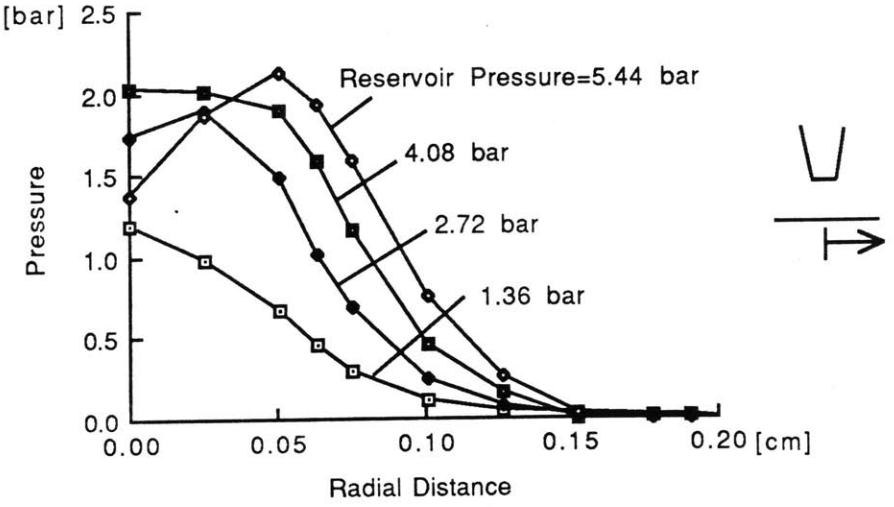
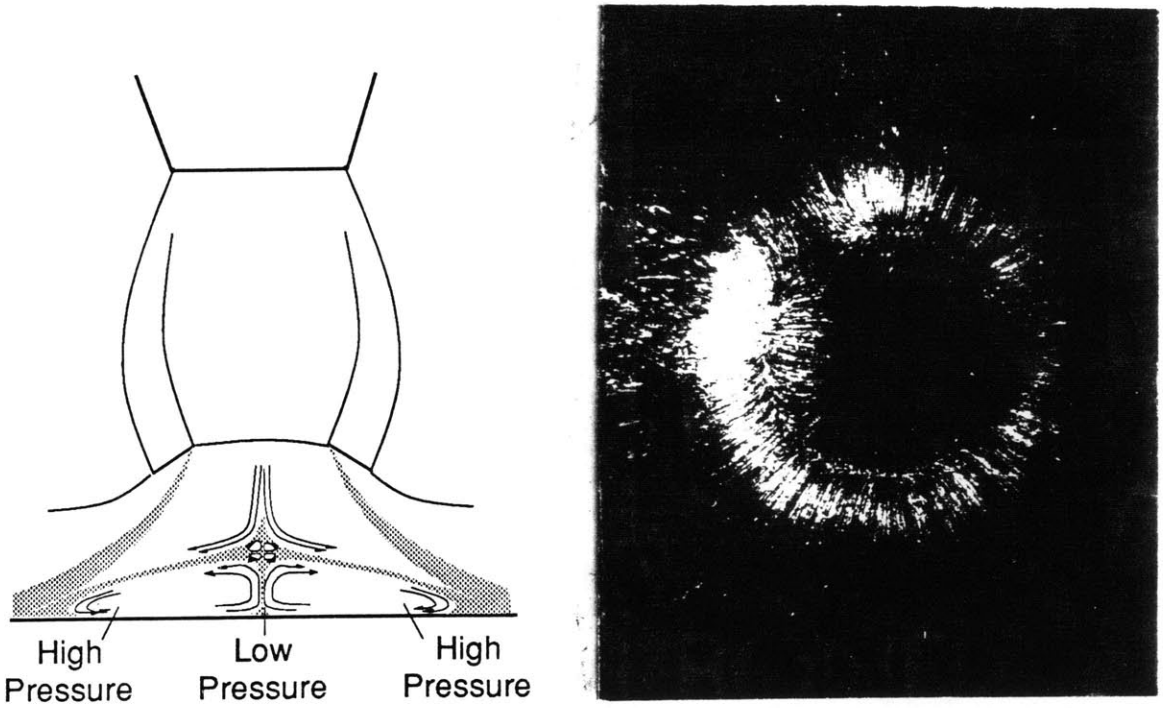



Fig. 3.4: Workpiece Pressure as a Function of Radial Distance from the Jet Targeting Point (nozzle/workpiece distance = 0.4 cm, nozzle exit diameter = 0.1 cm , and jet attack angle = 90°).




(a) Flow Separation

(b) Grease Streak Photo [57] (Top View)

Fig. 3.8: Jet Separation and Surface Flow Visualization.

A groove was formed by using two parallel plates attached to a contoured bottom plate. The groove was machined to have a straight cutting front. This shape is not the same as that of the actual grooving process. The reasons for using that groove shape are:

1. the parameters related to groove geometry can be easily changed, and
2. all the jet interaction phenomena happening during grooving can be observed by using the shape.

Groove depth was changed by placing plates of various heights on the contoured groove bottom surface. Groove width was adjusted by changing the distance between the two plates. Interchangeable bottom surfaces were machined with different cutting front angles. Three holes (center, top, and bottom) at the cutting front were drilled to measure the static pressures (Fig. 3.1 (c)).

The ranges of parameters in this test are shown in Table 3.1. For each trial, one parameter was varied while the other parameters were set at the fixed values. The reservoir pressure was ramped and the resulting static pressures in the reservoir and at the three points of the cutting front were measured. Results were plotted in the form of pressure difference at the cutting front vs. reservoir pressure for the variations in each parameter.

| Parameter | Range |
|---|---|
| ***Groove Parameter*** | |
| groove depth | 0.74 - 2.00 cm |
| groove width | 0.05 - 0.13 cm |
| groove angle | 30 - 90° |
| ***Jet Parameter*** | |
| nozzle/workpiece distance | 0.12 ~ 0.55 cm |
| jet targeting distance | - 0.15 to 0.15 cm from the center of the cutting front |
| jet attack angle | 30° - 90° |
| nozzle exit diameter | 0.05 - 0.20 cm |

Table 3.1: Parameter Ranges for Groove Tests.

Of special interest are the differences between the pressure at the center point and the pressures at the top ($\Delta P_t = P_c - P_t$) and bottom point ($\Delta P_b = P_c - P_b$) of the cutting front, because they determine the magnitude and direction of the driving force for material expulsion from the groove.

Fig. 3.9 shows the effect of reservoir pressure on pressure differences $\Delta P_t$ and $\Delta P_b$ for two groove depths (0.74 and 2.00 cm). While a peak for both pressure differences can be observed for a groove depth of 0.74 cm, the pressure differences remain practically unchanged with increase in reservoir pressure for a depth of 2.00 cm. In Fig. 3.10, the effects of reservoir pressure on the pressure differences for two groove widths are shown. For a groove width of 0.13 cm, $\Delta P_t$ increases with increasing reservoir pressure. For a groove width of 0.05 cm, $\Delta P_t$ decreases first and then levels off. An explanation for the negative $\Delta P_t$ can be that a shock occurring in front of the groove reduces the pressure at the center of the cutting front, but does not significantly affect the pressures at the periphery, as explained before. Fig. 3.10 also shows that the pressure difference is smaller for small groove width than for large groove width. This is because of the boundary layer effect, which reduces pressure differences at the cutting front through the jet dissipation with the groove walls.

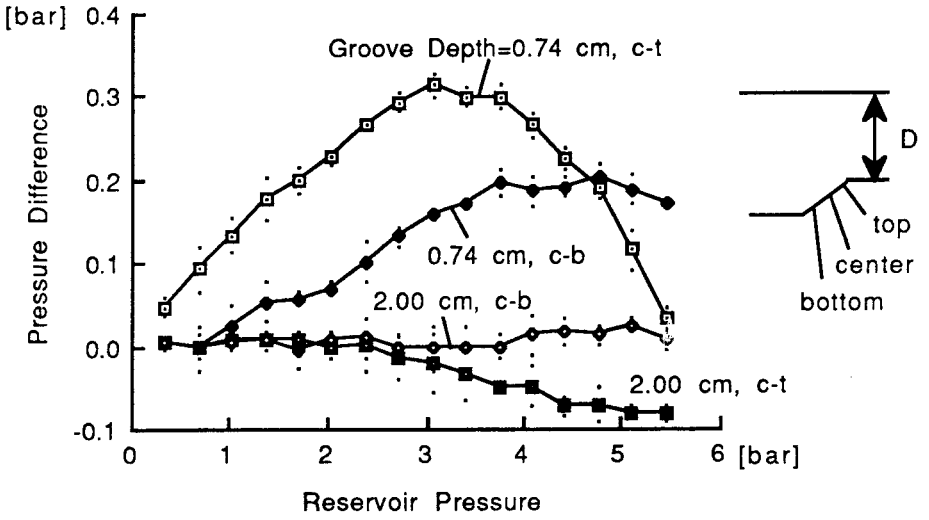



Fig. 3.9: Pressure Difference vs. Reservoir Pressure for Groove Depth Variations (other conditions: 0.4cm nozzle/workpiece distance, 0.1cm nozzle exit diameter, 90° jet attack angle, 0.076cm groove width, 45° cutting front angle).

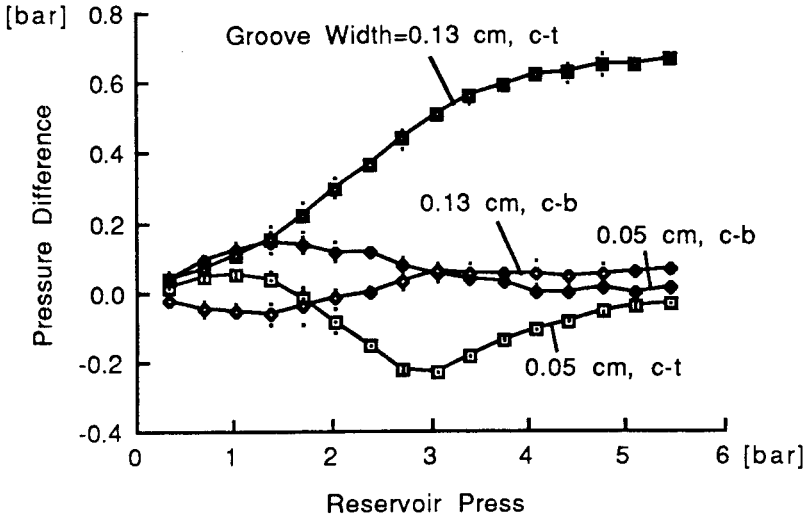



Fig. 3.10: Pressure Difference vs. Reservoir Pressure for Groove Width Variations (other conditions: 0.4cm nozzle/workpiece distance, 0.1cm nozzle exit diameter, 90° jet attack angle, 0.74cm groove depth, 45° cutting front angle)

In Fig. 3.11, the plot of pressure differences vs. reservoir pressure for changes in cutting front angle is shown. Larger pressure differences could be observed for a cutting front angle approaching the direction normal to the jet attack direction.

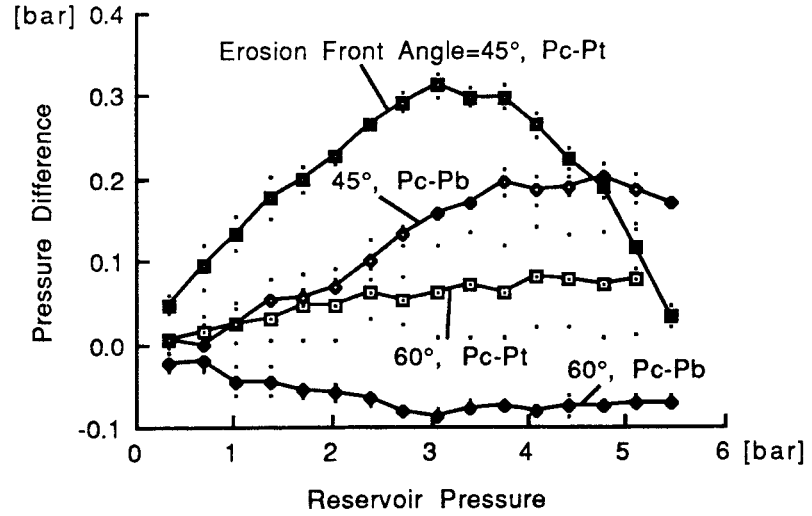



Fig. 3.11: Pressure Difference vs. Reservoir Pressure for Groove Angle Variations (other conditions: 0.4cm nozzle/workpiece distance, 0.1cm nozzle exit diameter, 90° jet attack angle, 0.74cm

groove depth, 0.076cm groove width)

Fig. 3.12 shows the plot of pressure differences vs. reservoir pressure for nozzle/workpiece distance variations. Depending on nozzle/workpiece distance, there are two directions of molten material flow. For small nozzle/workpiece distances, strong shocks reduce the pressure at the center less than that at the bottom point, causing molten material flow from the bottom to top of the cutting front. For large nozzle/workpiece distances, shocks are weak and do not significantly affect the center pressure. In this case, the molten material flows from center to bottom and top. The critical nozzle/workpiece distance determining the flow direction of the molten material is approximately 0.2 cm.

The relationship between pressure differences and reservoir pressure for jet targeting distance variation is shown in Fig. 3.13. For non-zero jet targeting distances, pressure differences increase or decrease monotonically. For small negative jet targeting distances (in the direction of x' in Fig. 3.13), both $\Delta P_t$ and $\Delta P_b$ are negative, causing molten material to flow towards the center of the cutting front. This flow is related to a formation of a separation region. In laser grooving, this condition may cause accumulation of molten material at the center of the cutting front. For larger shifts off-center, $\Delta P_t$ is positive and increases monotonically with shifting distance, while $\Delta P_b$ is negative and has a peak value.

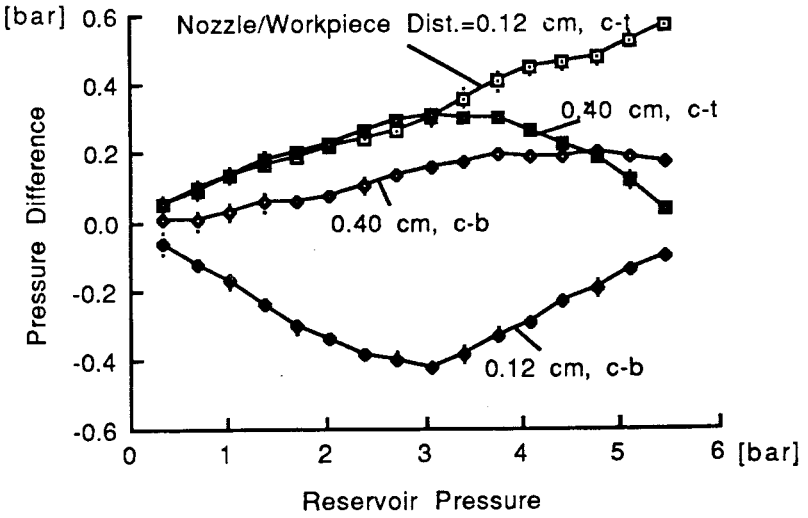



Fig. 3.12: Pressure Difference vs.Reservoir Pressure for Nozzle/workpiece Distance Variations.(other conditions: 0.1cm nozzle exit diameter, 90° jet attack angle, 0.74cm groove depth, 0.076cm groove width, 45°

cutting front angle)

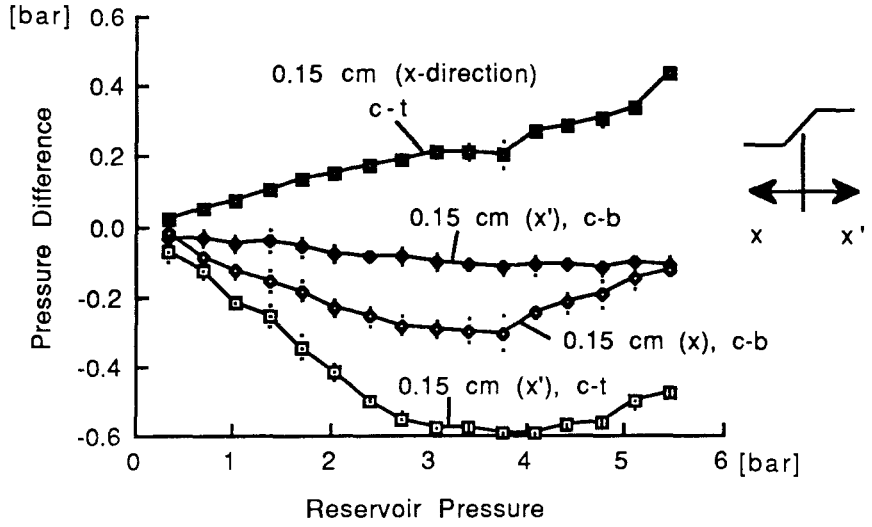



Fig. 3.13: Pressure Difference vs. Reservoir Pressure for Jet Targeting Distance Variations.(other conditions: 0.4cm nozzle/workpiece distance, 0.1cm nozzle exit diameter, 90° jet attack angle, 0.74cm groove depth, 0.076cm groove width, 45° cutting front angle)

In Fig. 3.14, the relationship between pressure differences and reservoir pressure for jet attack angle variation is shown. The pressure differences with respect to reservoir pressure have similar shapes for different jet attack angle. The decrease in the pressure difference at high reservoir pressures is due to the fact that for high reservoir pressures the jet diameter becomes large and makes the pressure distribution along the cutting front uniform. For 30° and 90° of jet attack angles, the pressure differences were found to be significantly smaller than those for 45° or 60°.

The effect of reservoir pressure on the pressure differences for variations in nozzle exit diameter is shown in Fig. 3.15. Nozzles with a small exit diameter (e.g. 0.05 cm) cannot cause a significant pressure change in the cutting front. For 0.10 cm of nozzle exit diameter, a nozzle/workpiece distance of 0.40 cm is too large to cause a large change in pressure difference, but for a nozzle diameter of 0.20 cm, the same nozzle/workpiece distance is within the range in which a large change in pressure difference can occur.

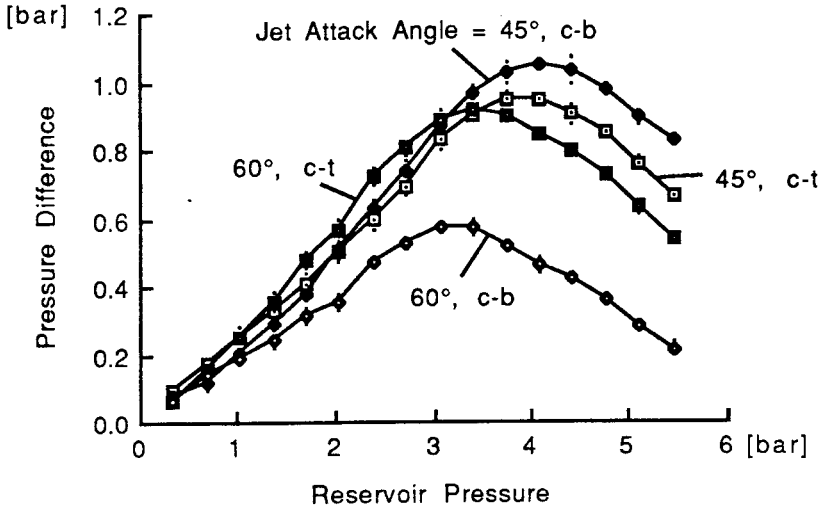



Fig. 3.14: Pressure Difference vs. Reservoir Pressure for Jet Attack Angle Variations.(other conditions: 0.4cm nozzle/workpiece distance, 0.1cm nozzle exit diameter, 0.74cm groove depth, 0.076cm groove width, 45° cutting front angle)

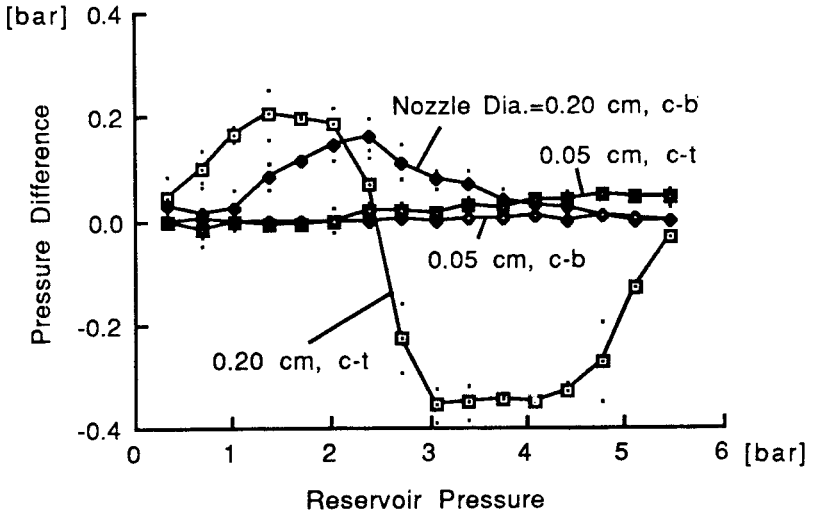



Fig. 3.15: Pressure Difference vs. Reservoir Pressure for Nozzle Exit Diameter Variation.(other conditions: 0.4cm nozzle/workpiece distance, 90° jet attack angle, 0.74cm groove depth, 0.076cm groove width, 45° cutting front angle)

From the gas jet experiments, several phenomena were observed for different jet parameters and groove geometry conditions. These phenomena include supersonic shocks, jet flow direction, and jet flow separation.

An under-expanded supersonic free jet forms a series of supersonic cells [58]. If a workpiece is close to the nozzle exit or reservoir pressure is relatively high, a shock occurs in front of the workpiece surface [52,53,59-61]. Across the shock, the jet stagnation pressure drops, resulting in a low pressure on the jet targeting point. Jet dissipation also influences the pressure distribution through the jet/wall contact length. In a deep and thin groove, jet dissipation reduces the jet stagnation pressure and uniformizes the pressure distribution at the cutting front.

From the grooved-workpiece test, there are four possible flow directions for jet flow at the cutting front: from center to top and bottom, toward the center, from bottom to top, and from top to bottom (Fig. 3.16). The ideal jet flow direction is from bottom to top of the cutting front. That jet flow direction yields cleaner cuts by driving molten material in the same direction. Mach shocks cause molten material to flow toward the center. A jet flows from top to bottom under the condition of a large nozzle diameter with high reservoir pressure in deep or thin grooves. A jet flows from bottom to top under the condition of large groove widths (or small groove depths) with low reservoir pressure and positive jet targeting distance (in the direction to the established groove).

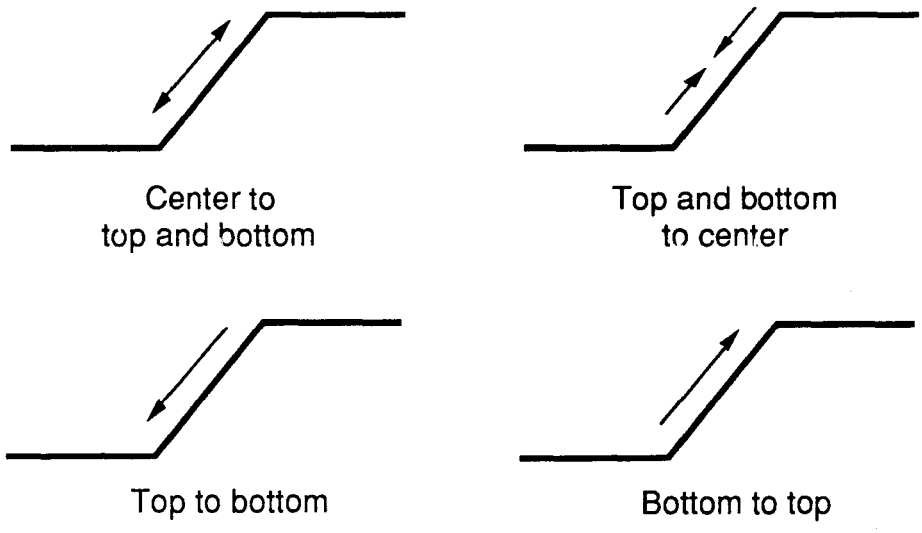



Fig. 3.16: Flow Directions of Molten Material.

The top-and-bottom-to-center direction might result in accumulation of molten material in the middle of the cutting front in an actual grooving and is unfavorable for molten material ejection. This flow behavior results from higher pressure at the periphery due to the presence of a Mach shock disc, and can lead to formation of a separated region of jet flow (FIg. 3.17).

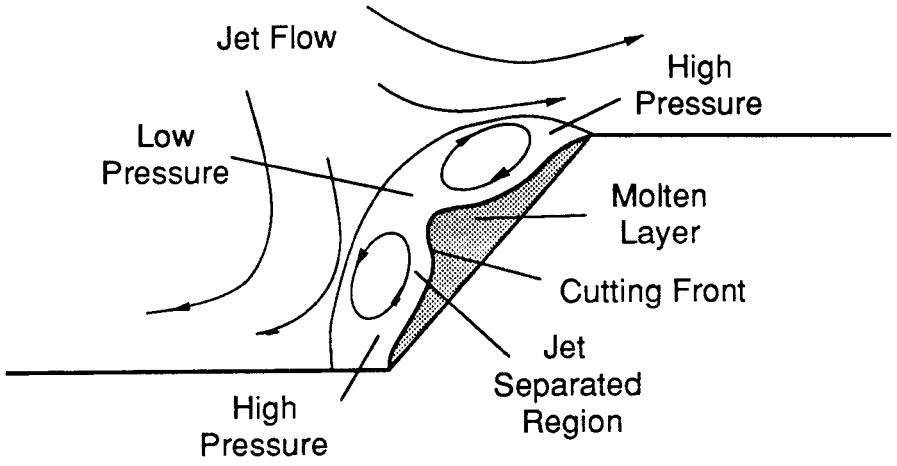



Fig. 3.17: Jet Flow Separation.

The parameter conditions, which yield high pressure differences at the cutting front, are shown in Table 3.2. Since the groove geometry depends on the process variables such as laser power, scanning velocity, number of passes, etc., optimal groove geometry is not meaningful in general. However, it might be useful to decide the process variables (e.g., number of passes) when a certain material removal is given as a task in three-dimensional laser machining. Small groove depth (less than 0.74 cm), medium groove width (greater than 0.08 cm and less than 0.13 cm), and small groove angle (less than 30°) were shown to be good for maximum molten material removal. In general, high pressure differences at the cutting front result from the jet attack angle perpendicular to the cutting front, small nozzle/workpiece distance, and positive jet targeting distance.

| Parameter | Value |
|---|---|
| ***Groove parameter*** | |
| Groove depth | <0.74 cm |
| Groove width | >0.08 cm and <0.13 cm |
| Groove angle | <30° |
| ***Jet parameter*** | |

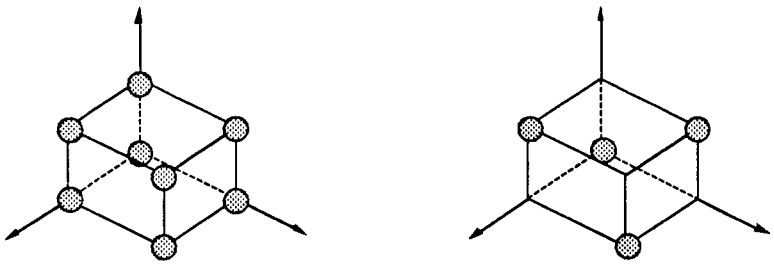
| | |
|---|---|
| Nozzle/workpiece distance | <0.12 cm |
| Jet targeting distance | >0.15 cm |
| Jet attack angle | perpendicular to the cutting front |
| Nozzle diameter | >0.10 cm and <0.20 cm |

Table 3.2: Conditions for High Pressure Differences in Grooved-Surface Test.
(a circular convergent nozzle of 0.1 cm diameter is used)

### 3.1.3 Real-Size-Groove Test

In the previous gas jet tests, the general trends of the gas jet parametric effects on pressure difference were investigated. Since the gas jet effects on groove depth is of interest, it is useful to conduct gas jet experiments under a situation similar to an actual grooving. In this test, a groove, which has the same dimension and shape as a groove made during laser grooving, was machined on a workpiece. A nozzle with oval exit shape was used (Fig. 3.2), since the oval nozzle delivers more momentum to the cutting front in grooving. Since jet attack angle was found to be unimportant in the preliminary grooving test (section 3.2), it was fixed at 60° in this test, and only three jet parameters were varied: nozzle/workpiece distance, jet targeting distance, and reservoir pressure. The ranges of the parameters were selected to cover the ranges found to be important in the preliminary jet tests.

When an output is affected by a number of parameters, performing experiments with one parameter varied and others fixed was thought to be an accurate way to find the effects of the parameters. However, this is accurate only for the fixed values of other parameters: for example, an optimal condition found that way is not necessarily optimal, if other parameters vary. In multi-parameter problems, an effective method is the factorial experimental design, which is to select experimental conditions by varying all the parameters simultaneously [71, 72]. As shown in Fig. 3.18 (a), the effects of 3 parameters can be determined from 8 experiments at the points (experimental conditions) arranged in a cubic configuration. The concept can be also applied to a case where 4 points are selected in the cube as shown in Fig. 3.18 (b). This is called fractional factorial design [73, 74]. The factorial design is a technique to extract maximum information from small number of experiments without loss of accuracy.



(a) Complete Factorial Design (b) Fractional Factorial Design

Fig. 3.18: Complete and Fractional Factorial Designs

According to the completer factorial design, 100 conditions were selected for the three parameters with four or five levels (Table 3.3). As shown in Fig. 3.3 (c), pressures were measured at the five points on the cutting front. The difference between the pressures at the top and bottom of the cutting front was determined, which is the driving force for molten material ejection.

| Parameter | Levels | | | | |
|---|---|---|---|---|---|
| | 1 | 2 | 3 | 4 | 5 |
| Jet Targeting Distance (cm) | 1.732 | 1.292 | 0.852 | 0.412 | -0.028 |
| Nozzle/Workpiece Distance (cm) | 0.236 | 0.318 | 0.396 | 0.475 | 0.544 |
| Reservoir Pressure (bar) | 1.361 | 2.721 | 4.082 | 5.102 | |

Table 3.3: Parameter Levels for Real-Size-Groove Test.

Fig. 3.19 shows the main effect of jet targeting distance on the pressure difference. The main effect of one parameter excludes the effects of other parameter values. The squares and the points in the figure represent the mean pressure differences (which were obtained by averaging all the values with the same parameter value regardless of other parameter values), and mean value ± one standard deviation, respectively. This figure shows that 1.3 cm of jet targeting distance produces the maximum pressure difference. Although experiments were not performed for jet targeting distances greater than 1.7 cm, beyond that value the resulting jet aiming point on the groove bottom surface is so far away from the cutting front that the jet is not effective and the pressure difference at the cutting front becomes small.

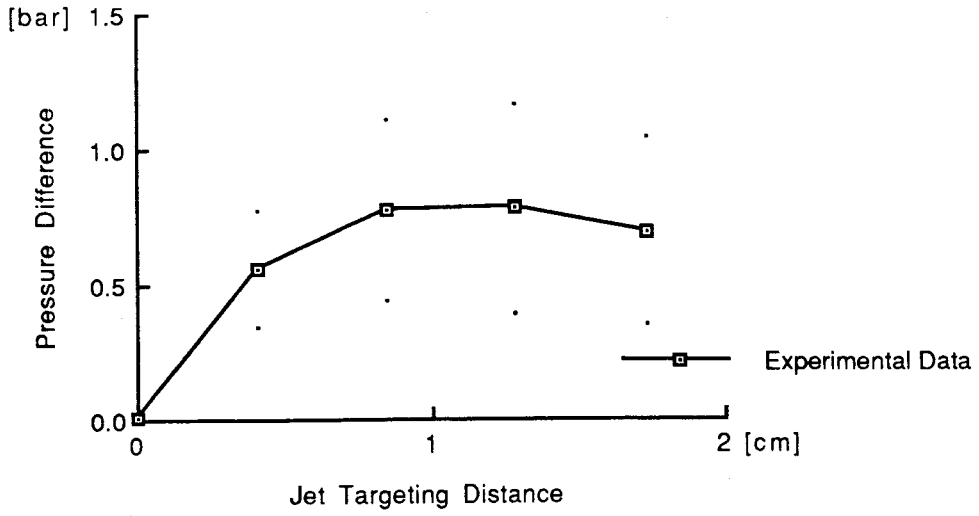



Fig. 3.19: Main Effect of Jet Targeting Distance on Pressure Difference

Fig. 3.20 shows that the relation between nozzle/workpiece distance and pressure difference is periodic. This is because the supersonic cells are repeated, and location of shocks, which depends on the nozzle/workpiece distance, is also repeated. Unlike the flat-workpiece test, the real-size-groove test result do not show significant drops in pressure. Due to the jet dissipation with the groove walls, the jet is mixed, and sharp drops which might occur at the groove inlet are smoothed out inside the groove.

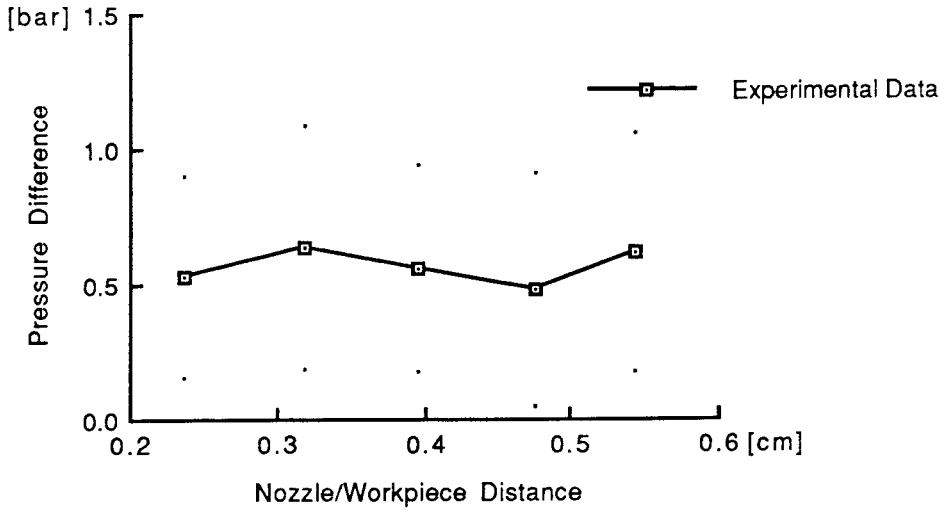



Fig. 3.20: Main Effect of Nozzle/Workpiece Distance on Pressure Difference

Fig. 3.21 shows the main effect of reservoir pressure on the pressure difference. It is shown that in general high reservoir pressures yield high pressure differences at the cutting front and large deviations.

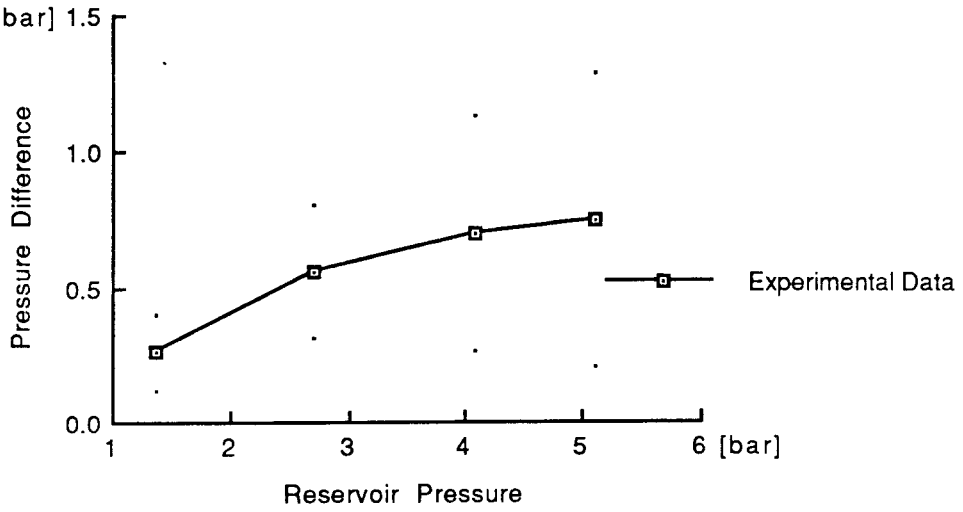



Fig. 3.21: Main Effect of Reservoir Pressure on Pressure Difference

## 3.2 Grooving Test

In order to determine the effects of gas jet parameters on the groove depth, find the best jet conditions for grooving, and check the validity of the theoretical analysis, a grooving experimental program was established. The experimental program consists of three tests to find:

1. the qualitative effect of an off-axial jet on groove formation: comparison between grooves made with and without an off-axial gas jet
2. the effects of gas jet parameters on groove depth: the best jet conditions producing the maximum groove depth for fixed process condition, and
3. application of the best jet condition to grooving for various process conditions.

The grooving tests were performed on aluminum oxide workpieces, the properties of which are shown in Table 3.4.

| *Thermal Property* | | |
|---|---|---|
| absorptivity | 0.2 - 0.6 | - |
| conductivity | 0.033 | W/cm°C |
| density | 2.8 | $g/cm^3$ |
| latent heat of fusion | 4150 | J/g |
| melting temperature | 2072 | ℃ |
| specific heat | 0.85 | J/g°C |
| *Mechanical Property* | | |
| hardness | 25000 | MPa |
| tensile strength | 480 | MPa |
| Young's modulus | 92 | MPa |

Table 3.4: Physical Properties of Aluminum Oxide ($Al_2O_3$).

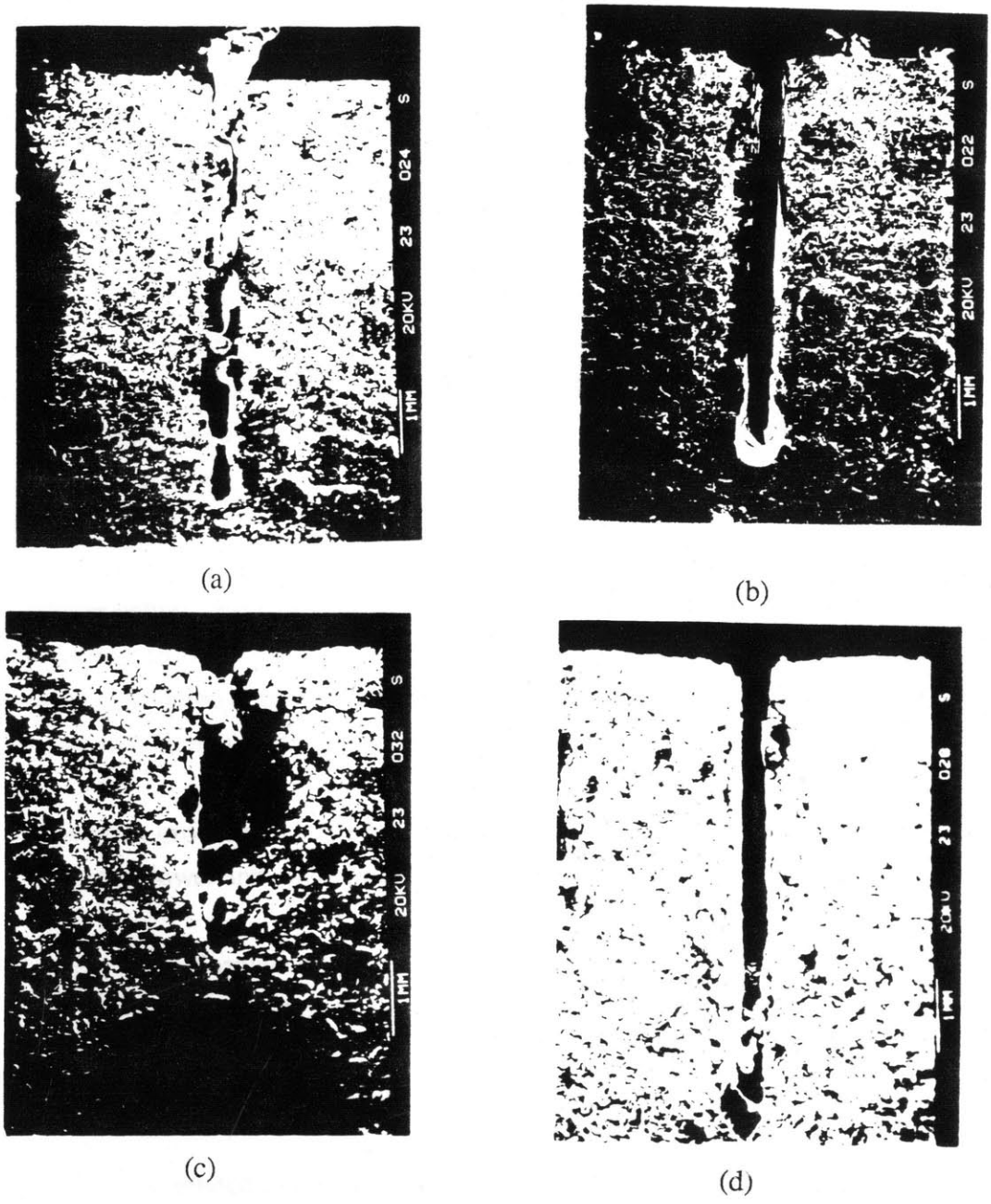
### 3.2.1 Effects of an off-axial gas jet

In order to find the effects of an off-axial gas jet on groove formation, grooving experiments were conducted with and without an off-axial gas jet. Fig. 3.22 shows four grooves formed by the laser beam with various jet conditions. The grooves (a) and (b) were made under the process condition of power = 500 W, scanning velocity =0.508 cm/s, and number of passes = 1, and the grooves (c) and (d) were made under the condition of power = 500 W, scanning velocity = 1.02 cm/s, and number of passes = 2. The grooves (a) and (c) were made without an off-axial gas jet, while the grooves (b) and (d) were made with an off-axial gas jet. The figure shows that the groove with an effective off-axial jet can be 30 per cent deeper than that without an off-axial jet in double-pass grooving and the grooves without an off-axial jet are filled with resolidified material. A coaxial jet blows molten material downward in the direction of the established groove, where the molten material is resolidified. In multiple-pass grooving, the resolidified material, which has to be melted prior to further ablation of the groove bottom material in the next pass, causes a significant reduction in the groove depth as well as deterioration of the surface quality. An off-axial jet trailing the laser beam ejects molten material in the same direction as the laser beam moves. As shown in Fig. 3.22, if an off-axial jet is effectively utilized, the resulting groove can be deep and clean.

To find the effects of an off-axial jet on molten material removal in multiple-pass grooving, grooving experiments were performed on 1.5 cm thick aluminum oxide workpieces with and without an off-axial jet. The laser power was 500 W, and the scanning velocity was 0.508 cm/s. In the experiment without using an off-axial gas jet, the reservoir pressure of a coaxial gas jet was set at 3.4 bar, which is close to the maximum possible reservoir pressure for the coaxial jet (without damaging the focussing lens). In the experiment with an off-axial gas jet, the reservoir pressures of a coaxial and an off-axial gas jet were set at 0.34 and 4.76 bar, respectively. With an off-axial gas jet, ten passes of laser scanning cut through the workpiece, while without an off-axial gas jet thirty passes did not cut through the workpiece. During the experiment without an off-axial gas jet, it was found that almost no molten material was removed after 15 passes. This means that in a deep groove, the coaxial gas jet did not remove molten material out of the groove and in the following passes a laser beam energy was totally used to remelt the resolidified material. When a thick workpiece is to be cut through by many laser beam passes, material removal direction is important and a use of an off-axial gas jet is necessary. Note that ten passes of laser scanning was needed, although the thickness of the workpiece was only 3 times the depth of a groove made by one pass. This is because in a deep groove the laser beam is defocused and the gas jet, due to jet dissipation at a large contact length with the groove walls, produce a uniform pressure distribution along the cutting front which is ineffective in ejecting molten material.

### 3.2.2 Effects of gas jet parameters on groove depth

In the previous section, it was found that grooves can be made deep and clean by a use of off-axial gas jets. It is of interest to find a dominat parameter affecting groove formation most and the jet condition producing deep grooves and the corresponding groove depths. There are so many jet parameters that the number of experiments would be enormous to find even the first-order parametric effects. Thus, the number of jet parameters should be reduced by screening out parameters which are unimportant or whose effects are obvious.




(a) (b)

(c) (d)

Fig. 3.22: Cross-Sectional Groove Shapes for Various Jet Conditions
P = 500W, v = 0.508 cm/s, number of passes = 1: (a) 3 bar coaxial (b) 1.5 bar coaxial and 5 bar off-axial reservoir pressure
P = 500 W, v = 1.02 cm/s, number of passes = 2: (c) 3 bar coaxial (d) 1.5 bar coaxial and 5 bar off-axial reservoir pressure.

Nozzle exit shape, nozzle exit diameter, and nozzle type are not to be investigated. If a jet diameter is large compared with a groove width, only the middle part of the jet penetrates into the groove, and the jet diameter at the groove inlet in the longitudinal direction becomes important. For the same jet diameter, nozzles of oval shape need less flow rate than those of circular shape. Thus, nozzles of oval shape are more effective. Nozzle exit diameter is not critical as long as the jet diameter is large enough compared with the groove width. According to [64], a convergent-divergent nozzle has a bigger supersonic cell and a higher Mach number in the cell than a simply convergent nozzle. Since a bigger cell results in less flow rate and a higher Mach number causes a larger stagnation pressure drop, a convergent-divergent nozzle is , in general, less effective than a simply convergent nozzle.

If two parameters are coupled with each other, one parametric effect is dependent of other parameter values. For instance, an optimal value for one parameter varies, if other parameter varies. In order to avoid this aspect due to the coupled effects, two or three parameters are considered at one test. Three tests were performed to eliminate unimportant parameters and to determine a dominat parameter.

To perform grooving tests, experimental ranges for the jet parameters should be selected. The ideal lower and upper limits for the four gas jet parameters are

- Nozzle/workpiece distance: $0 - \infty$
- Jet targeting distance: $0 - \infty$
- Jet attack angle: $90° - 0°$
- Reservoir pressure: $0 - \infty$

The lower limits are related to the off-axial nozzle setting close to a coaxial nozzle and a workpiece. For example, the off-axial nozzle set according to the ideal lower limits is on the coaxial nozzle position. Since the off-axial nozzle should be placed without being conflicted with the coaxial nozzle, the actual lower limits are different from the ideal lower limits. Although the possible lower limits depend on other parameters, for the given nozzles (shown in Fig. 3.2) the lower limits are approximately 0.2 cm for nozzle/workpiece distance, 0.2 cm for jet targeting distance, and 60° for jet attack angle. Since the whole ranges for those parameters cannot be covered, the upper limits should be selected to cover the major variations. The upper limits are selected from the gas jet test results.

When the test ranges for parameters are chosen, the number of levels for each parameter needs to be selected. In the 2 factorial design, two levels are used to find first order parametric effects (increase or decrease). In the Taguchi method, 3 levels are selected to find an optimal condition. Three levels might be good enough to find gradual parametric effects. Since supersonic jet interaction involves such phenomena as sudden drops, four or five levels seem proper to find the parametric effects

**Test I**

In the test I, three gas jet parameters were considered: nozzle/workpiece distance, jet targeting distance, and jet attack angle. Jet targeting distance was measured from the top surface to the intersecting point between the coaxial jet and off-axial jet center lines. Nozzle/workpiece distance was between 0.1 and 0.4 cm, and jet targeting distance was between 0.35 and 1.65 cm. Jet attack angle were 45° and 60°, since 60° is almost the largest possible jet attack angle without causing confliction between an off-axial nozzle and a coaxial nozzle. Small jet attack angles cause uniform pressure distributions on the cutting front due to jet dissipation through long contact lengths between the jet and the groove walls, and cannot produce deep grooves. For the three parameters, sixteen experimental conditions were selected.

The experimental setup is shown in Fig. 3.23. A $CO_2$ laser with the laser power of 500 W was used in the CW mode and the laser spot diameter was 0.0178 cm. The scanning velocity was fixed at 0.774 cm/s. The number of passes was two. A coaxial jet reservoir pressure was 2.5 bar to protect the lenses. An off-axial jet reservoir pressure was 4.76 bar. A circular convergent nozzle tapering at a 15° angle of 0.1 cm diameter was used. Aluminum oxide cylindrical workpieces of diameter 6.67 cm were used. Experiments were repeated over each condition.

The jet parameter values and the corresponding groove depths are listed in Table 3.5. This table shows that the groove depth changes up to ± 25 per cent, depending on the jet parameters.

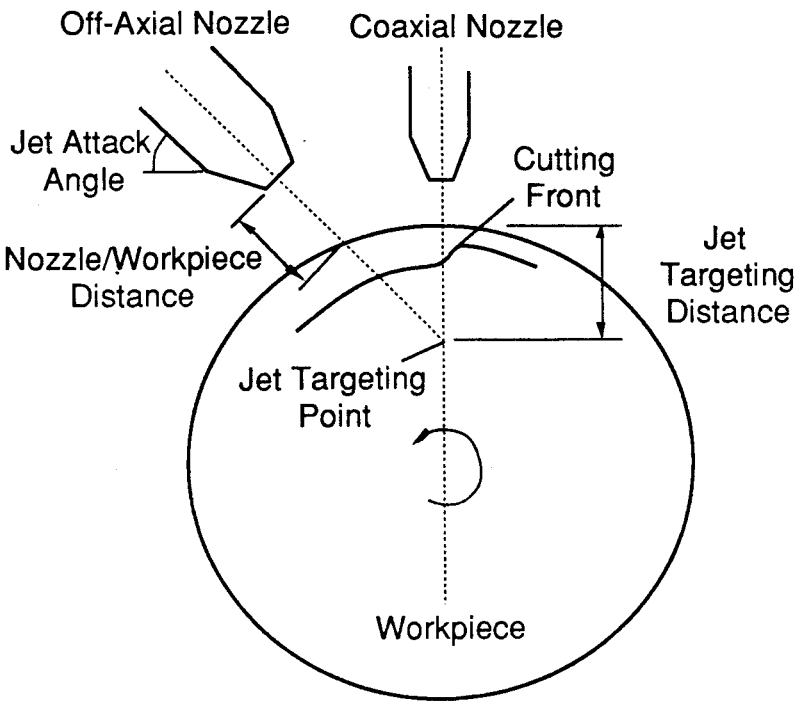



Fig. 3.23: Experimental Setup (Test I).

| Experiment No. | Nozzle/W Distance cm | Jet Targeting Distance cm | Jet Attack Angle (°) | Groove Depth cm |
|---|---|---|---|---|
| 1 | 0.1 | 0.78 | 60 | 0.3701 |
| 2 | 0.2 | 0.35 | 60 | 0.3548 |
| 3 | 0.2 | 0.60 | 45 | 0.3513 |
| 4 | 0.1 | 0.35 | 45 | 0.3132 |
| 5 | 0.3 | 1.65 | 60 | 0.3396 |
| 6 | 0.4 | 1.22 | 60 | 0.3843 |
| 7 | 0.4 | 1.10 | 45 | 0.3424 |
| 8 | 0.3 | 0.85 | 45 | 0.3208 |
| 9 | 0.1 | 1.65 | 60 | 0.3820 |
| 10 | 0.2 | 1.22 | 60 | 0.3348 |
| 11 | 0.2 | 1.10 | 45 | 0.2964 |
| 12 | 0.1 | 0.85 | 45 | 0.3797 |
| 13 | 0.3 | 0.78 | 60 | 0.2506 |
| 14 | 0.4 | 0.35 | 60 | 0.3145 |
| 15 | 0.4 | 0.65 | 45 | 0.3416 |
| 16 | 0.3 | 0.35 | 45 | 0.3439 |

Table 3.5: Jet Conditions and Corresponding Groove Depths.

Fig. 3.24 shows 4 grooves formed under the same power (500 W), and scanning velocity (0.774 cm/s) with different gas jet parameters. Groove (a) is clean and deep, while groove (b) is clogged and shallow. Compared with groove (d), groove (c) is deeper but has worse surface quality. Groove depths depends on the pressure gradient along the erosion front, while surface quality depends on the material removal (upward material removal produces clean grooves).

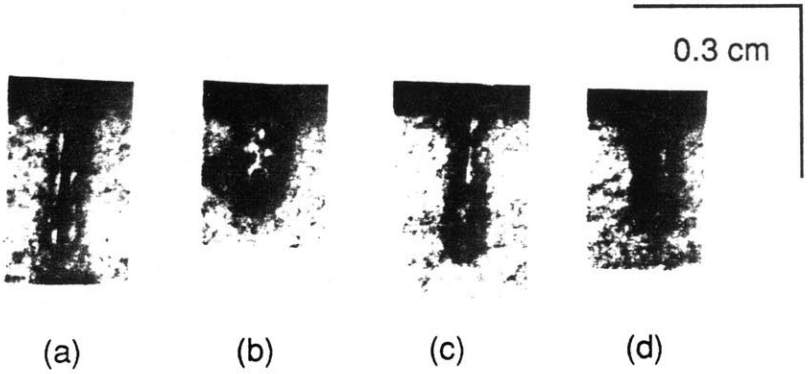



Fig. 3.24: Grooves Formed under the Process Condition: Laser Power = 500 W, Scanning Velocity = 0.508 cm/s, and Number of Passes = 2.

| | NWD (cm) | JAA(°) | JTD (cm) |
|---|---|---|---|
| (a) | 0.4 | 60 | 1.22 |
| (b) | 0.3 | 45 | 0.85 |
| (c) | 0.1 | 60 | 0.78 |
| (d) | 0.2 | 60 | 1.22 |

Fig. 3.25 shows the main effect of nozzle/workpiece distance on the groove depth. The experimental points were obtained by averaging the groove depths corresponding to the same nozzle/workpiece distance regardless of other parameters. The average value variation represents the effect of nozzle/workpiece distance, and the standard deviation variation represents other parametric effects. Fig. 3.25 shows that small nozzle/workpiece distance (0.1 cm) produces deep grooves while 0.3 cm of nozzle/workpiece distance produces shallow grooves. 0.3 cm of nozzle/workpiece distance might result in high stagnation pressure drop.

The main effect of jet targeting distance is shown in Fig. 3.26. This figure shows that in general large jet targeting distances produce deep grooves. For small jet targeting distances, material removal direction is not upward. The material, which is resolidified on

the groove wall due to an adverse material removal direction, requires additional laser energy in the next beam pass.

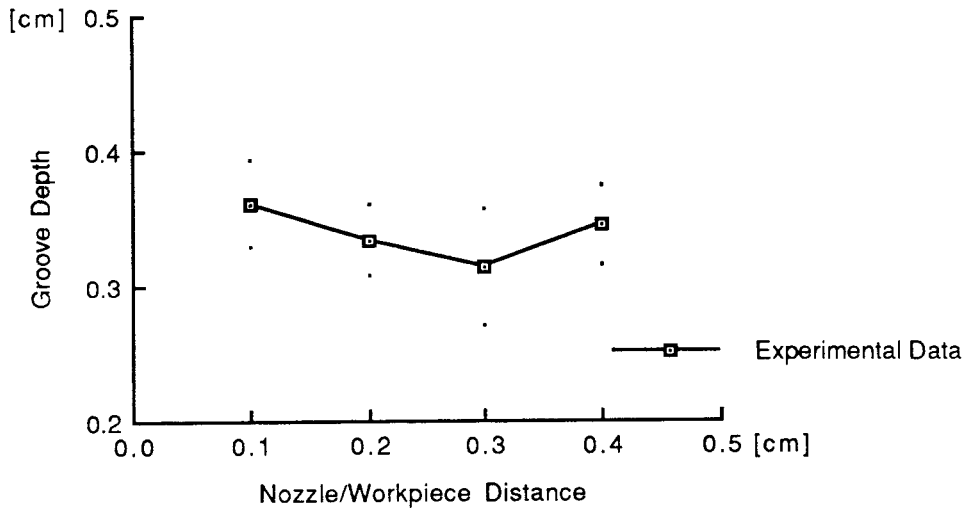



Fig. 3.25: Main Effect of Nozzle/Workpiece Distance on Groove Depth.

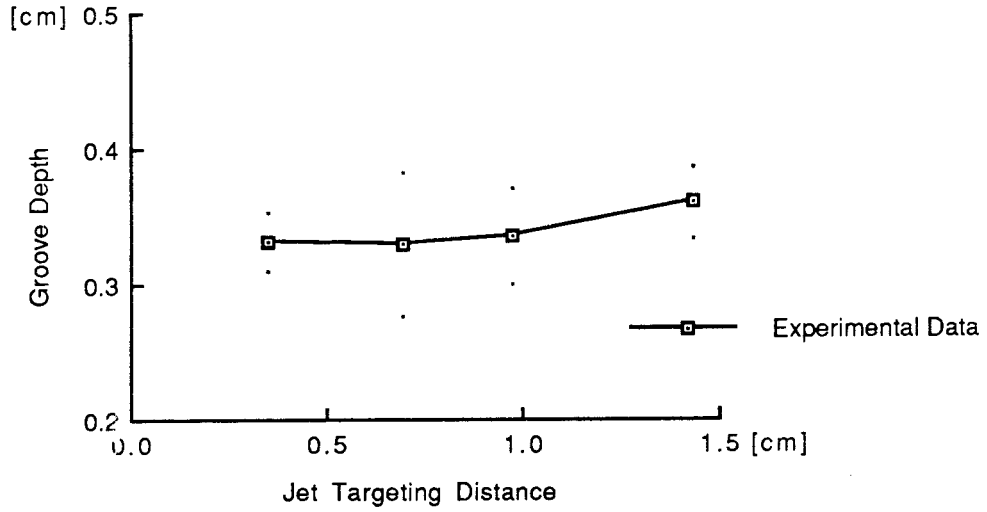



Fig. 3.26: Main Effect of Jet Targeting Distance on Groove Depth.

Fig. 3.27 shows the main effect of jet attack angle. The average groove depths do not show a significant difference in the test range. This means that within the test range jet attack angle is not important. Also, Fig. 3.27 shows that 60° of jet attack angle has a slightly larger average value and a larger standard deviation than 45°. That is, 60° can produce deeper grooves with proper values for other parameters than 45°. Jet attack angles

close to 90° cause bad molten material removal direction, and jet attack angles close to 0° cannot eject molten material, because the nozzle is too far away from the cutting front. Thus, some angle between 0 and 90° can produce the maximum groove depth. Since 60° is the largest possible jet attack angle and for 45° of jet attack angle groove depth is smaller than that for 60°, a jet attack angle between 60 and 90° would produce the deepest groove, and the groove depth would be reduced with decrease in jet attack angle from the optimal jet attack angle. For the following tests, jet attack angle will be fixed at 60°.

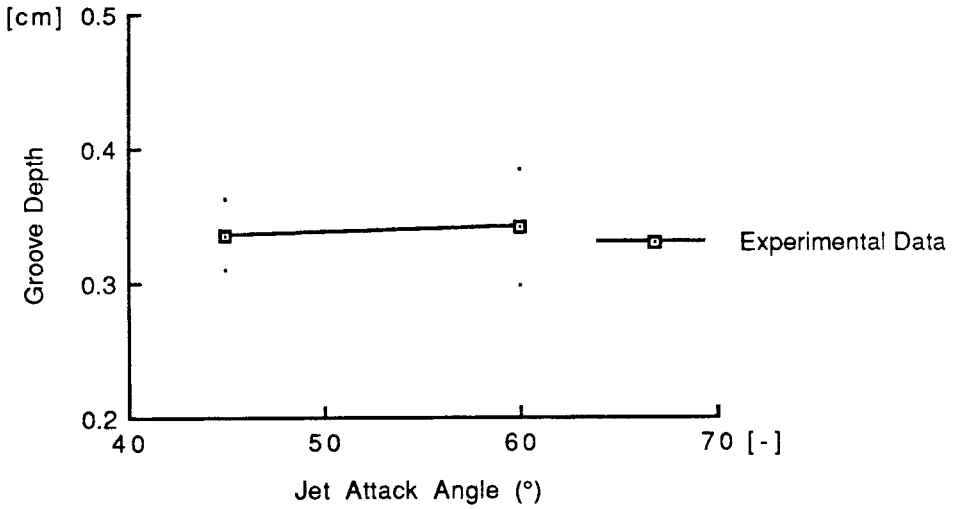



Fig. 3.27: Main Effect of Jet Attack Angle on Groove Depth.

## Test II

In this test, three jet parameters were considered: nozzle/workpiece distance, jet targeting distance, and reservoir pressure. Instead of a circular off-axial nozzle used in the Test I, a nozzle of 0.1 x 0.5 cm oval shape was used. Due to the large air mass flow through the oval shape nozzle, the grooves were relatively deeper than those in the previous grooving test. The laser power was 500 W, the scanning velocity was 0.508 cm/s, and the jet attack angle was 60°. The number of passes was one. Aluminum oxide plates of 1.5 cm thickness were used as workpieces. Fig. 3.28 shows the test setup.

Fig. 3.29 and 3.30 show the main effects of nozzle/workpiece distance and jet targeting distance on the groove depth, respectively. When a supersonic jet interacts with a grooved surface, a shock occurs around the groove. Nozzle/workpiece distance determines the shock location and the stagnation pressure drop in the supersonic cell. Jet targeting

distance plays a role of placing the jet on the groove bottom surface. In order to produce deep grooves, the portion of the jet which has the largest stagnation pressure should interact with the bottom of the cutting front. One parameter cannot determine the pressure distribution exclusively. Thus, the two parameters are coupled to each other.

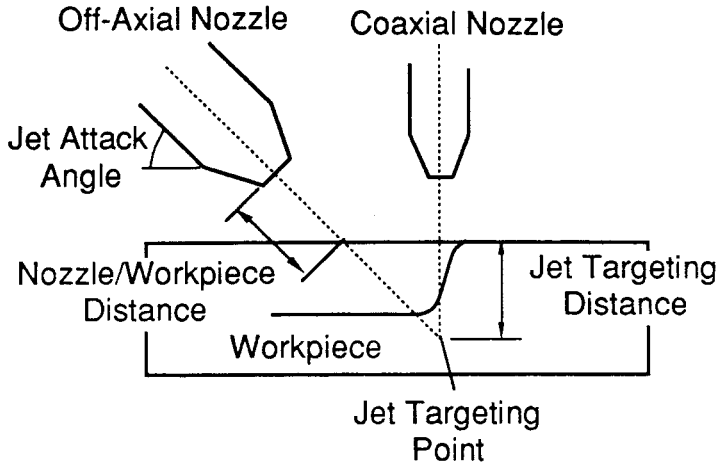



Fig. 3.28: Grooving Test Setup for Test II and III.

Fig. 3.31 shows the main effect of reservoir pressure. Among the three parameters, reservoir pressure shows the largest main effect on the groove depth. Fig. 3.31 also shows that 4.08 bar is the best condition for reservoir pressure. In the next test, the reservoir pressure will be fixed at 4.08 bar.

In order to control the groove depth in the laser grooving process or the material removal rate in the three-dimensional machining, one gas jet parameter should be selected as a control parameter [75]. The control parameter should have a large main effect, a small sensitivity to the variations of other parameters, a linear dependency over a broad range, and be less coupled with other parameters. In this thesis, the first two were used as the criteria for determining a control parameter (Fig. 3.32). Main effect is the effect of the parameter variation on the average yield, and sensitivity is the effect of other parameter variation on the yield. Thus the main effect is related to the variation of the parameter tested, and the sensitivity is the response of the yield to the variations of other parameters (Fig. 3.33). Main effect can be represented by the mean value variation due to a parameter regardless of other parameter values, and sensitivity can be represented by the variance of yields for the same level of the tested parameter.

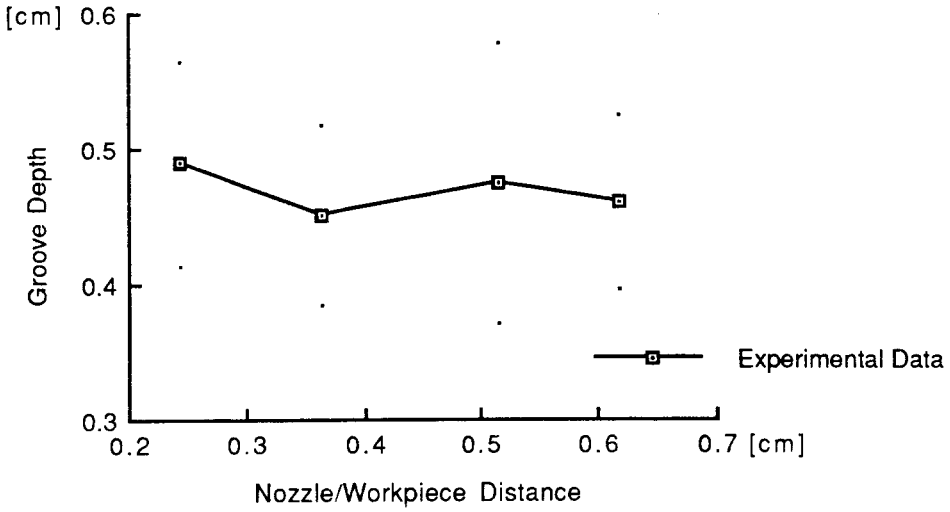



Fig. 3.29: Main Effect of Nozzle/Workpiece Distance on Groove Depth.

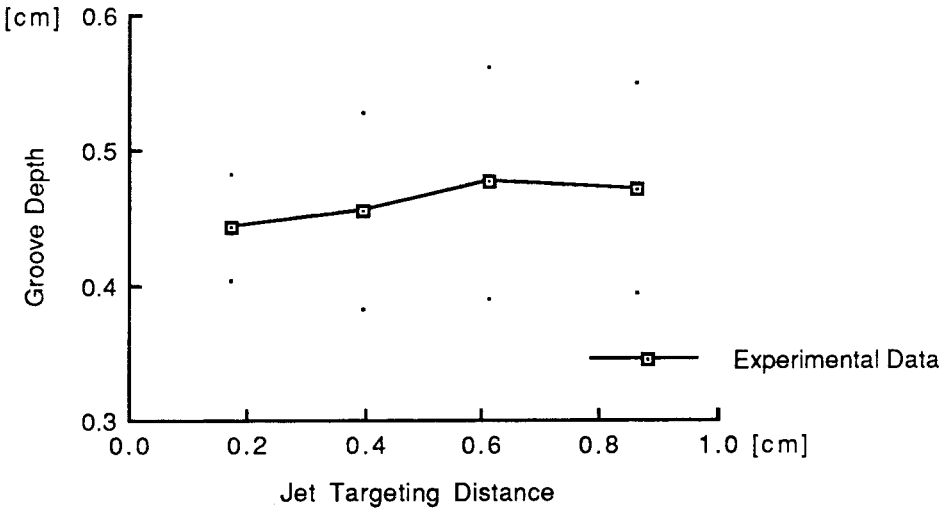



Fig. 3.30: Main Effect of Jet Targeting Distance on Groove Depth.

In order to determine a dominant parameter (control parameter), test ranges should be selected, because the criteria depend on the test ranges. As explained before, the lower limits for the three parameters were selected as the values without causing a confliction between the off-axial and the coaxial nozzles. The upper limit for nozzle/workpiece distance was selected as the first peak (0.53 cm) in Fig. 3.29. The first parts (until the first peak) shows all the major variations, and can duplicate the declining parts. Since deep grooves are of interest, parameter ranges which produce small groove depths are excluded from the ranges for determining the control parameter. Fig. 3.30 shows that there is an

optimal jet targeting distance which produces the maximum groove depth. The optimal jet targeting distance was selected as the upper limit. Fig. 3.31 shows that 4 bar is an optimal reservoir pressure. The value was taken as the upper limit for reservoir pressure.

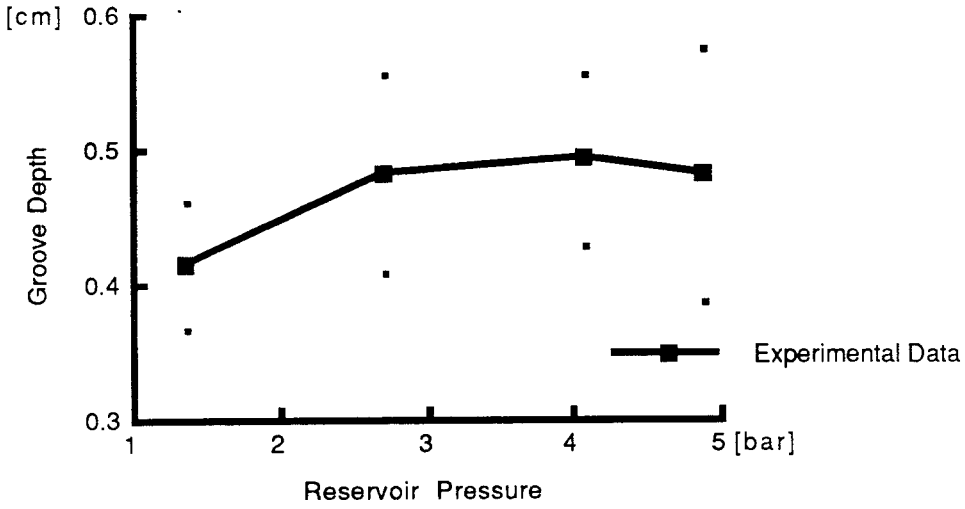



Fig. 3.31: Main Effect of Reservoir Pressure on Groove Depth.

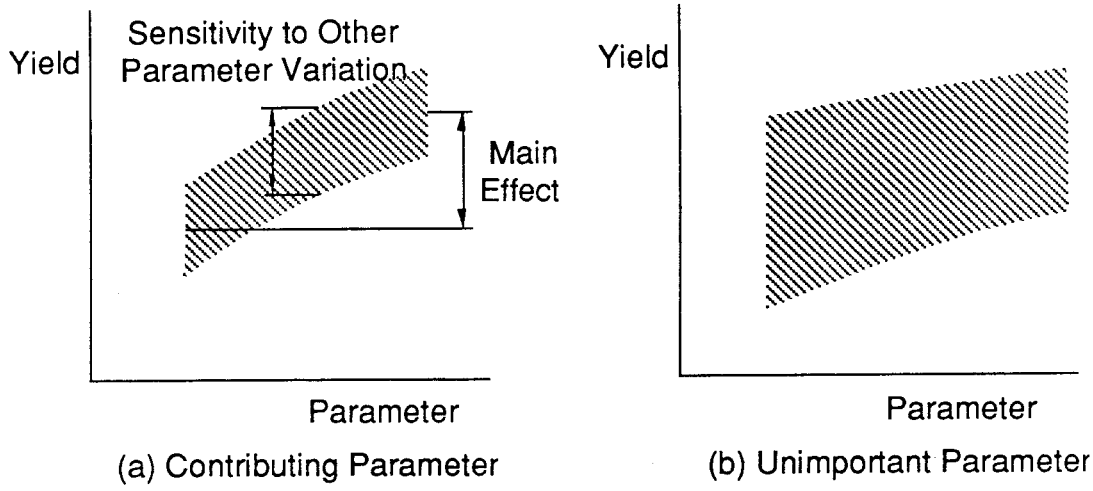



Fig. 3.32: Main Effect and Sensitivity of a Parameter.

In this analysis, total sum of yields is

$$T = \sum_{i=1}^{N} y_i \tag{3.4}$$

where N is the total number of trials, and $y_i$ is the yield at i-th trial. The overall average yield is

$$\bar{T} = \frac{T}{N} \tag{3.5}$$

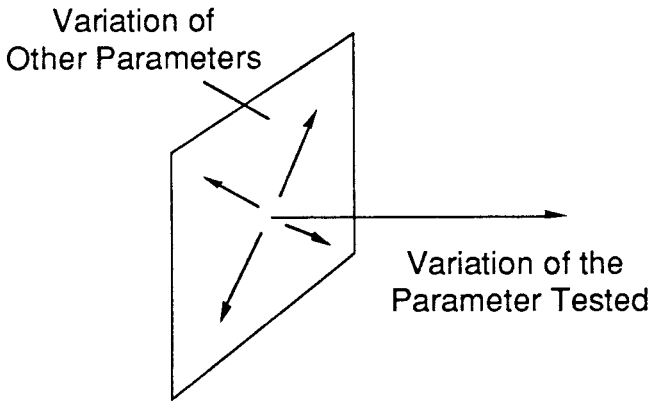



Fig. 3.33: Variations of Parameters.

The sum of squares of the total is

$$SS_T = \left( \sum y_i \right)^2 - \frac{T^2}{N} \tag{3.6}$$

To calculate main effects, sums of yields within a certain level of a parameter are calculated.

$$X_1 = \sum_{i=1}^{n_{X_1}} y_i$$

$$X_2 = \sum_{i=1}^{n_{X_2}} y_i$$

$$\vdots$$

$$X_j = \sum_{i=1}^{n_{X_j}} y_i \qquad (3.7)$$

where X is a parameter, the subscript is the level of the parameter, $X_j$ is the sum of yields for condition $X_j$, and $n_{Xj}$ is the number of trials for $X_j$. Sum of squares with respect to X represents the main effect of parameter X.

$$SS_X = \frac{X_1^2}{n_{X_1}} + \frac{X_2^2}{n_{X_2}} + \ldots - \frac{T^2}{N} \qquad (3.8)$$

Similarly, sums of squares with respect to Y and Z are calculated as:

$$SS_Y = \frac{Y_1^2}{n_{Y_1}} + \frac{Y_2^2}{n_{Y_2}} + \ldots - \frac{T^2}{N} \qquad (3.9)$$

$$SS_Z = \frac{Z_1^2}{n_{Z_1}} + \frac{Z_2^2}{n_{Z_2}} + \ldots - \frac{T^2}{N} \qquad (3.10)$$

Sums of squares (i.e., $SS_X$) represent the main effects of the corresponding parameters. A control parameter should have a large sum of squares.

Representing sensitivity, the variance of $X_1$ can be calculated as

$$V_{X_1} = \frac{1}{(n_{X_1} - 1)} \left( \left( \sum_{i=1}^{n_{X_1}} y_i \right)^2 - \frac{X_1^2}{n_{X_1}} \right) \tag{3.11}$$

Similarly, the variance of $X_j$ can be calculated.

$$V_{X_j} = \frac{1}{(n_{X_j} - 1)} \left( \left( \sum_{i=1}^{n_{X_j}} y_i \right)^2 - \frac{X_j^2}{n_{X_j}} \right) \tag{3.12}$$

The sensitivity of the variation of other parameters at $X_j$ is

$$SEN_{X_j} = V_{X_j} \tag{3.13}$$

Sensitivities are also calculated with respect to other parameters Y and Z. The overall sensitivity is defined as the average of sensitivities of all parameter levels.

$$SEN_X = \frac{1}{n_X} \left( \sum_{i=1}^{n_X} SEN_{X_i} \right) \tag{3.14}$$

Within the test ranges, the main effects and sensitivities were calculated for the three parameters (Table 3.6). It shows that reservoir pressure has the largest sum of square of main effects and smallest sensitivity to the variations in other parameters. Thus reservoir pressure is determined as a dominant (control) parameter. This feature is also shown in Fig. 3.29-3.31.

| *Parameter* | *SS(Main)* | *Sensitivity* |
|---|---|---|
| Nozzle/Workpiece Distance | 0.00304 | 0.00697 |
| Jet Targeting Distance | 0.00399 | 0.00464 |
| Reservoir Pressure | 0.01030 | 0.00388 |

Conditions: Laser Beam Power = 500W
Beam Scanning Velocity = 0.508 cm/s

Beam Spot Diameter = 0.0178 cm
Workpiece Material = $Al_2O_3$
Nozzle Type = Simply Convergent
Nozzle Exit Shape = 0.1 x 0.5 cm Oval

Table 3.6: Main Effects and Sensitivities of Three Jet Parameters.

## Test III

In the previous test, reservoir pressure was found to be important, and nozzle/workpiece distance and jet targeting distance were found to be coupled. If two parameters are coupled each other, a combination of the two parameters rather than single values for those parameters is important. In this test, broad ranges as well as many values for the two parameters were examined to investigate the coupled effect between the two parameters so that the best conditions for the jet parameters can be determined. In this test, reservoir pressure was fixed at 4.08 bar, nozzle/workpiece distance was varied from 0.25 to 0.65, and jet targeting distance was varied from 0.1 to 1.7 cm. The same oval shape nozzle was used, and the same process condition was used (laser power = 500 W and scanning velocity = 0.508 cm/s) as in Test II.

Table 3.7 shows the jet parameter values and the corresponding groove depth for Test III. It also shows that the groove depth is in the range of 0.15 and 0.53 cm depending on the two jet parameter values. Fig. 3.34 shows groove depth vs. jet targeting distance, and Fig. 3.35 shows groove depth vs. nozzle/workpiece distance. Two figures show that nozzle/workpiece distance and jet targeting distance are highly coupled.

Unit [cm]

| *NWD* | *JTD* | *Groove Depth* |
|---|---|---|
| 0.3 | 0.1 | 0.359 |
| 0.3 | 0.5 | 0.335 |
| 0.3 | 0.9 | 0.519 |
| 0.3 | 1.3 | 0.354 |
| 0.3 | 1.7 | clogged |
| 0.4 | 0.1 | 0.450 |
| 0.4 | 0.5 | 0.240 |
| 0.4 | 0.9 | 0.283 |
| 0.4 | 1.3 | 0.451 |
| 0.4 | 1.7 | 0.299 |
| 0.5 | 0.1 | 0.530 |
| 0.5 | 0.5 | 0.491 |
| 0.5 | 0.9 | 0.386 |

| | | |
|---|---|---|
| 0.5 | 1.3 | 0.266 |
| 0.5 | 1.7 | 0.280 |
| 0.6 | 0.1 | 0.456 |
| 0.6 | 0.5 | 0.186 |
| 0.6 | 0.9 | 0.157 |
| 0.6 | 1.3 | 0.235 |
| 0.6 | 1.7 | 0.168 |
| 0.25 | 0.3 | 0.491 |
| 0.25 | 0.7 | 0.412 |
| 0.25 | 1.1 | 0.450 |
| 0.35 | 0.3 | 0.532 |
| 0.35 | 0.7 | 0.448 |
| 0.35 | 1.1 | 0.344 |
| 0.45 | 0.3 | 0.432 |
| 0.45 | 0.7 | 0.437 |
| 0.45 | 1.1 | 0.520 |
| 0.55 | 0.3 | 0.443 |
| 0.55 | 0.7 | 0.419 |
| 0.55 | 1.1 | 0.277 |
| 0.65 | 0.3 | 0.229 |
| 0.65 | 0.7 | 0.366 |
| 0.65 | 1.1 | 0.219 |

Table 3.7: Jet Parameters and Groove Depths (Test III).

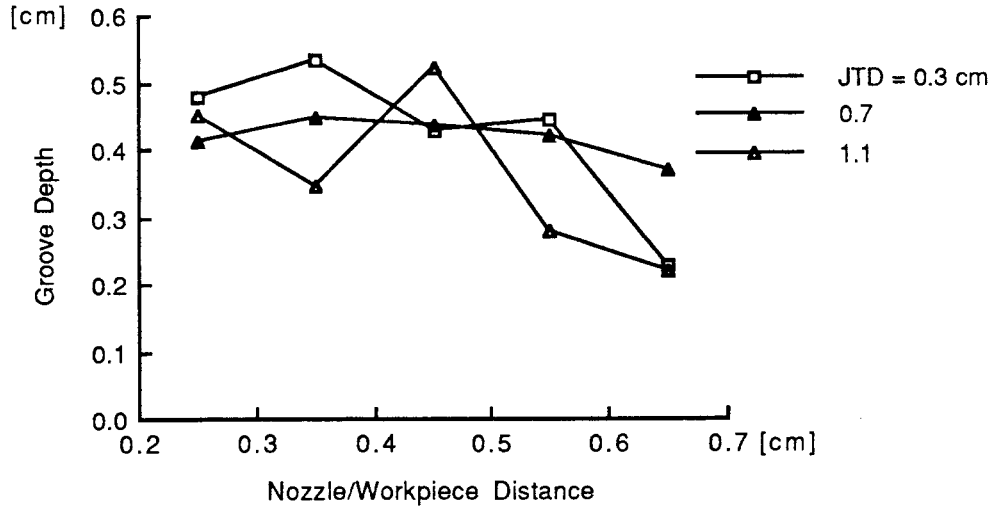



Fig. 3.34: Groove Depth vs. Nozzle/Workpiece Distance.

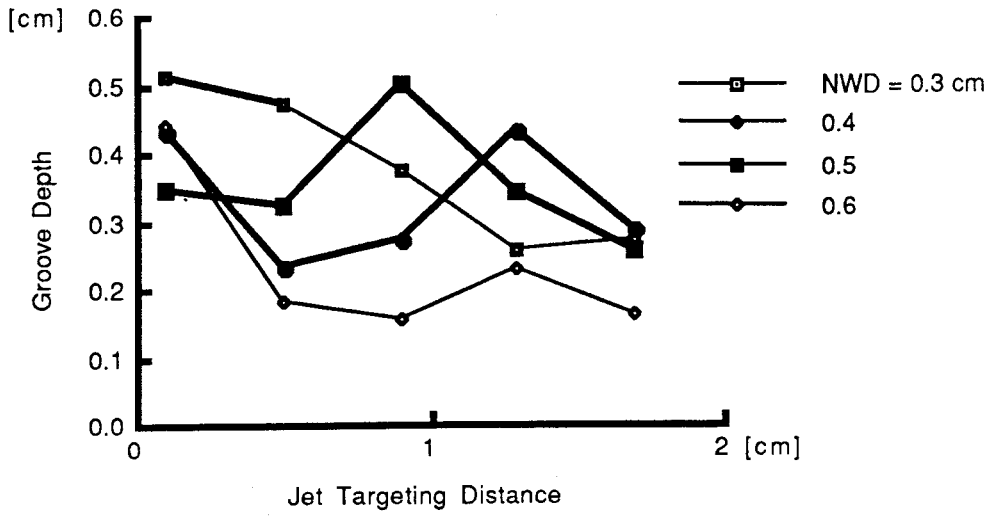



Fig. 3.35: Groove Depth vs. Jet Targeting Distance.

Fig. 3.36 shows the quality of the grooves on the two-dimensional plane of nozzle/workpiece distance and jet targeting distance. It is shown that if either nozzle/workpiece distance or jet targeting distance is too large, the groove quality is poor regardless of the value of the other parameter. Within the range of nozzle/workpiece distance less than 0.6 cm and jet targeting distance less than 1.6 cm, a combination of the two parameters becomes important rather than single values.

From the Test II data, a regression equation was obtained over nozzle/workpiece distance and jet targeting distance. A regression equation can be used to check the coupledness between nozzle/workpiece distance and jet targeting distance and to find the parameter values to yield the maximum groove depth. The regression equation was assumed to have the following polynomial form

$$\begin{aligned} D = \; & a_1 + a_2(NWD) + a_3(JTD) \\ & + a_4(NWD)^2 + a_5(JTD)^2 + a_6(NWD)(JTD) \\ & + a_7(NWD)^3 + a_8(JTD)^3 + a_9(NWD)^2(JTD) + a_{10}(NWD)(JTD)^2 \\ & + a_{11}(NWD)^4 + a_{12}(JTD)^4 + a_{13}(NWD)^3(JTD) + a_{14}(NWD)^2(JTD)^2 \\ & + a_{15}(NWD)(JTD)^3 \end{aligned} \tag{3.15}$$




Fig. 3.36: Groove Quality on Two-Dimensional Plane of Nozzle/Workpiece Distance and Jet Targeting Distance.

Nozzle/workpiece distance and jet targeting distance were normalized by the maximum values. A least square method was used to determine the coefficients fitting the experimental data best. Among various trials with different orders, the most accurate equation was determined as

$$\begin{aligned} D = \quad & 11.5 + 70.0(NWD) - 1.41(JTD) \\ & + 161(NWD)^2 + 4.97(JTD)^2 + 0.50(NWD)(JTD) \\ & - 158(NWD)^3 - 5.50(JTD)^3 - 0.314(NWD)^2(JTD) - 2.06(NWD)(JTD)^2 \\ & + 56.2(NWD)^4 + 1780(JTD)^4 - 1780(NWD)^3(JTD) - 0.563(NWD)^2(JTD)^2 \\ & + 3.068(NWD)(JTD)^3 \end{aligned} \tag{3.16}$$

which has the smallest root mean square 0.0382. The root mean square was defined as

$$\text{Root Mean Square} = \frac{1}{nD_{average}} \left( \sum_{1}^{n} (D_{calculated} - D_{measured})^2 \right) \tag{3.17}$$

Eq. (3.17) shows that low order main effects and higher order coupled effects are important. The FORTRAN program for regression is listed in Appendix C.

The best jet condition which can be an operating condition should produce a large groove depth and be stable to the variations in parameters. A stable condition means that

unexpected variations or small setting errors in parameters do not result in a large variation in the groove depth. Signal-to-Noise ratio (SN ratio) in the Taguchi method [76] can represent stability. Noise can be small variation of parameters. If an SN ratio is large for a certain jet condition, a small deviation from the jet condition does not result in a large variation in the groove depth. Groove depth as well as stability is considered to determine the best jet condition. A condition that exhibits a large mean value but a small SN ratio may not be the best condition, since the groove depth corresponding to the condition is sensitive to the variation of parameters.

Mean values and SN ratios are calculated for the experimental conditions shown in Fig. 3.37. The black point is the test condition, and the gray points surrounding the black point represent small parameter variations from the test condition. Mean value, m, can be calculated as

$$m = \frac{1}{n}\left(\sum y_i\right) \tag{3.18}$$

where n is the number of conditions for one black point, and $y_i$ is the yield. In this case, n is 5, including the black point. To calculate the SN ratio, variances and sums of squares are calculated.

$$V = \frac{\sum y_i^2 - n\,m^2}{n - 1} \tag{3.19}$$

$$S_m = \frac{1}{n}\left(\sum y_i\right)^2 \tag{3.20}$$

SN ratio, $\eta$, is defined as

$$\eta = 10 \log_{10}\left(\frac{S_m - V}{nV}\right) \tag{3.21}$$

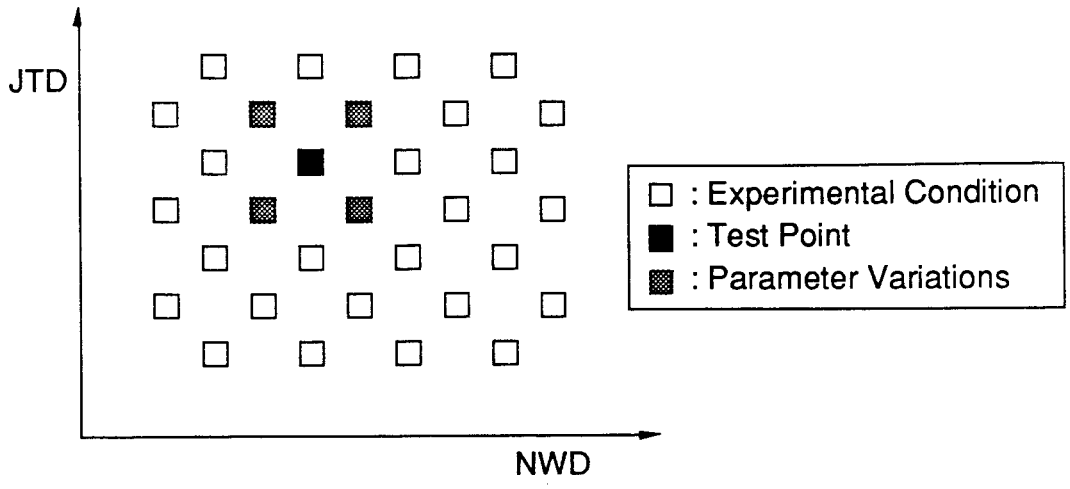



Fig. 3.37: Parameter Conditions for Signal-To-Noise Ratio Calculation.
Black Point: conditions where SN ratios are calculated
Gray Point: conditions due to the variations of parameters.

Table 3.8 lists the means and SN ratios for several test conditions which have high SN ratios. Condition JTD = 0.5 cm and NWD = 0.5 cm was selected as the best grooving condition for the following reasons:

1. the condition produces a relatively deep groove
2. the groove depth for the condition is the least sensitive to small variations of parameters

| *NWD* *cm* | *JTD* *cm* | *Mean* *cm* | *SN Ratio* *db* |
|---|---|---|---|
| 0.3 | 0.5 | 0.441 | 15.51 |
| 0.3 | 0.9 | 0.434 | 16.65 |
| 0.4 | 0.1 | 0.469 | 18.56 |
| 0.5 | 0.1 | 0.467 | 18.50 |
| 0.5 | 0.5 | 0.443 | 23.91 |

Table 3.8: Means and Signal-to-Noise Ratios for Several Test Conditions.

3. the condition has relatively large nozzle/workpiece distance and jet targeting distance, since small distances (which means setting of an off-axial nozzle close to a coaxial nozzle and a workpiece) might cause setting confliction with a coaxial nozzle.

The best jet condition was selected for the oval and convergent nozzle as follows:

| *Parameter* | *Best Condition* | |
|---|---|---|
| Nozzle/Workpiece Distance | 0.5 | cm |
| Jet Targeting Distance | 0.5 | cm |
| Reservoir Pressure | 4.08 | bar |
| Jet Attack Angle | 60° | |

Conditions: Laser Beam Power = 500W
Beam Scanning Velocity = 0.508 cm/s
Beam Spot Diameter = 0.0178 cm
Workpiece Material = $Al_2O_3$
Nozzle Type = Simply Convergent
Nozzle Exit Shape = 0.1 x 0.5 cm Oval

The best jet condition found above is not absolutely best for different process conditions. Suppose that a best nozzle configuration is found to be Fig. 3.38 (a) for a ceratin groove depth, D. For a groove depth $\gamma D$ ($\gamma>0$), if all the length scales are extended $\gamma$ times, the two configurations become geometrically similar. However, groove widths do not nearly change for various process conditions. Thus, only a two-dimensional geometric similarity is possible when the jet flow in the groove width direction is negligible. Since the supersonic cell size is proportional to the nozzle exit diameter, a dynamic similarity exists. Inside the groove, the flow is three-dimensional due to the boundary layer effect, and the boundary layer thickness for different groove depths will be different. When the boundary layer thicknesses are negligible compared with the groove width, two grooving situations are geometrically as well as dynamically similar to each other. For groove depths less than a certain critical groove depth (which has negligible boundary layer thickness compared with the groove width), there exists a similarity, and the best jet configuration found for one groove depth can be applied to other cases.

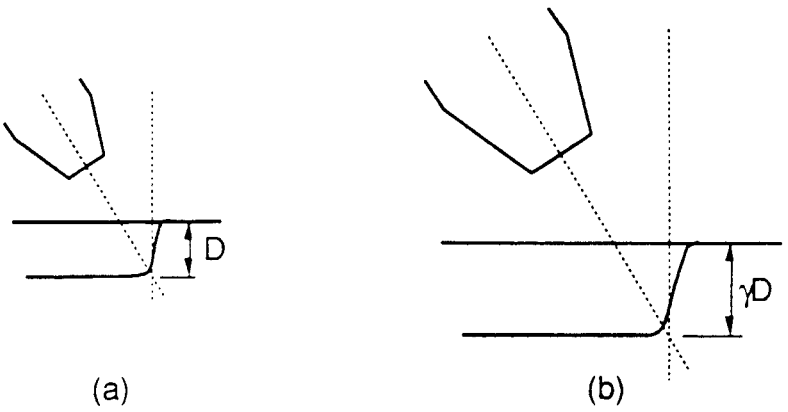



Fig. 3.38: Geometric and Dynamic Similarity between Two Configurations.

### 3.2.3 Grooving test for various process conditions

This test was performed to check the validity of the theoretical solutions. The laser power was varied from 300 to 600 W in CW mode. The number of laser beam passes was 1 or 2. The jet parameters were set according to the best jet condition found in the grooving tests. The best jet condition found in the previous tests corresponds to a certain groove depth. Thus, various jet conditions near the best jet condition were tried, and deep grooves were chosen.

To describe the combined effect of the laser power and the scanning velocity, a parameter, non-dimensional energy, was introduced and defined as the amount of laser energy applied on a workpiece surface divided by the amount of energy needed to melt unit volume of the material. The non-dimensional energy can be expressed as

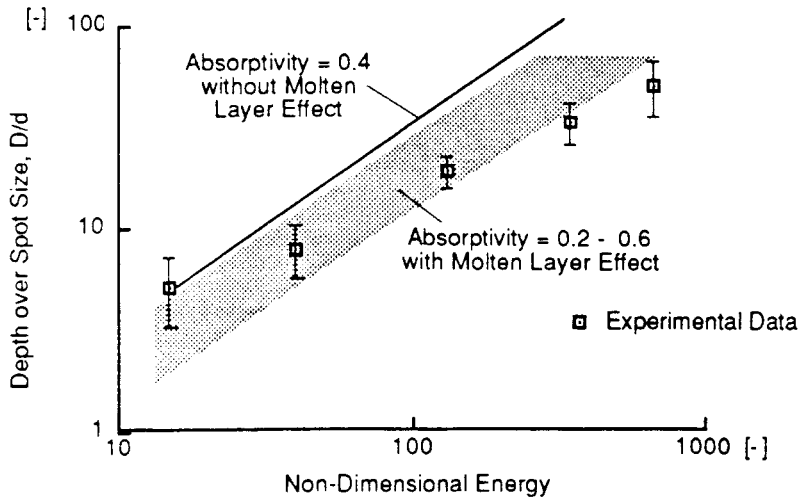
$$\text{Non-Dimensional Energy} = \frac{\left(\frac{P\lambda}{vd^2}\right)}{\rho L} = \frac{P\lambda}{\rho L v d^2} \tag{3.22}$$

where $\lambda$ is the number of beam passes. While the non-dimensional energy allows the consideration of the combined effect of power and scanning velocity on the grooving process, it does not account for beam interaction time over the workpiece, which implies that different groove shapes may result from the same non-dimensional energy. Despite

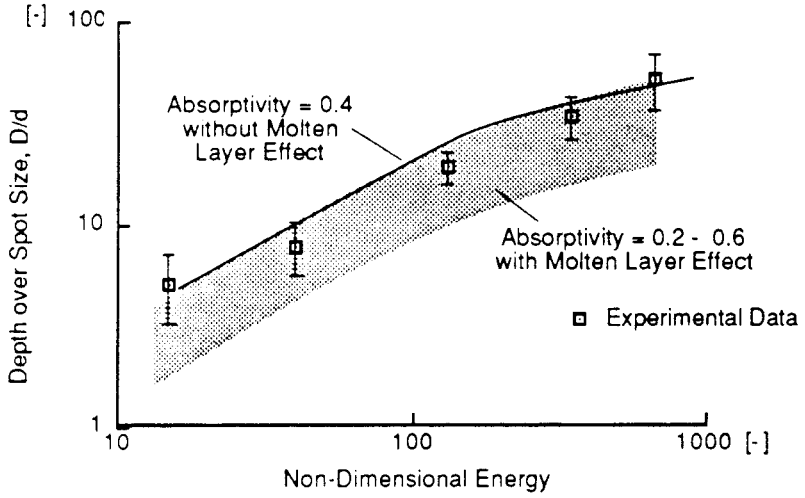
this drawback, the concept of the non-dimensional energy offers a comprehensive way to present and compare various theoretical and experimental results.

In order to check if molten layer effect is negligible, a molten layer thickness should be measured. However, a molten layer thickness is difficult to measure. Resolidified layer thicknesses, which are close to molten layer thicknesses, were experimentally measured instead. The ratio of the resolidified layer thickness to the groove width was found to be in the range of 0.1 and 0.3. Therefore, molten layer effect cannot be ignored. In Fig. 3.39, a comparison between the theoretical and the experimental results is presented. The groove depths were calculated based on the procedure described in Chap. 2. In calculating molten layer thicknesses, 1.09 bar, which is the gage stagnation pressure after a Mach shock for 4.08 bar of reservoir pressure, was used for the pressure difference along the cutting front. A good agreement is shown with the exception of the analytical solution. The analytical solution over-estimates the groove depth. This is because of the simplification of the temperature derivatives in the analytical solution, which under-estimates the conduction heat. The numerical solution predicts the groove depths best, and the modified solution under-estimates the groove depths for non-dimensional energies higher than 100. The modified and numerical solutions are very close to each other in the non-dimensional energies less than 200. The absorptivity, which makes the numerical solution fit the experimental data best, is about 0.5.

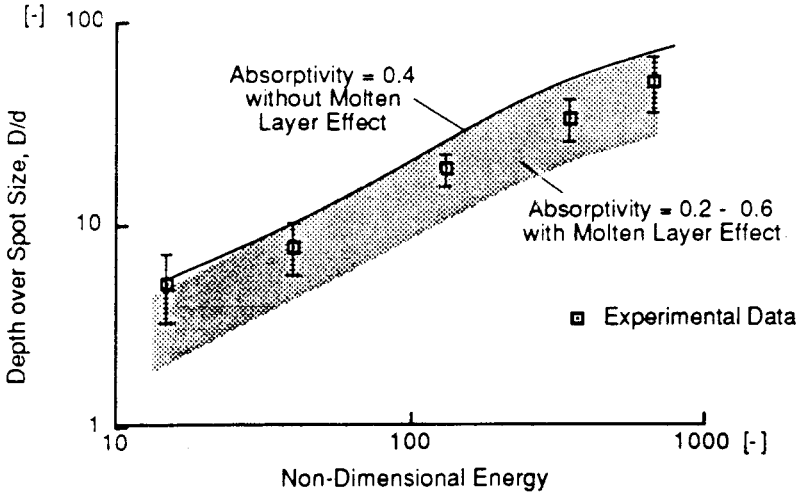
By using two laser beams, three-dimensional laser machining was performed. This test was attempted to find the influence of one laser beam on the grooving process of the other beam. In order to be able to measure the groove depth, a workpiece was set tilted so that two groove ends meet together (Fig. 3.40) at a certain position. Otherwise, it is very difficult to make the two groove ends meet together. Also, the groove depth cannot be measured correctly, since the boundary conditions become different. The tilting angle was kept small to make the resulting transient effect negligible. The laser power was fixed at 500 W, and the scanning velocity was varied from 0.254 to 2.54 cm/s. Fig. 3.41 shows that the groove depths in the three-dimensional laser machining are slightly greater than the average groove depths made by single beam. The difference in the groove depths for the two cases can be explained by the difference in the conduction heat through the plane which is symmetric in the case of the three-dimensional laser machining. However, the difference in the conduction heats is not significant compared with other heat loss components.




(a) Analytical Solution




(b) Modified Solution




(c) Numerical Solution

Fig. 3.39: Groove Depth vs. Non-Dimensional Energy in Laser Grooving ($Al_2O_3$).

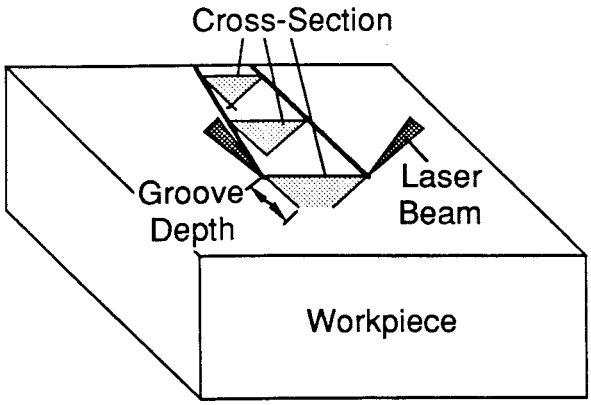



Fig. 3.40: Test Setup for Three-Dimensional Laser Machining.

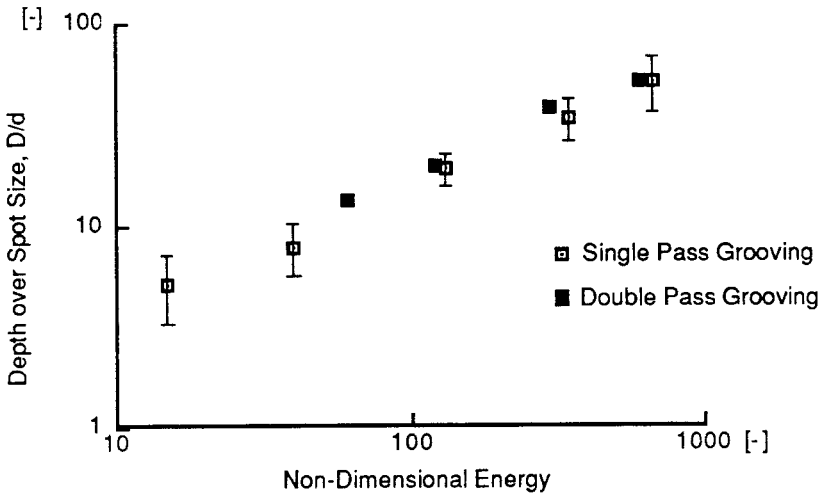



Fig. 3.41: Groove Depths for Single and Double Beam Grooving ($Al_2O_3$).

Material removal rates are shown in Fig. 3.42 for various processes [77]. The workpiece materials are metals and alloys. The processes which have high material removal rates per unit power input can be called efficient. For instance, ECM has lower efficiency than EDM, although ECM is a higher power and higher removal process than EDM. The material removal rate of the three-dimensional laser machining is calculated as

$$\begin{aligned} \text{Material Removal Rate} &= (\text{Groove Depth})^2(\text{Scanning Velocity}) \\ &= (0.53)^2(0.508)\ \text{cm}^3/\text{s} \\ &= 513.7\ \text{cm}^3/\text{hr} \\ &= 31.3\ \text{in}^3/\text{hr} \end{aligned} \tag{3.23}$$

The workpiece material in the three-dimensional laser machining is aluminum oxide. Since the groove depth data in three-dimensional laser machining for metals and alloys are not available, a direct comparison between the machining efficiencies of the three-dimensional laser machining and other processes cannot be made. However, the groove depths for ceramic materials are of almost the same order of magnitude as those for metals and alloys and a rough comparison can be made. In LBM (laser beam machining), material is removed in a molten or vaporized form, while in the three-dimensional laser machining mostly in a solid form. As shown in Fig. 3.42, the material removal rates per unit power input for LBM and the three-dimensional laser machining are $2.5 \times 10^{-5}$ and $3 \times 10^{-2}$ $in^3/hr$ W, respectively. This means that the efficiency of the three-dimensional laser machining is 3 orders of magnitude higher than the single-beam-laser machining. Fig. 3.42 also shows that three-dimensional laser machining has a slightly lower efficiency than the conventional milling based on the same power input.

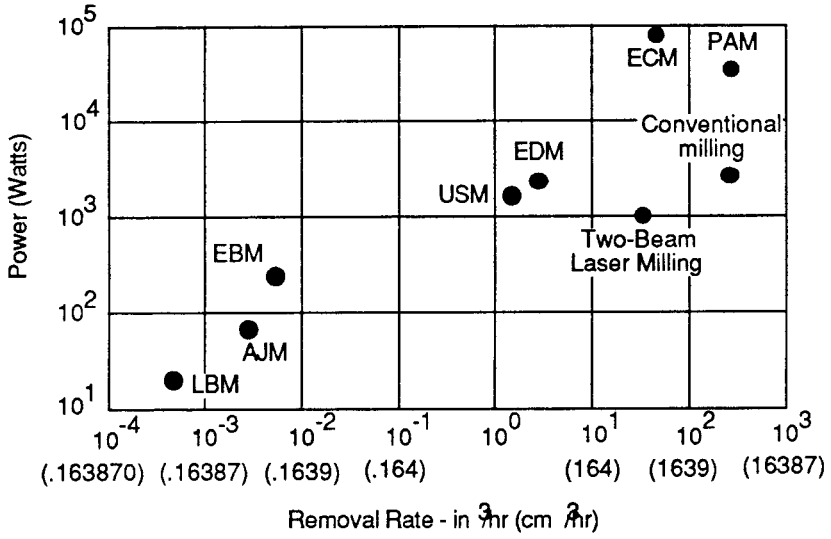



Fig. 3.42: Material Removal Rates for Various Processes [77].

An optimal set of process variables in three-dimensional machining is mathematically derived in Appendix D.

# CHAP 4. CONCLUSIONS

To understand the physical mechanisms in grooving, a theoretical analysis was performed. Based on a simple estimation of the driving force for molten material expulsion, groove depths were predicted. The predicted groove depths by the theoretical solutions showed a good agreements with the experimental results. The absorptivity value whic fits the experimental data best was found to be 0.5.

To find the effects of gas jets on grooving, two types of tests were performed. Gas jet tests were performed to understand supersonic jet behavior and to find the effects of gas jets on the pressure distribution on the cutting front, which is the driving force for molten material expulsion; grooving tests were also performed to find the effects of gas jets on groove depth. An off-axial gas jet increased groove depth up to 30 per cent. Especially in deep grooves, off-axial jets were able to reject molten material. It was found that the groove depth depended significantly on the gas jet parameter values. Reservoir pressure was found to be a dominant parameter. The best jet condition which yielded a relatively deep groove and was not sensitive to small variations in parameters was determined by using a statistical method.

The three-dimensional laser machining was performed to find the effect of two beams on groove depth for aluminum oxide material. The groove depths in three-dimensional laser machining were slightly greater than the average groove depths in single beam grooving. This is because in the three-dimensional machining there exists a symmetry plane across which heat is not conducted and conduction heat loss is reduced. The material removal rate of the three-dimensional laser machining was found to be substantially increased compared with that of the single beam grooving.

Future research directions include further detail theoretical study of molten layer flow, further experimental work on three-dimensional machining, and development of process control for laser machining processes.

## REFERENCES


[1] Chryssolouris, G., "Stock Removal by Laser Cutting," U.S. Patent Application Serial No. 640764, (Aug. 1984).

[2] Chryssolouris, G., and J. Bredt, and S. Kordas, "Laser Turning for Difficult to Machine Materials," *Proceedings of the Simposium on Machining of Ceramic Materials and Components, ASME, PED*, (Vol. 17, Nov 1985), pp. 9-17.

[3] Chryssolouris, G., and J. Bredt, "Machining of Ceramics Using a Laser Lathe," *Int. Ceramic Review*, (Vol. 37, No. 2, 1988), pp. 43-45.

[4] Chryssolouris, G., et al., "Theoretical Aspects of a Laser Machine Tool," *J. Engineering for Industry*, ASME, (Vol. 110, No. 1, Feb 1988), pp. 65-70.

[5] Eloy, J.-F., Power Lasers (1987).

[6] Chun, M. K., and K. Rose, "Interaction of High-Intensity Laser Beams with Metals," *J. Appl. Phys.*, (Vol. 41, No. 2, 1970), pp. 614-620.

[7] Dabby, F. W., and U.-C. Paek, "High-Intensity Laser-Induced Vaporization and Explosion of Solid Material," *IEEE J. Quantum Electronics* (Vol. QE-8, No. 2, Feb 1972), pp. 106-111.

[8] El-Adawi, M. K., "Laser Melting of Solids-An Exact Solution for Time Intervals Less or Equal to the Transit Time," *J. Appl. Phys.* (Vol. 60, No. 7, Oct 1986), pp. 2256-2265.

[9] Masters, J. I., "Problem of Intense Surface Heating of a Slab Accompanied by Change of Phase," *J. Appl. Phys.* (Vol. 27, No. 5, May 1956), pp. 477-484.

[10] Schvan, P, and R. E. Thomas, "Time-Dependent Heat Flow Calculation of CW Laser-Induced Melting of Silicon," *J. Appl. Phys.* (Vol. 57, No. 10, May 1985), pp. 4738-4741.

[11] Warren, R. E., and M. Sparks, "Laser Heating of a Slab Having Temperature-Dependent Surface Absorptance," *J. Appl. Phys.* (Vol. 50, No. 12, Dec 1979), pp. 7952-7957.

[12] Carslaw, H. S., and J. C. Jaegar, Conuction of Heat in Solid (1959).

[13] Rosenthal, D., "The Theory of Moving Sources of Heat and Its Applications to Metal Treatments," *Transactions of the ASME* (Nov 1946).

[14] El-Adawi, M. K., and E. F. Elshehawey, "Heating a Slab Induced by a Time-Dependent Laser Irradiance-An Exact Solution," *J. Appl. Phys.* (Vol. 60, No. 7, Oct 1986), pp. 2250-2255.

[15] Modest, M. F., and H. Abakians, "Heat Conduction in a Moving Semi-Infinite Solid Subjected to Pulsed Laser Irradiation," *J. Heat Transfer* (Vol. 108, Aug 1986), pp. 597-607.

[16] von Allmen, M., P. Blaser, K. Affolter, and E. Stürmer, "Absorption Phenomena in Metal Drilling with Nd-Lasers," *IEEE J. Quantum Electronics* (Vol. QE-14, No. 2, Feb 1978), pp. 85-88.

[17] Kocher, E., L. Tschudi, J. Steffen, and G. Herziger, "Dynamics of Laser Processign in Transparent Media," *IEEE J. Quantum Electronics*, (Vol. QE-8, No.2, Feb 1972), pp. 120-125.

[18] Gagliano, F. P., and U. C. Paek, "Observation of Laser-Induced Explosion of Solid Materials and Correlation with Theory," *Appl. Optics*, (Vol. 13, No. 2, Feb 1974), pp. 274-279.

[19] Kocher, E., "Material Processing with Solid State Lasers: Drilling, Cutting, and Welding," *Optoelectronics Conf. Proc.*, 1975, pp.105-108.

[20] Barber, R., "Hole Drilling with Lasers," *Creative Manuf. Engg. Programs*, MR74-951.

[21] Longfellow, J., "High Speed Drilling in Alumina Substrates with a $CO_2$ Laser," *Ceramic Bulletin* (Vol. 50, No. 3, 1971), pp. 251-253.

[22] Wagner, R. E., "Laser Drilling Mechanics," *J. Appl. Phys.* (Vol. 45, No. 10, Oct 1974), pp. 4631-4637.

[23] Hamilton, D. C., and I. R. Pashby, "Hole Drilling Studies with a Variable Pulse Length $CO_2$ Laser," *Optics and Laser Technology*, (Aug. 1979), pp. 183-188.

[24] Paek, U. C., and F. P. Gagliano, "Thermal Analysis of Laser Drilling Processes," *IEEE J. Quantum Electronics* (Vol. QE-8, No. 2, Feb 1972), pp. 112-119.

[25] Bush, A. J., and F. J. Kromer, "Simplification of the Hole-Drilling Method of Residual Stress Measurement," *ISA Transaction* (Vol. 12, No. 3, Dec 1973), pp. 249-259.

[26] Sparks, M., "Theory of Laser Heating of Solids: Metals," *J. Appl. Phys.* (Vol. 47, No. 3, Mar 1976), pp. 837-849.

[27] Brugger, K., "Exact Solutions for the Temperature Rise in a Laser-Heated Slab," *J. Appl. Phys.* (Vol. 43, No. 2, Feb 1972), pp. 577-583.

[28] Arata, Y., and I. Miyamoto, "Some Fundamental Properties of High Power Laser Beam as a Heat Source (Report 1) - Beam Focusing Characteristics of $CO_2$ Laser," *Transactions of the Japan Welding Soc.*, (Vol. 3, No. 1, Apr 1972), pp. 143-151.

[29] Schulz, W., G. Simon, H. M. Urbassek, and I. Decker, "On Laser Fusion Cutting of Metals," *J. Phys. D: Appl. Phys.* (Vol. 20, 1987), pp. 481-488.

[30] Schuoecker, D., and W. Abel, "Material Removal Mechanism of Laser Cutting," *SPIE*, (Sep 1983), pp. 88-95.

[31] Bunting, K. A., and G. Cornfield, "Toward a General Theory of Cutting:A Relationship Between the Incident Power Density and the Cut Speed," *J. Heat Transfer* (Feb 1975), pp. 116-122.

[32] Petring, D., P. Abels, E. Beyer, and G. Herziger, "Werkstoffbearbeitung mit Laserstrahlung," *Feinwerktechnik & Messtechnik* (Vol. 96, 1988), pp. 364-372.

[33] Lee, C. S., A. Goel, and H. Osada, "Parametric Studies of Pulsed-Laser Cutting of Thin Metal Plates," *J. Appl. Phys.* (Vol. 58, No. 3, Aug 1985), pp. 1339-1343.

[34] Chryssolouris, G., and W. C. Choi, "Gas Jet Effects on Laser Cutting," *SPIE*, (Jan 1989).

[35] Schuocker, D., and P. Muller, "Dynamic Effects in Laser Cutting and Formation of Periodic Striations," *SPIE* (Vol. 801, 1987), 258-264.

[36] Vicanek, M., G. Simon, H. M. Urbassek, and I. Decker, "Hydrodynamical Instability of Melt Flow in Laser Cutting," *J. Phys. D: Appl. Phys.* (Vol. 20, 1987), pp. 140-145.

[37] Sharp, C. M., "Laser Welding and Drilling," *SPIE Fourth European Electro Optics Conference*, (Vol. 164, Oct 1978), pp. 271-278.

[38] Banas, C. M., "High Power Laser Welding," *Optical Enginnering*, (Vol. 17, No. 3, May-Jun 1978), pp. 210-216.

[39] Cline, H. E., and T. R. Anthony, "Surface Rippling Induced by Surface-Tension Gradients during Laser Surface Melting and Alloying," *J. Appl. Phys.*, (Vol. 48, No. 9, Sep 1977), pp. 3895-3900.

[40] Andrews, J. G., and D. R. Atthey, "Hydrodynamic Limit to Penetration of a Material by a High-Power Beam," *J. Phys., D/ British*, (Vol. 9, No. 15, 1976), pp. 2181-2194.

[41] Klemens, P. G., "Heat Balance and Flow Conditions for Electron Beam and Laser Welding," *J. Appl. Phys.*, (Vol. 47, No. 5, May 1976), pp. 2165-2174.

[42] Chan, C., J. Mazumder, and M. M. Chen, "Perturbation Model for Three-Dimensional Thermocapillary Convection in Laser Melt Pool," *ASME Winter Annual Meeting*, (Dec, 1986), pp. 1-8.

[43] Dowden, J., M. Davis, and P. Kapadia, "The Flow of Heat and the Motion of the Weld Pool in Penetration," *J. Appl. Phys.*, (Vol. 57, No. 9, May 1985), pp. 4474-4479.

[44] Dowden, J., N. Postacioglu, M. Davis, and P. Kapadia, "A Keyhole Model in Penetration Welding with a Laser," *J. Phys D: Appl. Phys.*, (Vol. 20 1987), pp. 36-44.

[45] Anthony, T. R., and H. E. Cline, "Surface Rippling Induced by Surface-Tension Gradients during Laser Surface Melting and Alloying," *J. Appl. Phys.*, (Vol. 48, No. 9, Sep 1977), pp. 3888-3894.

[46] Modest, M. F. and H. Abakians, "Evaporative Cutting of a Semi-Infinite Body with a Moving CW Laser," *J. Heat Transfer*, (Aug 1986), pp. 602-607.

[47] Chryssolouris, G., and W. C. Choi, "Theoretical Aspects of Laser Grooving," *Proceedings, 14th Conference on Production Research and Technology*, (1987), pp. 323-331.

[48] Copley, S. M., M. Bass, and R. G. Wallace, "Shaping Silicon Compound Ceramics with a Continuous Wave Carbon Dioxide Laser," *Proceedings, Second International Symposium on Ceramic Machining and Finishing*, (1978), pp. 97-104.

[49] Chryssolouris, G, P. S. Sheng, and W. C. Choi, "Analysis on the Laser Machining Process for Ceramics and Composite Materials," *Proceedings 15th Conference on Res. & Tech.* Jan (1989).

[50] Meyer, G. H., "An Application of the Method of Lines to Multidimensional Free Boundary Problems," *J. the Institutue of Mathematics and Its Applications*, (Vol. 20, Nov 1977), pp. 317-329.

[51] Meyer, G. H., "The Method of Lines and Invariant Imbedding for Elliptic and Parabolic Free Boundary Problems," *SIAM J on Numerical Analysis*, (Vol. 18, Feb 1981), pp. 150-164.

[52] Nielsen, S. E., "Laser Cutting with High Pressure Cutting Gases and Mixed Cutting Gases", PhD Thesis, Inst. Mfg. Eng., Technical University of Denmark, (1985).

[53] Fieret, J., and B. A. Ward, "Circular and Non-Circular Nozzle Exits fro Supersonic Gas Jet Assist in $CO_2$ Laser Cutting", *Proc. 3rd Intl. Conf. on Lasers in Mfg. (LIM3)*, Paris, (1986).

[54] Ward, B. A., "Supersonic Characteristics of Nozzles Used with Lasers for Cutting", 94/*L.I.A., ICALEO* (Vol. 44, 1984), pp. 94-101.

[55] Chryssolouris, G., W. C. Choi, S. B. Kyi, and P. Sheng, "Investigation of the Effects of a Gas Jet on Laser Grooving," *NAMRI of SME* , (May 1987), pp. 217-222.

[56] Vicanek, M., and G. Simon, "Momentum and Heat Transfer of an Inert Gas Jet to the Melt in Laser Cutting", *J. Phys. D: Appl. Phys.* (Vol. 20, 1987), pp. 1191-1196.

[57] Donaldson, C. D., and R. S. Snedeker, "A Study of Free Jet Impingement. Part 1. Mean Properties of Free and Impinging Jets", *J. Fluid Mech.*, (Vol. 45, 1971), 281-319.

[58] Gubanova, O. I., V. V. Lunev, and L. N. Plastinina, "The Central Breakaway Zone with Interaction between a Supersonic Unexpanded Jet and a Barrier", *Fluid Dynamics*, (Vol. 6, 1973), pp. 298-301.

[59] Gummer, J. H., and B. L. Hunt, "The Impingement of Non-Uniform, Axisymmetric Supersonic Jets on a Perpendicular Flat Plate", *Israel J. Technology*, (Vol. 12, 1974), pp. 221-235.

[60] Belov, I. A., I. P. Ginzburg, and L. I. Shub, "Supersonic Underexpanded Jet Impingement upon Flat Plate", *Int. J. Heat Mass Transfer*, (Vol. 16), pp. 2067-2076.

[61] Vick, A. R., and E. H. Anderson Jr., "An Investigation of Highly Under-expanded Exhaust Plumes Impinging upon a Perpendicular Flat Surface", *NASA TN D-3269.*

[62] Prandtl, Essentials of Fluid Dynamics, (1952), p. 269.

[63] Pack, D. C., "On the Formation of Shock-Waves in Supersonic Gas Jets", *Quarterly J. Mechanics and Applied Math.*, (Vol. 1, 1948), pp. 1-17.

[64] Love, E. S., C. E. Grisby, L. P. Lee, and M. J. Woodling, "Experimental and Theoretical Studies of Axisymmetric Free Jets", *NASA TR R-6.*

[65] Holt, M., "Direct Calculation of Pressure Distribution on Blunt Hypersonic Nose Shapes With Sharp Corners", *J. Aero Sci*, (Vol. 28), pp. 872-876.

[66] Traugott, S., "An Approximate Solution of the Direct Supersonic Blunt-Body Problem for Arbitrary Axisymmetric Shapes", *J. Aero Sci*, (Vol. 27), pp. 361-370.

[67] Hayes, W. D., and R. F. Probstein, Hypersonic Flow Theory, pp. 166-200.

[68] South, J. C., "Calculation of Axisymmetric Supersonic Flow Past Blunt Body with Sonic Corners, Including a Program Description and Listing", *NASA TN D-4563.*

[69] Sabersky, R. H., A. J. Acosta, and E. G. Hauptman, Fluid Flow, (1971), p258.

[70] Touloukian, Y. S., Thermophysical Properties of Matter, (1970).

[71] Box, G. E. P., and S. Bisgaard, "Statistical Tools for Improving Designs," *Mech. Eng.*, (Vol. 33, Jan 1988), pp. 32-40.

[72] Box, G. E. P., and K. B. Wilson, "On the Experimental Attainment of Optimum Conditions," *J. Royal Statistical Society B*, (Vol. 13, 1951), pp. 1-45.

[73] Finney, D. J., "The Fractional Replication of Factorial Arrangements," *Annals of Eugenics*, (Vol. 12), pp. 291-301.

[74] Davies, O. L., and W. A. Hay, "The Construction and Uses of Fractional Factorial Designs in Industrial Research," *Biometrics*, (Jun 1950), pp. 233-249.

[75] Suh, N. P., The Principles of Design, (1989).

[76] Taguchi, G., System of Experimental Design, Vol. 1 and 2, (1987).

[77] Weller, E. J., and M. Haavisto, Nontraditional Machining Processes, (1984).

## Appendix A: Gas Jet Effects on Laser Cutting

Jet interaction and heat transfer aspects are analyzed independently. This is appropriate since the molten layer is relatively thin due to the easy removal of molten material in laser cutting. Molten layer thickness is determined for a given jet configuration. Later the cutting depth is determined based on the thickness of the molten layer. The momentum theorem can be used for the analysis of jet interaction with a grooved workpiece in which the detailed jet flow is not critical. Since an off-axial jet removes most of the molten material, only the off-axial jet is considered. To simplify the analysis, the following assumptions are made.

- The jet flow is two-dimensional inside the kerf.
- The kerf wall is parallel to the laser beam.
- The shear force exerted on the molten layer by the melting front is negligible as compared with other forces.
- The static pressure of the jet is ambient at the kerf exit

As shown in Fig. 1, a control volume covering the nozzle exit and the kerf is considered. The momentum balance in the direction parallel to the erosion front can be written as:

$$A_p(p_j - p_a)\sin\phi = \dot{m}_3 v_3 + \dot{m}_4 v_4 - \dot{m}_2 v_2 \sin\phi - \dot{m}_1 v_1 \sin\phi \tag{1}$$

where: $A_p$: area
$p_j$: jet static pressure
$\phi$: jet attack angle

The molten material velocity is determined from the following expression:

$$v_3 = (A_p(p_j - p_a)\sin\phi + (\dot{m}_1 v_1 - \dot{m}_2 v_2)\sin\phi - \dot{m}_4 v_4)/\dot{m}_3 \tag{2}$$

where

$$\dot{m}_4 = \dot{m}_1 - \dot{m}_2 \tag{3}$$

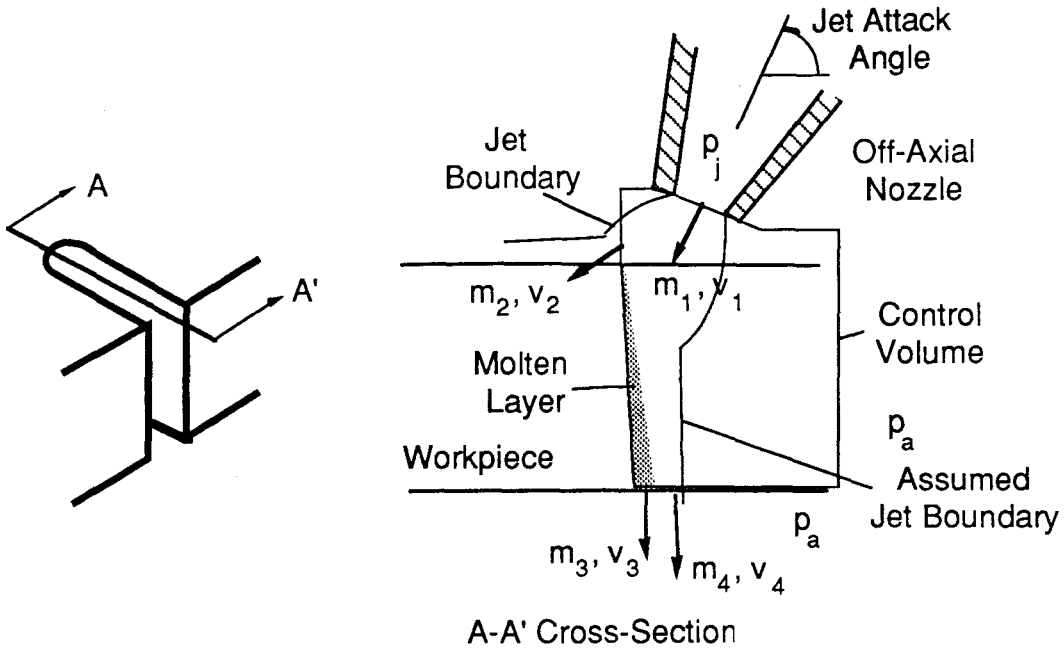



Fig. 1: Off-axial Jet Interaction with a Kerf

Since the jet diameter increases after the nozzle exit, a portion of the jet penetrates into the kerf. The area, $A_p$, which is a function of reservoir pressure and nozzle-workpiece distance, can be calculated from the jet diameter. The jet pressure at the nozzle exit, $p_j$, is determined uniquely by the reservoir pressure. The mass flow rates, $m_1$ and $m_2$, can be determined from the geometry of the jet configuration, and the velocity, $v_2$, is approximated from a free jet velocity. The velocity, $v_4$, at the kerf exit, which contains all the information of the jet history from the nozzle up to the kerf exit, is unknown. In this paper, the jet velocity at the kerf exit is assumed to be sonic. In the Schlieren photographs of supersonic jets inside kerfs, the jet condition at the kerf exit is close to sonic.

With respect to a coordinate system moving with the laser beam, material in a solid state is fed into the molten layer, and it is ejected from the molten layer in a liquid state. As shown in Fig. 2, the mass balance in the molten layer gives

$$m_3 = \text{material fed into the control volume in solid state} = \text{material removed from the control volume in liquid state} \quad (4)$$

$$\dot{m}_3 = \rho v w D = \frac{\pi}{2}\left(\left(\frac{w}{2}\right)^2 - \left(\frac{d}{2}\right)^2\right)\rho v_3 \cong \frac{\pi}{2}\rho v_3 w t \tag{5}$$

where: ρ: density
v: scanning velocity
w: groove width
D: groove depth
d: beam diameter
t: molten layer thickness

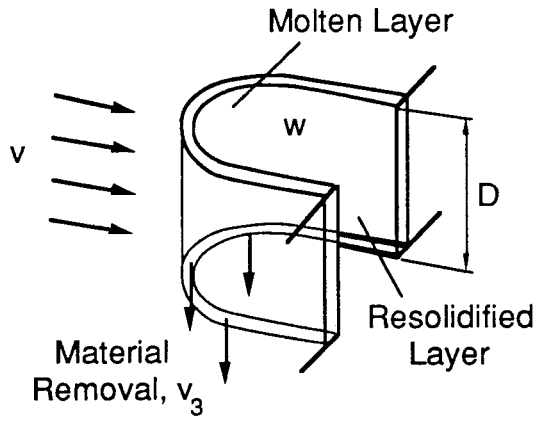



Fig. 2: Material Balance at the Erosion Front

In calculating $m_3$, the laser beam diameter is used instead of w since the molten layer thickness is negligible compared to the beam diameter. From Eq. (5), the thickness of the molten layer can be calculated.

$$t = \frac{2vD}{\pi v_3} \tag{6}$$

Eq. (6) shows that as the scanning velocity increases, the molten layer thickness and workpiece thickness increase, and the momentum transferred from the jet decreases.

For a given laser power, scanning velocity, and molten layer thickness, the cutting depth is determined. Assuming that except for reflected heat loss, heat losses are

negligible, the absorbed laser power melts material and heats the surrounding medium to its melting point. The molten layer is assumed to be at its melting point. Since in laser cutting the thickness of the molten layer is very small, this is a reasonable assumption.

$$\text{absorbed laser power} = \text{melting heat} + \text{conduction heat} \tag{7}$$

$$aP = \rho vwDL + \int_{-\pi/2}^{\pi/2} -k\left(\frac{\partial T}{\partial n}\right)_{n=0} Bd\theta D = wD\left(\rho vL - k\int_{0}^{\pi/2}\left(\frac{\partial T}{\partial n}\right)_{n=0} d\theta\right) \tag{8}$$

where:
- a: absorptivity
- P: laser power
- L: latent heat of fusion
- k: thermal conductivity
- n: heat conduction direction
- $\theta$: angle
- B: half of kerf width = w/2

The cutting depth is determined from Eq. (8).

$$D = \frac{aP}{w\left(\rho vL - k\int_{0}^{\pi/2}\left(\frac{\partial T}{\partial n}\right)_{n=0} d\theta\right)} \tag{9}$$

In order to calculate the temperature gradient at the melting front, the integral method is used. The assumptions are made that heat transfer in the z-direction is negligible and the melting front is cylindrical. In Fig. 3, an energy balance is considered in an infinitesimal control volume of angle $d\theta$ covering from the melting front to beyond the heat affected zone. At $\theta = \theta$, the heat convected into the control volume, $P_1$, is

$$P_1 = \rho c_p v \sin\theta \int_{B}^{H} Tdr \tag{10}$$

where: H: large distance beyond penetration depth
cp: specific heat.

At $\theta = \theta + d\theta$, the heat convected out of the control volume, $P_2$, is

$$P_2 = \rho c_p v \sin\theta \int_B^H T dr + \frac{\partial}{\partial\theta}\left(\rho c_p v \sin\theta \int_B^H T dr\right) d\theta \tag{11}$$

The heat due to material moving into the control volume, $P_3$, is

$$P_3 = \rho c_p v T_o H \cos\theta \, d\theta \tag{12}$$

where: $T_o$: ambient temperature.

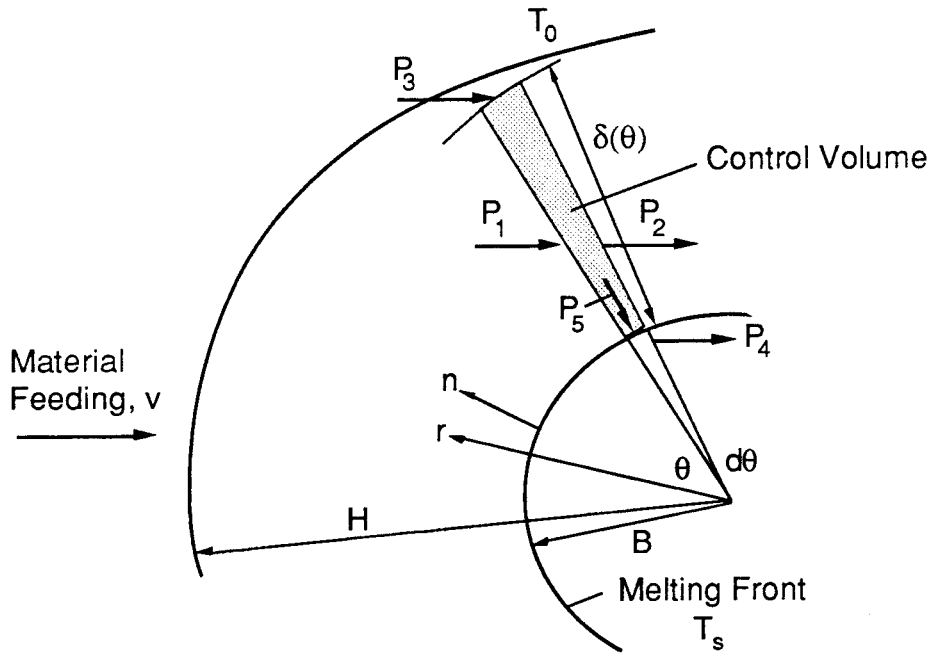



Fig. 3: Heat Balance in Heat Affected Zone

The heat due to material moving across the melting front, $P_4$, is

$$P_4 = \rho c_p v T_s B \cos\theta \, d\theta \tag{13}$$

where: Ts: erosion front temperature.

Conduction heat from the melting front, $P_5$, is

$$P_5 = - k \left( \frac{\partial T}{\partial r} \right)_{r=B} B d\theta \tag{14}$$

where: r: radial coordinate.

The temperature distribution inside the medium is assumed to be an exponential function of distance from the melting front, satisfying the boundary conditions:

$$\begin{aligned} &\text{at } r = R, T = T_s, \text{ and} \\ &\text{as } r \rightarrow \infty, T = T_o \end{aligned} \tag{15}$$

$$\frac{T - T_o}{T_s - T_o} = \exp\left( \frac{- 2(r - B)}{\delta(\theta)} \right) \tag{16}$$

The penetration depth, $\delta$, is a function of $\theta$ only. The energy balance in the control volume is

$$P_1 + P_3 + P_5 = P_2 + P_4 \tag{17}$$

$$\rho c_p v T_o H \cos\theta \, d\theta + \frac{2k}{\delta} (T_s - T_o) B \, d\theta = \frac{\partial}{\partial \theta} \left( \rho c_p v \sin\theta \int_B^H T dr \right) d\theta + \rho c_p v T_s B \cos\theta \, d\theta \tag{18}$$

Dividing by $\rho c_p v d\theta$, Eq. (18) can be rewritten as:

$$T_o H \cos\theta + \frac{2\alpha}{v\delta} (T_s - T_o) B = \frac{\partial}{\partial \theta} \left( \sin\theta \int_B^H T dr \right) + T_s B \cos\theta \tag{19}$$

or

$$\frac{2\alpha}{v\delta}(T_s - T_o)B = \frac{\partial}{\partial\theta}\left(\sin\theta\left(\int_B^H Tdr - T_o(H - B)\right)\right) + (T_s - T_o)B\cos\theta \tag{20}$$

or

$$\frac{2\alpha}{v\delta}(T_s - T_o)B = \frac{\partial}{\partial\theta}\left(\sin\theta\int_B^H (T - T_o)dr\right) + (T_s - T_o)B\cos\theta \tag{21}$$

The integral part of the first term on the right-hand side in Eq. (21) is

$$\int_B^H (T - T_o)dr = \int_B^H (T_s - T_o)\exp\left(\frac{-2(r - B)}{\delta}\right)dr$$

$$= (T_s - T_o)\left(-\frac{\delta}{2}\right)\left(\exp\left(\frac{-2(H - B)}{\delta}\right) - \exp\left(\frac{-2(B - B)}{\delta}\right)\right)$$

$$= (T_s - T_o)\frac{\delta}{2} \tag{22}$$

The energy balance (21) is rewritten as:

$$\frac{2\alpha B}{v\delta} = \cos\theta\frac{\delta}{2} + \sin\theta\frac{1}{2}\frac{d\delta}{d\theta} + B\cos\theta \tag{23}$$

or

$$\frac{d\delta}{d\theta} + \frac{\delta}{\tan\theta} + \frac{2B}{\tan\theta} - \frac{4\alpha B}{v\delta\sin\theta} = 0 \tag{24}$$

By the symmetry, the boundary condition at $\theta = 0$ is

$$\frac{d\delta(0)}{d\theta} = 0 \tag{25}$$

With the above boundary condition, initial value of $\delta$ can be determined for a one-dimensional case ($B \rightarrow \infty$) to check if Eq. (24) is derived correctly.

$$\delta(0) = \frac{2\alpha}{v} \tag{26}$$

The penetration depth for a flat heat source can be found from the temperature distribution for a one-dimensional case.

$$\frac{T - T_o}{T_s - T_o} = \exp\left(-\frac{vx}{\alpha}\right) = \exp\left(\frac{-2(r - B)}{2\alpha/v}\right) \tag{27}$$

The penetration depth agrees with the value derived above.

With the penetration depth known, the cutting depth can be determined.

$$D = \frac{aP}{w\left(\rho v L + 2k(T_s - T_o)\int_0^{\pi/2} \frac{d\theta}{\delta(\theta)}\right)} \tag{28}$$

Fig. 4 shows the cutting depth vs. energy density. Based on the conditions of the jet parameters, the analytical solution is calculated, and plotted for constant power and for constant scanning velocity. A good agreement is shown between the analytical and experimental results. For high energy density, the discrepancy becomes large. This is due to beam defocussing effects. The analytical solution, which assumes a non-divergent beam, over-estimates the cutting depth in deep kerfs, where the beam defocussing becomes significant.

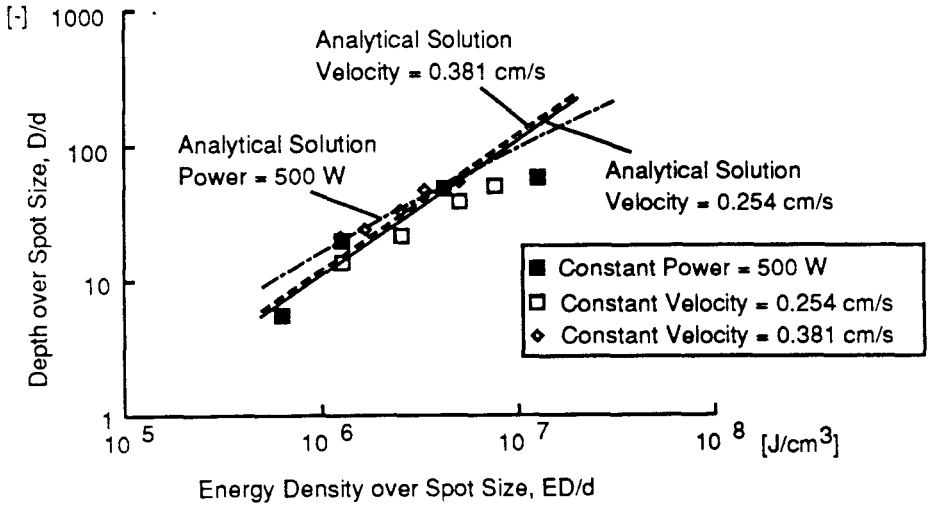



Fig. 4: Energy Density vs. Cutting Depth.

# Appendix B. Fortran Program for Numerical Analysis

```
C       PROGRAM: GROOVE FORMATION IN TWO LASER BEAM GROOVING
C
C
C
C               DEFINITION OF VARIABLES
C
C       SURI:    TEMPORY SURFACE DEPTH
C       SURO:    OLD SURFACE DEPTH
C       SURN:    NEW SURFACE DEPTH
C       L:       INTEGER SURFACE DEPTH
C       TPO:     OLD TEMPERATURE
C       TPN:     NEW TEMPERATURE
C       R1,R2,R3:        RICCATI FUNCTIONS
C       W:       RICCATI FUNCTION
C       DX:      MESH SIZE IN THE SCANNING DIRECTION
C       DY:      MESH SIZE IN THE DIRECTION NORMAL TO THE SCANNING DIRECTION
C       DZ:      MESH SIZE IN THE LASER BEAM DIRECTION
C       NODX:    NUMBER OF NODES IN THE X-DIRECTION
C       NODY:    NUMBER OF NODES IN THE Y-DIRECTION
C       NODZ:    NUMBER OF NODES IN THE Z-DIRECTION
C       TO:      AMBIENT TEMPERATURE
C       TM:      MELTING TEMPERATURE
C       QKF:     LATENT HEAT OF FUSION
C       C:       SPECIFIC HEAT
C       RO:      FOCUSED BEAM RADIUS
C       V:       SCANNING VELOCITY
C       POWER:   LASER BEAM POWER
C       AS:      ABSORPTIVITY
C       QLAM:    THERMAL CONDUCTIVITY
C       EPST:    TOLERANCE FOR TEMPERATURE CHANGE
C       EPSS:    TOLERANCE FOR TEMPERATURE CHANGE
C       TIMMAX:  MAXIMUM ITERATION TIME
C       OMEGA:   RELAXATION FACTOR
C       WAVEL:   BEAM WAVE LENGTH
C       ITMAX:   MAXIMUM ITERATION
C       RFT:
C       XMIN:    MINIMUM X VALUE
C       XMAX:    MAXIMUM X VALUE
C       YMIN:    MINIMUM Y VALUE
C       YMAX:    MAXIMUM Y VALUE
C       ZMIN:    MINIMUM Z VALUE
C       ZMAX:    MAXIMUM Z VALUE
C       A1,A2,A3:        COEFFICIENTS
C       DZL:     CONDUCTIVITY DIVIDED BY MESH SIZE IN Z DIRECTION
C       HB1,HT1,HW1,HW2,HW31,HW32,HW33,HW4,HW5,HW61,HW62,HW63: COEFFICIENTS
C       DX2I,DY2I,RCZ,RCZV,RCZVX,ZLX2,HB1:       COEFFICIENTS
C       PI:      3.14159
C       X:       X VALUE
C       Y:       Y VALUE
C       Z:       Z VALUE
C       XS:      X VALUE OF SOURCE CENTER LOCATION
C       YS:      Y VALUE OF SOURCE CENTER LOCATION
C       I:       NODE VALUE IN X DIRECTION
C       J:       NODE NUMBER IN Y DIRECTION
C       K:       NODE NUMBER IN Z DIRECTION
C       KK:      DUMMY VARIABLE
C       HBL:
C       ZNORM:   SURFACE INCLINATION
C       ZNORM2:  SQUARE OF ZNORM
C       TIME:    INTERACTION TIME
```

```
C       SUR:    TEMPORARY SURFACE DEPTH
C       SURMOVE:        TEMPORARY SURFACE DEPTH IN CASE OF NO ABALTION
C       SURMAX: MAXIMUM SURFACE DEPTH CHANGE
C       TEMMAX: MAXIMUM TEMPERATURE CHANGE
C       BCON1:  FUNCTION DETERMINING BOUNDARY
C       BCON2:  FUNCTION DETERMINING BOUNDARY
C       IT:     ITERATION NUMBER
C       ITERRE: ITERATION NUMBER FOR DIFFERENT PROCESS CONDITIONS
C       M:      NUMBER OF PROCESS CONDITIONS
C       ABARA,ABARB,ABARC,ABAR1,ABAR2,ABAR3:    COEFFICIENTS
C       AA,CCC: COEFFICIENTS
C       TT:     TEMPORARY TEMPERATURE
C       RS:     RICCATI FUNCTION
C       WS:     RICCATI FUNCTION
C       RADZ2:  SQUARE OF BEAM RADIUS (DEFOCUSED BEAM)
C       SOUR:   LASER BEAM HEAT SOURCE
C       XS:     X VALUE OF SOURCE LOCATION
C       YS:     Y VALUE OF SOURCE LOCATION
C       KK:     TEMPORARY NODAL VALUE OF TOP SURFACE
C
C               SUBROUTINES
C
C       HREAD:  READ INPUT VRIABLES
C       HCOEF:  CALCULATE COEFFICIENTS
C       HCALR:  CALCULATE RICCATI FUNCTIONS
C       HINIT:  ASSIGN INITIAL CONDITIONS
C       HREPL:  UPDATE TEMPERATURES AND SURFACE DEPTHS
C       HNORM:  CALCULATE SURFACE INCLINATION
C       HMAIN:  DETERMINE WHETHER OR NOT ABLATION OCCURS
C       HNOAB:  CALCULATE TMEPERATURES IN CASE OF NO ABLATION
C       HABLA:  CALCULATE TEMPERATURES AND SURFACE DEPTHS IN CASE OF ABLATION
C       HBOUV:  ASSIGN BOUNDARY CONDITIONS
C
C
C
C
      COMMON/D1/SURI(20,20),SURO(20,20),SURN(20,20),L(20,20)
      COMMON/D2/TPO(20,20,1000),TPN(20,20,1000)
      COMMON/D3/R1(20,1000),R2(20,1000),R3(20,1000),W(20,1000)
      COMMON/C1/DX,DY,DZ,DT,NODX,NODY,NODZ,TO,TM,QKF,C,RO
      COMMON/C2/V,POWER,RADIUS,AS,QLAM,EPST,EPSS,TIMMAX,OMEGA,WAVEL
      COMMON/C3/ITMAX,RFT,XMIN,XMAX,YMIN,YMAX,ZMIN,ZMAX,DZL
      COMMON/C4/HB1,HT1,HW1,HW2,HW31,HW32,HW33,HW4,HW5,HW61,HW62,HW63
      COMMON/E1/PI,X,Y,Z,I,J,K,KK,HBL,ZNORM ZNORM2,TIME
      COMMON/E2/SUR,SURMOVE,SURMAX,TEMMAX,BCON1,BCON2,IT
      COMMON/E3/ITERRE
      COMMON/E4/XS,YS,KI
C
C
      OPEN(UNIT=1,FILE='THREEDIN.DAT',STATUS='OLD')
      OPEN(UNIT=2,FILE='THREEDOUT.DAT',STATUS='NEW')
      OPEN(UNIT=3,FILE='THREEDTEMPOUT.DAT',STATUS='NEW')
C
C
      PI = 4.0*ATAN(1.0)
                    CALL HREAD
                    CALL HCOEF
                    CALL HCALR
      READ(1,40)M
40    FORMAT(/2X,I10)
```

```
C
C
      DO 2001 III=1,M
      READ(1,41)POWER,V
41    FORMAT(/2X,2F10.5)
      WRITE(2,79)POWER,V
      WRITE(3,79)POWER,V
      WRITE(2,81)
C
C
80    FORMAT(2X,I5,2F10.5)
79    FORMAT(1H1//2X,'POWER =',F10.3,'  VELOCITY =',F10.5////)
                  CALL HINIT
C
C
      DO 1000 IT=1,ITMAX
              TIME = DT*IT
      DO 960 ITER=1,ITERRE
                  CALL HREPL
C
C
      DO 990 I=2,NODX-1
      DO 990 J=2,NODY
                  CALL HNORM
              BCON1 = -1.0E+20
              KI=1+(J-1)*DY/DZ
C
C             SWEEP FROM THE BOTTOM BOUNDARY TO THE TOP SURFACE
C
      DO 995 K=KI,L(I,J)
                  CALL HMAIN
              IF(BCON2.LT.0.)GOTO 993
              KK=K
              L(I,J)=K
              GOTO 500
993           BCON1=BCON2
995   CONTINUE
              KK=L(I,J)
C
C             IF BCON2 IS LESS THAN ZERO, NO ABLATION OCCURS
C
                  CALL HNOAB
              GOTO 990
C
C             IF BCON2 IS GREATER THAN ZERO, ABLATION OCCURS
C
500                   CALL HABLA
C
C
              IF(TEMMAX.LE.EPST.AND.SURMAX.LE.EPSS)GOTO 700
990   CONTINUE
                  CALL HBOUV
960   CONTINUE
1000  CONTINUE
C
C             PRINT OUTPUT
C
700   WRITE(2,65)((SURN(I,J),I=1,NODX),J=1,NODY)
      WRITE(2,67)((L(I,J),I=1,NODX),J=1,NODY)
C
```

```
C
      DO 1501 K=NODZ,1,-1
              WRITE(3,66)((TPN(I,J,K),I=1,NODX),J=1,NODY)
1501  CONTINUE
65    FORMAT(/2X,11F10.5)
66    FORMAT(/2X,11F10.3)
67    FORMAT(/2X,11I5)
      WRITE(2,68)
68    FORMAT(1H1)
2001  CONTINUE
      END


      SUBROUTINE HBOUV
      COMMON/D1/SURI(20,20),SURO(20,20),SURN(20,20),L(20,20)
      COMMON/D2/TPO(20,20,1000),TPN(20,20,1000)
      COMMON/C1/DX,DY,DZ,DT,NODX,NODY,NODZ,TO,TM,QKF,C,RO
      COMMON/E4/XS,YS,KI
C
C
              DO 605 J=1,NODY
              SURN(NODX,J)=SURN(NODX-1,J)
              L(NODX,J)=L(NODX-1,J)
              DO 605 K=1,NODZ
              TPN(NODX,J,K)=TPN(NODX-1,J,K)
605           CONTINUE
C
C
              DO 720 J=1,NODY
              DO 720 I=1,NODX
              SURN(I+1,J)=AMIN1(SURN(I,J),SURN(I+1,J))
              IF(L(I+1,J).GT.L(I,J))L(I+1,J)=L(I,J)
720           CONTINUE
      RETURN
      END


      SUBROUTINE HREPL
      COMMON/D1/SURI(20,20),SURO(20,20),SURN(20,20),L(20,20)
      COMMON/D2/TPO(20,20,1000),TPN(20,20,1000)
      COMMON/C1/DX,DY,DZ,DT,NODX,NODY,NODZ,TO,TM,QKF,C,RO
      COMMON/E2/SUR,SURMOVE,SURMAX,TEMMAX,BCON1,BCON2,IT
      COMMON/E4/XS,YS,KI
C
C
              DO 203 I=1,NODX
              DO 203 J=1,NODY
                      SURO(I,J) = SURN(I,J)
                      SURI(I,J) = SURN(I,J)
              DO 204 K=1,NODZ
                      TPO(I,J,K) = TPN(I,J,K)
204           CONTINUE
              KI=1+(J-1)*DY/DZ
              DO 205 K=1,KI-1
                      TPO(I,J,K) = TPN(I,J,KI)
                      TPN(I,J,K) = TPN(I,J,KI)
205           CONTINUE
203           CONTINUE
              TEMMAX = 0.0
              SURMAX = 0.0
```

```
      RETURN
      END


      SUBROUTINE HREAD
      COMMON/C1/DX,DY,DZ,DT,NODX,NODY,NODZ,TO,TM,QKF,C,RO
      COMMON/C2/V,POWER,RADIUS,AS,QLAM,EPST,EPSS,TIMMAX,OMEGA,WAVEL
      COMMON/C3/ITMAX,RFT,XMIN,XMAX,YMIN,YMAX,ZMIN,ZMAX,DZL
      COMMON/E3/ITERRE
      COMMON/E4/XS,YS,KI
C
C
      READ(1,51)DX,DY,DZ,DT,NODX,NODY,NODZ,ITERRE
      WRITE(2,60)
      WRITE(2,51)DX,DY,DZ,DT,NODX,NODY,NODZ,ITERRE
      READ(1,52)TO,TM,QKF,C,RO
      WRITE(2,61)
      WRITE(2,52)TO,TM,QKF,C,RO
      READ(1,52)V,POWER,RADIUS,AS,QLAM
      WRITE(2,62)
      WRITE(2,52)V,POWER,RADIUS,AS,QLAM
      READ(1,52)EPST,EPSS,TIMMAX,OMEGA,WAVEL
      WRITE(2,63)
      WRITE(2,52)EPST,EPSS,TIMMAX,OMEGA,WAVEL
      READ(1,53)XS,YS
      WRITE(2,64)
      WRITE(2,53)XS,YS
51    FORMAT(//2X,4F10.5,4I5)
52    FORMAT(/2X,5F10.5)
53    FORMAT(/2X,2F10.5)
60    FORMAT(/2X,'     DX          DY          DZ          DT         NODX    '
     *          ,'    NODY       NODZ')
61    FORMAT(/2X,'     TO          TM      LATENT      SPECI      DENSITY')
62    FORMAT(/2X,'      V       POWER      RADIUS      ABSOP      CONDUCT')
63    FORMAT(/2X,'    EPST       EPSS      TIMMAX      OMEGA       WAVEL')
C
64    FORMAT(/2X,'     XS          YS')
C
            NODX=NODX+1
            NODY=NODY+1
            NODZ=NODZ+1
            ITMAX=TIMMAX
            XS=0.
            YS=20.-YS
            XMIN= XS-(NODX-1)/2*DX
            XMAX= XS+(NODX-1)/2*DX
            YMIN= YS-(NODY-1)/2*DY
            YMAX= YS+(NODY-1)/2*DY
            DZ=(20.-YMIN)/(NODZ-1.)
            ZMIN= YMIN-20.
            ZMAX= 0.0
      RETURN
      END


      SUBROUTINE HCOEF
      COMMON/C1/DX,DY,DZ,DT,NODX,NODY,NODZ,TO,TM,QKF,C,RO
      COMMON/C2/V,POWER,RADIUS,AS,QLAM,EPST,EPSS,TIMMAX,OMEGA,WAVEL
      COMMON/C3/ITMAX,RFT,XMIN,XMAX,YMIN,YMAX,ZMIN,ZMAX,DZL
      COMMON/C4/HB1,HT1,HW1,HW2,HW31,HW32,HW33,HW4,HW5,HW61,HW62,HW63
```

```
C
C
                DX2I=1./(DX*DX)
                DY2I=1./(DY*DY)
                RCZ=RO*C*DZ
                RCZV=RCZ*V
                RCZVX=RCZV/(2.*DX)
                ZLX2=QLAM*DZ*DX2I
                HB1 = 0.
                HT1 = 2.0*QLAM/DZ
                HW1 = 1./HT1
                HW2 = 0.
                HW31 = RCZVX-ZLX2
                HW32 = 0.
                HW4 = -RCZVX - ZLX2
                HW5 = -QLAM*DZ*DY2I
                HW61 = HW5
                HW62 = HW5
        RETURN
        END


        SUBROUTINE HCALR
        COMMON/D3/R1(20,1000),R2(20,1000),R3(20,1000),W(20,1000)
        COMMON/C1/DX,DY,DZ,DT,NODX,NODY,NODZ,TO,TM,QKF,C,RO
        COMMON/C2/V,POWER,RADIUS,AS,QLAM,EPST,EPSS,TIMMAX,OMEGA,WAVEL
        COMMON/C3/ITMAX,RFT,XMIN,XMAX,YMIN,YMAX,ZMIN,ZMAX,DZL
        COMMON/E4/XS,YS,KI
C
C
        DX2I=1./(DX*DX)
        DY2I=1./(DY*DY)
        A1= 2.*QLAM*(DX2I+DY2I)
        A2= RO*C*V/(2.*DX)+QLAM*(DX2I+2.*DY2I)
        DZL=QLAM/DZ
C
C
        ABARA=SQRT(A1*QLAM)
        ABARB=SQRT(A2*QLAM)
        ABAR1=SQRT(4.*A1/QLAM)
        ABAR2=SQRT(4.*A2/QLAM)
C
C
        DO 300 J=1,NODY
                        KI=1+(J-1)*DY/DZ
                        R1(J,KI)=DZL
                        R2(J,KI)=DZL
                DO 301 K=KI,NODZ
                        CONST=(DZL-ABARA)/(DZL+ABARA)
                        AA=-ABAR1*(K-1)*DZ
                        IF(ABS(AA).LE.1E6)GOTO 302
                        R1(J,K)=ABARA
                        GOTO 301
302                     EXPAA=EXP(AA)
                        CEXPAA=CONST*EXPAA
                        R1(J,K)=ABARA*(1.+CEXPAA)/(1.-CEXPAA)
301             CONTINUE
C
C
                DO 311 K=KI,NODZ
```

```
                        CONST=(DZL-ABARB)/(DZL+ABARB)
                        AA=-ABAR2*(K-1)*DZ
                        IF(ABS(AA).LE.1E6)GOTO 312
                        R2(J,K)=ABARB
                        GOTO 311
 312                    EXPAA=EXP(AA)
                        CEXPAA=CONST*EXPAA
                        R2(J,K)=ABARB*(1.+CEXPAA)/(1.-CEXPAA)
 311            CONTINUE
 300    CONTINUE
 C
 C
        RETURN
        END


        SUBROUTINE HINIT
        COMMON/D1/SURI(20,20),SURO(20,20),SURN(20,20),L(20,20)
        COMMON/D2/TPO(20,20,1000),TPN(20,20,1000)
        COMMON/D3/R1(20,1000),R2(20,1000),R3(20,1000),W(20,1000)
        COMMON/C1/DX,DY,DZ,DT,NODX,NODY,NODZ,TO,TM,QKF,C,RO
 C
 C
                DO 202 I=1,NODX
                DO 202 J=1,NODY
                        SURN(I,J)=0.0
                        SURI(I,J)=0.0
                        L(I,J)=NODZ
                DO 201 K=1,NODZ
                        TPN(I,J,K)=TO
 201            CONTINUE
 202            CONTINUE
        RETURN
        END


        SUBROUTINE HNORM
        COMMON/D1/SURI(20,20),SURO(20,20),SURN(20,20),L(20,20)
        COMMON/D2/TPO(20,20,1000),TPN(20,20,1000)
        COMMON/D3/R1(20,1000),R2(20,1000),R3(20,1000),W(20,1000)
        COMMON/C1/DX,DY,DZ,DT,NODX,NODY,NODZ,TO,TM,QKF,C,RO
        COMMON/C2/V,POWER,RADIUS,AS,QLAM,EPST,EPSS,TIMMAX,OMEGA,WAVEL
        COMMON/C3/ITMAX,RFT,XMIN,XMAX,YMIN,YMAX,ZMIN,ZMAX,DZL
        COMMON/C4/HB1,HT1,HW1,HW2,HW31,HW32,HW33,HW4,HW5,HW61,HW62,HW63
        COMMON/E1/PI,X,Y,Z,I,J,K,KK,HBL,ZNORM,ZNORM2,TIME
        COMMON/E2/SUR,SURMOVE,SURMAX,TEMMAX,BCON1,BCON2,IT
        COMMON/E4/XS,YS,KI
 C
 C
                X = XMIN+DX*(I-1)
                Y = YMIN+DY*(J-1)
                W(J,KI)=-QLAM*TPO(I,J-1,KI)/DZ
 C
 C
                        ZNORM2 = 1. + ((SURI(I,J)-SURI(I-1,J))/DX)**2
     *                                + ((SURI(I,J+1)-SURI(I,J))/DY)**2
        IF(I.EQ.NODX)   ZNORM2 = 1. + ((SURI(I,J+1)-SURI(I,J))/DY)**2
                        ZNORM = SQRT(ZNORM2)
        RETURN
        END
```

```
      SUBROUTINE HMAIN
      COMMON/D1/SURI(20,20),SURO(20,20),SURN(20,20),L(20,20)
      COMMON/D2/TPO(20,20,1000),TPN(20,20,1000)
      COMMON/D3/R1(20,1000),R2(20,1000),R3(20,1000),W(20,1000)
      COMMON/C1/DX,DY,DZ,DT,NODX,NODY,NODZ,TO,TM,QKF,C,RO
      COMMON/C2/V,POWER,RADIUS,AS,QLAM,EPST,EPSS,TIMMAX,OMEGA,WAVEL
      COMMON/C3/ITMAX,RFT,XMIN,XMAX,YMIN,YMAX,ZMIN,ZMAX,DZL
      COMMON/C4/HB1,HT1,HW1,HW2,HW31,HW32,HW33,HW4,HW5,HW61,HW62,HW63
      COMMON/E1/PI,X,Y,Z,I,J,K,KK,HBL,ZNORM,ZNORM2,TIME
      COMMON/E2/SUR,SURMOVE,SURMAX,TEMMAX,BCON1,BCON2,IT
      COMMON/E4/XS,YS,KI
C
C
            Z = ZMIN + (K-1)*DZ
            RADZ2 = (RADIUS**2)*(1.0+(WAVEL*Z/(PI*RADIUS**2))**2)
            SOUR = AS*2.0*POWER/(PI*RADZ2)*
     *             EXP(-((X-XS)**2+(Y-YS)**2)/RADZ2)
C
C
                    W(J,K) = ((1.0-HW1*R1(J,K-1))*W(J,K-1)+
     *       HW2*TPO(I,J,K)+HW31*TPN(I+1,J,K)+ HW4*TPN(I-1,J,K)+
     *       HW5*TPN(I,J+1,K)+HW61*TPN(I,J-1,K))/(1.0 + HW1*R1(J,K))
      IF(I.EQ.NODX)   W(J,K) = ((1.0-HW1*R2(J,K-1))*W(J,K-1)+
     *       HW2*TPO(I,J,K)+HW31*TPN(I+1,J,K)+ HW4*TPN(I-1,J,K)+
     *       HW5*TPN(I,J+1,K)+HW61*TPN(I,J-1,K))/(1.0 + HW1*R2(J,K))
C
C
            HBL = QKF*V/DX*(Z-SURO(I-1,J))
      IF(I.EQ.NODX) HBL = 0.
                    BCON2 = HBL + SOUR - (R1(J,K)*TM+W(J,K))*ZNORM2
      IF(I.EQ.NODX) BCON2 = HBL + SOUR - (R2(J,K)*TM+W(J,K))*ZNORM2
C
C
      RETURN
      END


      SUBROUTINE HNOAB
      COMMON/D1/SURI(20,20),SURO(20,20),SURN(20,20),L(20,20)
      COMMON/D2/TPO(20,20,1000),TPN(20,20,1000)
      COMMON/D3/R1(20,1000),R2(20,1000),R3(20,1000),W(20,1000)
      COMMON/C1/DX,DY,DZ,DT,NODX,NODY,NODZ,TO,TM,QKF,C,RO
      COMMON/C2/V,POWER,RADIUS,AS,QLAM,EPST,EPSS,TIMMAX,OMEGA,WAVEL
      COMMON/C3/ITMAX,RFT,XMIN,XMAX,YMIN,YMAX,ZMIN,ZMAX,DZL
      COMMON/C4/HB1,HT1,HW1,HW2,HW31,HW32,HW33,HW4,HW5,HW61,HW62,HW63
      COMMON/E1/PI,X,Y,Z,I,J,K,KK,HBL,ZNORM,ZNORM2,TIME
      COMMON/E2/SUR,SURMOVE,SURMAX,TEMMAX,BCON1,BCON2,IT
      COMMON/E4/XS,YS,KI
C
C
            K=KK
            SURMOVE = SURO(I,J)
            SURN(I,J) = SURMOVE
            RADZ2 = RADIUS**2*(1.0+(WAVEL*SURMOVE/(PI*RADIUS**2))**2)
            SOUR = AS*2.0*POWER/(PI*RADZ2)*
     *             EXP(-((X-XS)**2+(Y-YS)**2)/RADZ2)
            CCC=(SOUR/ZNORM - W(J,KK)) / R1(J,KK)
            TT = AMIN1(CCC,TM)
            CCC=ABS(TT-TPN(I,J,KK))
```

```
                TEMMAX = AMAX1(CCC,TEMMAX)
                TPN(I,J,KK) = TPN(I,J,KK) + OMEGA*(TT-TPN(I,J,KK))
                IF(KK.LT.NODZ)TPN(I,J,KK)=TM
C
C
                DO 705 KL=KK+1,NODZ
                TPN(I,J,KL) = TPN(I,J,KK)
705             IF(KK.LT.NODZ)TPN(I,J,KL)=TM
C
C
                      KI=1+(J-1)*DY/DZ
                DO 710 K=KK-1,KI,-1
                    TT = ((HT1-R1(J,K))*TT-W(J,K)-W(J,K-1)) / (HT1+R1(J,K-1))
         IF(I.EQ.NODX) TT = ((HT1-R2(J,K))*TT-W(J,K)-W(J,K-1)) / (HT1+R2(J,K-1))
                CCC = ABS(TT-TPN(I,J,K))
                TEMMAX = AMAX1(CCC,TEMMAX)
                TPN(I,J,K) = TPN(I,J,K)+ OMEGA*(TT-TPN(I,J,K))
                TPN(I,J,K) = AMAX1(TPN(I,J,K),TO)
710             CONTINUE
        RETURN
        END


        SUBROUTINE HABLA
        COMMON/D1/SURI(20,20),SURO(20,20),SURN(20,20),L(20,20)
        COMMON/D2/TPO(20,20,1000),TPN(20,20,1000)
        COMMON/D3/R1(20,1000),R2(20,1000),R3(20,1000),W(20,1000)
        COMMON/C1/DX,DY,DZ,DT,NODX,NODY,NODZ,TO,TM,QKF,C,RO
        COMMON/C2/V,POWER,RADIUS,AS,QLAM,EPST,EPSS,TIMMAX,OMEGA,WAVEL
        COMMON/C3/ITMAX,RFT,XMIN,XMAX,YMIN,YMAX,ZMIN,ZMAX,DZL
        COMMON/C4/HB1,HT1,HW1,HW2,HW31,HW32,HW33,HW4,HW5,HW61,HW62,HW63
        COMMON/E1/PI,X,Y,Z,I,J,K,KK,HBL,ZNORM,ZNORM2,TIME
        COMMON/E2/SUR,SURMOVE,SURMAX,TEMMAX,BCON1,BCON2,IT
        COMMON/E4/XS,YS,KI
C
C
               SUR = Z - DZ*(BCON2/(BCON2-BCON1))
               CCC = ABS(SURN(I,J)-SUR)
               SURMAX = AMAX1(SURMAX,CCC)
               SURN(I,J) = SUR
C
C
                K=KK
          RS = R1(J,K) + (R1(J,K-1)-R1(J,K))*(BCON2/(BCON2-BCON1))
        IF(I.EQ.NODX) RS = R2(J,K) + (R2(J,K-1)-R2(J,K))*
     *                          (BCON2/(BCON2-BCON1))
          WS = W(J,K) + (W(J,K-1)-W(J,K))*(BCON2/(BCON2-BCON1))
C
C
                DO 550 KL=KK,NODZ
550             TPN(I,J,KL) = TM
C
C
                  TT = (TM -(RS*TM+WS+W(J,K-1))*BCON1/(HT1*(BCON1-BCON2)))/
     *               (1.0 + R1(J,K-1)*BCON1/(HT1*(BCON1-BCON2)))
        IF(I.EQ.NODX) TT = (TM -(RS*TM+WS+W(J,K-1))*BCON1/(HT1*(BCON1-BCON2)))/
     *               (1.0 + R2(J,K-1)*BCON1/(HT1*(BCON1-BCON2)))
C
C
                     KI=1+(J-1)*DY/DZ
```

```
                DO 560 K = KK-1,KI-1,-1
                 CCC =   ABS(TT-TPN(I,J,K))
                 TEMMAX = AMAX1(CCC,TEMMAX)
                 TPN(I,J,K) = TPN(I,J,K)+OMEGA*(TT-TPN(I,J,K))
                       TT = ((HT1-R1(J,K))*TT-W(J,K)-W(J,K-1))
     *                            /(HT1+R1(J,K-1))
        IF(I.EQ.NODX) TT = ((HT1-R2(J,K))*TT-W(J,K)-W(J,K-1))
     *                            /(HT1+R2(J,K-1))
                        CCC = ABS(TT-TPN(I,J,K))
                        TEMMAX = AMAX1(CCC,TEMMAX)
                        TPN(I,J,K) = TPN(I,J,K)+ OMEGA*(TT-TPN(I,J,K))
                        TPN(I,J,K) = AMAX1(TPN(I,J,K),TO)
560             CONTINUE
                CCC = ABS(TT-TPN(I,J,KI))
                TEMMAX = AMAX1(CCC,TEMMAX)
                TPN(I,J,KI) = TPN(I,J,KI) + OMEGA*(TT-TPN(I,J,KI))
                TPN(I,J,KI) = AMAX1(TPN(I,J,KI),TO)
C
C
        RETURN
        END
```

# Appendix C. Fortran Program for Regression

```
C
C       PROGRAM LINEAR REGRESSION
C
C       VARIABLE DEFINITION
C
C       X:      INDEPENDENT VARIABLES
C       Y:      MEASURED YIELDS
C       C:      COEFFICIENTS IN SIMULTANEOUS ALGEBRAIC EQUATIONS
C       CI:     COEFFICIENTS IN THE INVERSE MATRIX OF C
C       CY:     COEFFICIENTS IN THE RIGHT SIDE OF THE EQUATIONS
C       A:      CONSTANT TERM IN THE REGRESSION EQUATION
C       B:      COEFFICIENTS IN THE REGRESSION EQUATION
C       Q:      AUGMENTED MATRIX COMPOSED OF C, CY, AND UNIT MATRIX
C       NB:     NUMBER OF COEFFICIENTS
C       NY:     NUMBER OF OBSERVATIONS
C       IN:     VALUE FOR DECIDING WHETHER PROCEEDING TO MAXIMUM POINT
C               CALCULATION
C       NROW:   NUMBER OF ROWS OF MATRIX Q
C       NCOL:   NUMBER OF COLUMNS OF MATRIX Q
C
C
      DIMENSION CY(15),C(15,15)
      COMMON/C1/Q(15,30),NROW,NCOL
      COMMON/C2/A,NB,NY,B(15),X(200,20),Y(200),AVERY
      OPEN(UNIT=1,FILE='TEIN.DAT',STATUS='OLD')
      OPEN(UNIT=2,FILE='TEOUT.DAT',STATUS='NEW')
C
C
C             READ INPUT VARIABLES AND YIELDS
C
      READ(1,145)NB,NY,IN
      WRITE(2,146)NB
      DO 100 I=1,NY
      READ(1,153)(X(I,J),J=1,2)
      X(I,1)=X(I,1)/0.65
      X(I,2)=X(I,2)/1.7
100   CONTINUE
C
C
      DO 110 I=1,NY
      READ(1,160)Y(I)
110   CONTINUE
C
C             CALCULATE INDEPENDENT VARIABLES FOR ALL OBSERVATIONS
C
      DO 105 I=1,NY
      X(I,3)=X(I,1)*X(I,1)
      X(I,4)=X(I,2)*X(I,2)
      X(I,5)=X(I,1)*X(I,2)
      X(I,6)=X(I,3)*X(I,1)
      X(I,7)=X(I,4)*X(I,2)
      X(I,8)=X(I,3)*X(I,2)
      X(I,9)=X(I,1)*X(I,4)
105   CONTINUE
C
C
145   FORMAT(/2X,3I5)
146   FORMAT(/2X,' NUMBER OF TERMS CONSIDERED =',I5)
150   FORMAT(2X,8F10.5)
153   FORMAT(2X,2F5.3)
```

```
 155     FORMAT(2X,8F5.2)
 160     FORMAT(2X,F10.5)
 162     FORMAT(2X,I5)
 164     FORMAT(2X,10I5)
C
C               CALCULATE COEFFICIENTS OF MATRIX C
C
        DO 320 J=1,NB
        DO 310 K=1,NB
        SUMU=0.
        SUMV=0.
        SUMW=0.
        DO 300 I=1,NY
        SUMU=SUMU+X(I,J)*X(I,K)
        SUMV=SUMV+X(I,J)
        SUMW=SUMW+X(I,K)
 300    CONTINUE
        C(J,K)=SUMU-SUMV*SUMW/NY
 310    CONTINUE
 320    CONTINUE
C
C               CALCULATE COEFFICIENTS OF MATRIX CY
C
        DO 340 J=1,NB
        SUMXY=0.
        SUMX=0.
        SUMY=0.
        DO 330 I=1,NY
        SUMXY=SUMXY+X(I,J)*Y(I)
        SUMX=SUMX+X(I,J)
        SUMY=SUMY+Y(I)
 330    CONTINUE
        CY(J)=SUMXY-SUMX*SUMY/NY
 340    CONTINUE
C
C
        WRITE(2,1005)
1005    FORMAT(/2X,'  COEFFICIENTS CIJ')
        DO 321 J=1,NB
 321    WRITE(2,150)(C(J,K),K=1,NB)
        WRITE(2,1007)
1007    FORMAT(/2X,'  COEFFICIENTS CY')
        WRITE(2,150)(CY(J),J=1,NB)
C
C               SOLVE THE SIMULTANEOUS EQUATIONS
C
        DO 344 IROW=1,NB
        DO 343 ICOL=1,NB
        Q(IROW,ICOL)=C(IROW,ICOL)
 343    Q(IROW,ICOL+NB+1)=0.
        Q(IROW,NB+1)=CY(IROW)
 344    Q(IROW,IROW+NB+1)=1.
C
C
        NROW=NB
        NCOL=2*NB+1
        CALL FORWARDSOLVE
        CALL BACKSOLVE
C
C               COEFFICIENTS B ARE THE SAME AS ONE COLUMN OF Q
```

```
C
      DO 365 I=1,NB
      B(I)=Q(I,NB+1)
365   CONTINUE
C
C              CALCULATE CONSTANT TERM A
C
      SUMBX=0.
      DO 380 J=1,NB
      SUM=0.
      DO 370 I=1,NY
      SUM=SUM+X(I,J)
370   CONTINUE
      AVERX=SUM/NY
      SUMBX=SUMBX+B(J)*AVERX
380   CONTINUE
      SUMY=0.
      DO 381 I=1,NY
381   SUMY=SUMY+Y(I)
      AVERY=SUMY/NY
      A=AVERY-SUMBX
C
C
      WRITE(2,1008)A
1008  FORMAT(/2X,'  A =',F10.5)
C
C
      WRITE(2,1001)
1001  FORMAT(/2X,' COEFFICIENT B')
      DO 390 I=1,NB
390   WRITE(2,160)B(I)
C
C              DETERMINE THE ACCURACY OF THE REGRESSION EQUATION
C
      CALL RMSQ
      END


      SUBROUTINE FORWARDSOLVE
      COMMON/C1/Q(15,30),NROW,NCOL
C
C
      DO 470 IPIVOT=1,NROW
      CALL ROWPIVOT(IPIVOT)
      FACTOR=Q(IPIVOT,IPIVOT)
      DO 440  ICOL=1,NCOL
440   Q(IPIVOT,ICOL)=Q(IPIVOT,ICOL)/FACTOR
      DO 460 IROW=IPIVOT+1,NROW
      FACTOR=Q(IROW,IPIVOT)
      DO 450 ICOL=IPIVOT,NCOL
450   Q(IROW,ICOL)=Q(IROW,ICOL)-Q(IPIVOT,ICOL)*FACTOR
460   CONTINUE
470   CONTINUE
      RETURN
      END


      SUBROUTINE BACKSOLVE
      COMMON/C1/Q(15,30),NROW,NCOL
C
```

```
C
      DO 500 IPIVOT=NROW,2,-1
      DO 490 IROW=IPIVOT-1,1,-1
      FACTOR=Q(IROW,IPIVOT)
      Q(IROW,IPIVOT)=0.
      DO 480 ICOL=IPIVOT+1,NCOL
480   Q(IROW,ICOL)=Q(IROW,ICOL)-Q(IPIVOT,ICOL)*FACTOR
490   CONTINUE
500   CONTINUE
      RETURN
      END


      SUBROUTINE ROWPIVOT(IPIVOT)
      COMMON/C1/Q(15,30),NROW,NCOL
C
C
      ISMALL=IPIVOT
      DO 510 IROW=IPIVOT+1,NROW
      IF(ABS(Q(IROW,IPIVOT)).GT.ABS(Q(ISMALL,IPIVOT))) ISMALL=IROW
510   CONTINUE
      IF(ISMALL.NE.IPIVOT) THEN
      DO 520 ICOL=1,NCOL
      TEMP=Q(IPIVOT,ICOL)
      Q(IPIVOT,ICOL)=Q(ISMALL,ICOL)
520   Q(ISMALL,ICOL)=TEMP
      ENDIF
      RETURN
      END


      SUBROUTINE RMSQ
      COMMON/C2/A,NB,NY,B(15),X(200,20),Y(200),AVERY
C
C
      RMS=0.
      WRITE(2,150)
      DO 100 I=1,NY
      D=A
      DO 101 J=1,NB
      D=D+B(J)*X(I,J)
101   CONTINUE
      WRITE(2,160)I,D,Y(I)
      RMS=RMS+(D-Y(I))**2
100   CONTINUE
      RMS=SQRT(RMS)/NY/AVERY
      WRITE(2,200)RMS
150   FORMAT(/2X,'            NUMBER   CALCULATED   MEASURED'/)
160   FORMAT(2X,I15,2F15.7)
200   FORMAT(//2X,'  ROOT MEAN SQUARE OF THE REGRESSION EQ. =',F15.10)
      RETURN
      END
```

## Appendix D: Optimization of Three-Dimensional Laser Machining

The task is to remove a given amount of material at a minimum time, as shown in Fig. 1. It is assumed that groove depth is constant for a fixed process condition. This assumption ignores technical difficulties associated with focusing beams on workpiece surfaces.

For single pass machining, the machining time is the number of sections times the time to machine each section (Fig. 1).

$$t = \frac{a^2}{D^2}\frac{b}{v} \tag{1}$$

where D is the depth of cut and v is the scanning velocity.

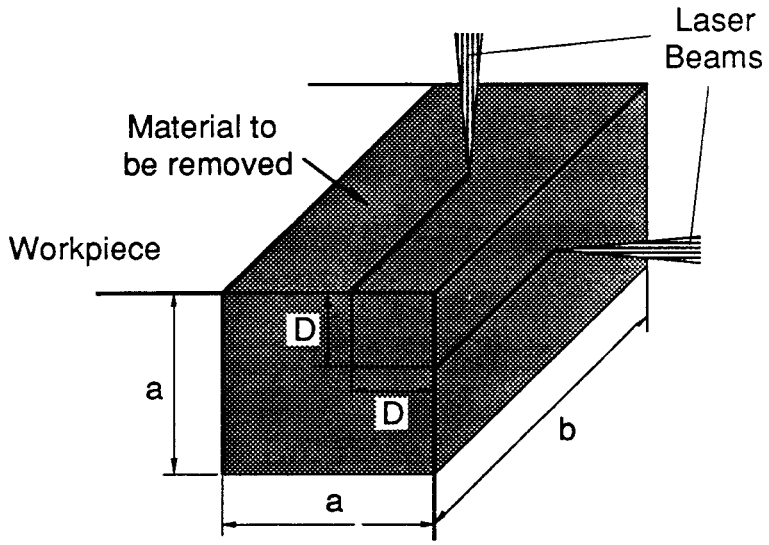



Fig. 1: Three-dimensional laser machining.

An inverse velocity is defined as w = 1/v. Groove depth is a function of w.

$$D = f(1/v) = f(w) \tag{2}$$

The machining time is expressed as

$$t = \frac{a^2}{\left(f(w)\right)^2} bw = \frac{V w}{\left(f(w)\right)^2} \tag{3}$$

where V is the amount of material to be removed. The optimal inverse velocity to minimize the machining time can be determined from $\partial t/\partial w = 0$.

$$\frac{\partial t}{\partial w} = -\frac{2Vwf'}{f^3} + \frac{V}{f^2} \tag{4}$$

$\partial t/\partial w = 0$ yields the following relation

$$2f'w = f \tag{5}$$

The value of w satisfying Eq. (5) is the optimal inverse velocity for single pass machining, which maximizes the material removal rate. Graphically, the optimal value of w can be determined as shown in Fig. 2. If w is less than the optimal value, the amount of material removed is small and the machining time becomes large. If w is larger than the value, the velocity is slow and the machining time becomes large.

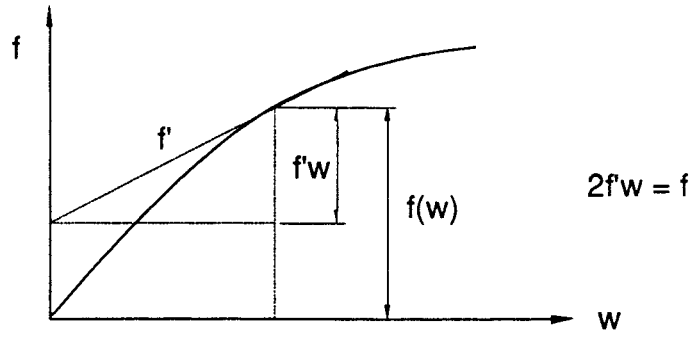



Fig. 2: Optimal inverse velocity for a single pass machining.

For two pass machining, the depth of cut is the sum of depths cut by two passes.

$$D = f_1(w_1) + f_2(w_2) \tag{7}$$

where $f_1(w_1)$ and $f_2(w_2)$ are the depths of cut by first and second pass, respectively (Fig. 3). The machining time is

$$t = \frac{a^2}{\left(f_1(w_1) + f_2(w_2)\right)^2}(bw_1 + bw_2) = \frac{V\,(w_1 + w_2)}{\left(f_1(w_1) + f_2(w_2)\right)^2} \tag{8}$$

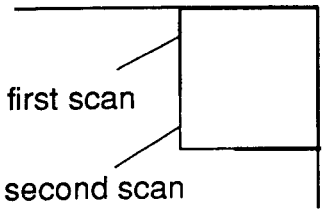



Fig. 3: Depths of cut for two pass machining.

Differentiations of the machining time with respect to $w_1$ and $w_2$ yield

$$\frac{\partial t}{\partial w_1} = -\frac{2V(w_1 + w_2)\,f_1'}{(f_1 + f_2)^3} + \frac{V}{(f_1 + f_2)^2} \tag{9}$$

$$\frac{\partial t}{\partial w_2} = -\frac{2V(w_1 + w_2)\,f_2'}{(f_1 + f_2)^3} + \frac{V}{(f_1 + f_2)^2} \tag{10}$$

$\partial t/\partial w_1 = 0$ and $\partial t/\partial w_2 = 0$ give

$$2f_1'\,(w_1 + w_2) = f_1 + f_2 \tag{11}$$

$$2f_2'\,(w_1 + w_2) = f_1 + f_2 \tag{12}$$

From Eqs. (11) and (12), the following relation is obtained.

$$f_1' = f_2' \tag{13}$$

The above realtion implies that the slope in the relation of depth and inverse velocity should be kept constant to minimize the machining time. If $w_1$ is selected, then $w_2$ is determined according to Eq. (13). The inverse velocities can be chosen to make the sum of depths of cut the same as the section length.

For n-pass machining, a similar calculation can be performed. The machining time is

$$t = \frac{V\,(w_1 + w_2 + \ldots + w_n)}{\left(f_1(w_1) + f_2(w_2) + \ldots + f_n(w_n)\right)^2} \tag{14}$$

$$\frac{\partial t}{\partial w_i} = -\frac{V\,(w_1 + w_2 + \ldots + w_n)\,f_i'}{(f_1 + f_2 + \ldots + f_n)^3} + \frac{V}{(f_1 + f_2 + \ldots + f_n)^2} \tag{15}$$

for $i = 1,\ldots,n$

$\partial t/\partial w_i = 0$ for $i = 1,\ldots,n$

$$2f_i'\,(w_1 + w_2 + \ldots + w_n) = (f_1 + f_2 + \ldots + f_n) \tag{16}$$

In order to minimize the machining time, the slopes throughout any passes should be the same.

$$f_i' = f_j' \qquad\qquad i = 1,\ldots,n \text{ and } j = 1,\ldots,n \tag{17}$$

Since the groove depth decreases monotonically for a higher pass due to beam defocussing and increment in conduction area, the inverse velocity should be smaller to keep the slope constant. Thus, the scanning velocity should be increased for higher number of passes.

The given task can be achieved by any number of passes. Now, the optimal number of passes has to be determined. For n-1 and n pass machinings, the machining times for a fixed depth of cut are respectively

$$t_{n-1} = \frac{V}{D^2}(w_1 + w_2 + \ldots + w_{n-1}) \tag{18}$$

$$t_n = \frac{V}{D^2}(w_1 + w_2 + \ldots + w_n) \tag{19}$$

Since the machining times are proportional to the sum of inverse velocities, the optimal number of passes should correspond to a minimum sum of inverse velocities. For the two cases, the fixed depth of cut implies

$$f_{n-1}'\,(w_1 + \ldots + w_{n-1})_{n-1} = f_n'\,(w_1 + \ldots + w_n)_n \tag{20}$$

The depth cut by the first pass is smaller for n number of passes than n-1 number of passes. Thus, the slope $f_n'$ should be larger than $f_{n-1}'$. In order to satisfy Eq. (20), the sum of inverse velocities for n passes should be smaller than those for n-1 passes. Since there is no restriction on n, the largest possible number of passes is optimal, as long as the slope can be kept constant.

Now the number of sections or the length of each side of a section should be determined. It was found that an optimal number of passes should be as large as possible and the machining time is proportional to the sum of inverse velocities. Fig. 4 shows the relation between section length and sum of inverse velocities for the maximum possible number of passes. When a section length is given, Fig. 4 gives the optimal sum of inverse velocities. In order to be able to plot the figure, all the functional relations between groove depth and inverse velocity for all the number of passes are needed. The machining time to remove a volume V is expressed as

$$t = \frac{V}{D_t^2} w_t = \frac{V}{g(w_t)} w_t \tag{21}$$

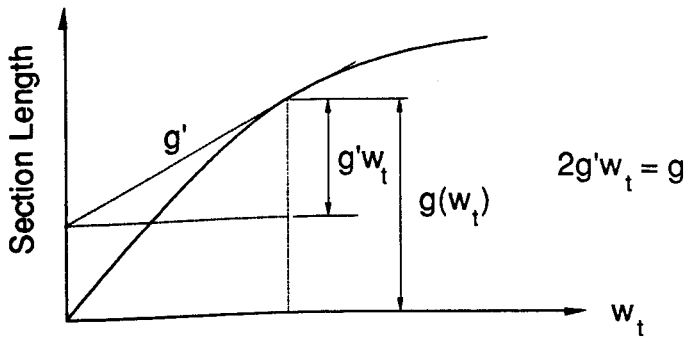



Fig. 4: Section length vs. optimal sum of inverse velocities.

Differentiation of the machining time with respect to $w_t$ yields

$$\frac{\partial t}{\partial w_t} = - \frac{V w_t g'}{g^3} + \frac{V}{g^2} \tag{22}$$

$\partial t/\partial w_t = 0$ gives the following relation

$$2g'w_t = g \tag{23}$$

The sum of inverse velocities and section length which satisfy Eq. (23) are optimal. However, the optimal sum of inverse velocities should be chosen so that the section length is close to the optimal section length, since the total length to cut should be a multiple of the section length.